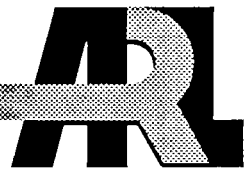


ARMY RESEARCH LABORATORY



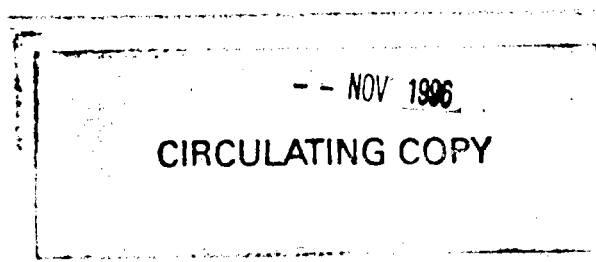
# Normal Depth of Penetration Experiments in Ceramic/Metal Targets Simulated by Computer

James Dehn

ARL-TR-487

July 1994

ARL TECHNICAL LIBRARY  
APG, MD. 21005-5066



APPROVED FOR PUBLIC RELEASE; DISTRIBUTION IS UNLIMITED.

## NOTICES

Destroy this report when it is no longer needed. DO NOT return it to the originator.

Additional copies of this report may be obtained from the National Technical Information Service, U.S. Department of Commerce, 5285 Port Royal Road, Springfield, VA 22161.

The findings of this report are not to be construed as an official Department of the Army position, unless so designated by other authorized documents.

The use of trade names or manufacturers' names in this report does not constitute indorsement of any commercial product.

**INTENTIONALLY LEFT BLANK.**

## LIST OF TABLES

<u>Table</u>		<u>Page</u>
1.	Key Material Properties Used in the Computer Simulations . . . . .	2
2.	L/D=10 WA Rods Striking at 1,500 m/s . . . . .	5
3.	L/D=10 WA Rods Striking at 1,000 m/s . . . . .	8
4.	L/D=3.2 WA Rods Striking at 1,500 m/s . . . . .	9
5.	L/D=3.2 WA Rods Striking at 1,000 m/s . . . . .	9
6.	L/D=20 WA Rods Striking at 1,500 m/s . . . . .	10
7.	L/D=20 WA Rods Striking at 1,000 m/s . . . . .	10

INTENTIONALLY LEFT BLANK.

<u>Figure</u>	<u>Page</u>
39. L/D=20 WA rod at 1,500 m/s against 2.54-cm SiC in Ti covered by 1-cm Ti at 200 $\mu$ s .....	52
40. L/D=20 WA rod at 1,500 m/s against 2.54 cm-SiC in $\infty$ Ti covered by 1-cm Ti: speed and position of rod nose and tail and tile back vs. time .....	53
41. L/D=20 WA rod at 1,000 m/s against 2.54-cm SiC in $\infty$ Ti at 150 $\mu$ s .....	54
42. L/D=20 WA rod at 1,000 m/s against 2.54-cm SiC in $\infty$ Ti covered by 1-cm Ti at 150 $\mu$ s .....	55
43. L/D=10 WA rod at 1,500 m/s against $\infty$ RHA at 10 $\mu$ s: $10^8$ -dynes/cm <sup>2</sup> pressure contours .....	56
44. L/D=10 WA rod at 1,500 m/s against $\infty$ Ti at 10 $\mu$ s: $10^8$ -dynes/cm <sup>2</sup> pressure contours .....	57
45. L/D=10 WA rod at 1,500 m/s against $\infty$ SiC at 10 $\mu$ s: $10^8$ -dynes/cm <sup>2</sup> pressure contours .....	58
46. L/D=10 WA rod at 1,500 m/s against $\infty$ Ti at 6 $\mu$ s: pressure vertical histogram on the shotline .....	59
47. L/D=10 WA rod at 1,500 m/s against $\infty$ Ti at 10 $\mu$ s: pressure vertical histogram on the shotline .....	60
48. L/D=10 WA rod at 1,500 m/s against $\infty$ Ti at 20 $\mu$ s: pressure vertical histogram on the shotline .....	61
49. L/D=10 WA rod at 1,500 m/s against $\infty$ Ti at 50 $\mu$ s: pressure vertical histogram on the shotline .....	62
50. L/D=10 WA rod at 1,500 m/s against 2.54-cm SiC in $\infty$ Ti at 10 $\mu$ s: $10^8$ -dynes/cm <sup>2</sup> pressure contours .....	63
51. L/D=10 WA rod at 1,500 m/s against 2.54-cm SiC in $\infty$ Ti at 10 $\mu$ s: pressure vertical histogram on the shotline .....	64
52. L/D=10 WA rod at 1,500 m/s against 2.54-cm SiC in $\infty$ Ti at 10 $\mu$ s: pressure vertical histogram 3 cm from the shotline .....	65
53. L/D=10 WA rod at 1,500 m/s against 2.54-cm SiC in $\infty$ Ti at 10 $\mu$ s: pressure horizontal histograms at y=2.45 cm and y=2.65 cm just below and above the tile back .....	66
54. L/D=10 WA rod at 1,500 m/s against 2.54-cm SiC in $\infty$ Ti at 20 $\mu$ s: pressure horizontal histograms at y=2.45 cm and y=2.65 cm just below and above the tile back .....	67

<u>Figure</u>		<u>Page</u>
21.	L/D=10 WA rod at 1,000 m/s against 2.54-cm AD99.5 in $\infty$ RHA: speed and position of rod nose and tail and tile back vs. time .....	34
22.	L/D=10 WA rod at 1,000 m/s against 2.54-cm SiC in $\infty$ Ti covered by 1-cm Ti at 200 $\mu$ s .....	35
23.	L/D=10 WA rod at 1,000 m/s against 2.54-cm SiC in $\infty$ Ti at 200 $\mu$ s .....	36
24.	L/D=3.2 WA rod at 1,500 m/s against 2.54-cm SiC in $\infty$ Ti at 0 $\mu$ s .....	37
25.	L/D=3.2 WA rod at 1,500 m/s against 2.54-cm SiC in $\infty$ Ti at 200 s .....	38
26.	L/D=3.2 WA rod at 1,500 m/s against 2.54-cm SiC in $\infty$ Ti: speed and position of rod nose and tail and tile back vs. time .....	39
27.	L/D=3.2 WA rod at 1,500 m/s against 2.54-cm SiC in $\infty$ Ti covered by 1-cm Ti at 0 $\mu$ s .....	40
28.	L/D=3.2 WA rod at 1,500 m/s against 2.54-cm SiC in $\infty$ Ti covered by 1-cm Ti at 200 $\mu$ s .....	41
29.	L/D=3.2 WA rod at 1,500 m/s against 2.54-cm SiC in $\infty$ Ti covered by 1-cm Ti: speed and position of rod nose and tail and tile back vs. time .....	42
30.	L/D=20 WA rod at 1,612 m/s against 4.00-cm AD99.5 in $\infty$ RHA covered by 1.27-cm RHA at 0 $\mu$ s .....	43
31.	L/D=20 WA rod at 1,612 m/s against 4.00-cm AD99.5 in $\infty$ RHA covered by 1.27-cm RHA at 200 $\mu$ s .....	44
32.	L/D=20 WA at 1,612 m/s against 4.00-cm AD99.5 in $\infty$ RHA covered by 1.27-cm RHA: speed and position of rod nose and tail and tile back vs. time .....	45
33.	L/D=20 WA at 1,500 m/s against $\infty$ RHA at 0 $\mu$ s .....	46
34.	L/D=20 WA rod at 1,500 m/s against $\infty$ RHA at 200 $\mu$ s .....	47
35.	L/D=20 WA rod at 1,500 m/s against 2.54-cm SiC in $\infty$ Ti at 0 $\mu$ s .....	48
36.	L/D=20 WA rod at 1,500 m/s against 2.54-cm SiC in $\infty$ Ti at 200 $\mu$ s .....	49
37.	L/D=20 WA rod at 1,500 m/s against 2.54-cm SiC in $\infty$ Ti: speed and position of rod nose and tail and tile back vs. time .....	50
38.	L/D=20 WA rod at 1,500 m/s against 2.54-cm SiC in $\infty$ Ti covered by 1-cm Ti at 0 $\mu$ s .....	51

## LIST OF FIGURES

<u>Figure</u>	<u>Page</u>
1. L/D=10 WA rod at 1,500 m/s against $\infty$ RHA at 0 time .....	14
2. L/D=10 WA rod at 1,500 m/s against $\infty$ RHA at 200 $\mu$ s .....	15
3. L/D=10 WA rod at 1,500 m/s against 10-cm RHA at 200 $\mu$ s .....	16
4. L/D=10 WA rod at 1,500 m/s against RHA: speed and position of rod nose and tail as a function of time .....	17
5. L/D=10 WA rod at 1,500 m/s against 2.54-cm AD99.5 in $\infty$ RHA at 0 time .....	18
6. L/D=10 WA rod at 1,500 m/s against 2.54-cm AD99.5 in $\infty$ RHA at 50 $\mu$ s .....	19
7. L/D=10 WA rod at 1,500 m/s against 2.54-cm AD99.5 in $\infty$ RHA at 200 $\mu$ s .....	20
8. L/D=10 WA rod at 1,500 m/s against 2.54-cm AD99.5 in $\infty$ RHA: speed and position of rod nose and tail and tile back vs. time .....	21
9. L/D=10 WA rod at 1,500 m/s against 2.54-cm SiC in $\infty$ RHA at 50 $\mu$ s .....	22
10. L/D=10 WA rod at 1,500 m/s against 2.54-cm SiC in $\infty$ Ti at 50 $\mu$ s .....	23
11. L/D=10 WA rod at 1,500 m/s against 2.54-cm AD99.5 in $\infty$ Ti: speed and position of rod nose and tail and tile back vs. time .....	24
12. L/D=10 WA rod at 1,500 m/s against 2.54-cm SiC in $\infty$ RHA at 650 $\mu$ s .....	25
13. L/D=10 WA rod at 1,500 m/s against 2.54-cm SiC at 200 $\mu$ s .....	26
14. L/D=10 WA rod at 1,500 m/s against 2.54-cm SiC at 650 $\mu$ s .....	27
15. L/D=10 WA rod at 1,500 m/s against 2.54-cm RHA at 0 $\mu$ s .....	28
16. L/D=10 WA rod at 1,500 m/s against 2.54-cm RHA at 200 $\mu$ s .....	29
17. L/D=10 WA rod at 1,500 m/s against 2.54-cm RHA at 650 $\mu$ s .....	30
18. L/D=10 WA rod at 1,500 m/s against 2.54-cm SiC in $\infty$ Ti covered by 1-cm Ti at 0 time .....	31
19. L/D=10 WA rod at 1,500 m/s against 2.54-cm SiC in $\infty$ Ti covered by 1-cm Ti at 50 $\mu$ s .....	32
20. L/D=10 WA rod at 1,000 m/s against 2.54-cm AD99.5 in $\infty$ RHA at 200 $\mu$ s .....	33

INTENTIONALLY LEFT BLANK.

## TABLE OF CONTENTS

	<u>Page</u>
ACKNOWLEDGMENTS .....	iii
LIST OF FIGURES .....	vii
LIST OF TABLES .....	xi
1. INTRODUCTION .....	1
2. OVERVIEW OF COMPUTER SIMULATIONS .....	1
3. NUMERICAL SIMULATIONS OF L/D=10 WA RODS IMPACTING TARGETS AT 1,500 m/s .....	4
4. SIMULATIONS INVOLVING RODS OF VARIOUS L/D RATIOS AND STRIKING SPEEDS .....	8
5. SIMULATIONS OF WAVE MOTION IN IMPACT PROBLEMS .....	11
6. SUMMARY .....	12
7. RECOMMENDATIONS .....	13
8. REFERENCES .....	69
DISTRIBUTION LIST .....	71

**INTENTIONALLY LEFT BLANK.**

#### ACKNOWLEDGMENTS

The author wishes to thank some of the Army Research Laboratory (ARL) people who have helped him in this work. In particular, he thanks Bill Gooch and his team, especially Matt Burkins for the L/D=10 data and the L/D=3.2 data. In addition, he thanks George Hauver and his team for the L/D=20 data. Also, he wants to thank Skip Filbey and his team, especially Bert Meyer, for all of their support and many helpful discussions. Finally, Kent Kimsey deserves a special acknowledgment for frequently sharing his time and expertise with the author.

INTENTIONALLY LEFT BLANK.

# REPORT DOCUMENTATION PAGE

Form Approved  
OMB No. 0704-0188

Public reporting burden for this collection of information is estimated to average 1 hour per response, including the time for reviewing instructions, searching existing data sources, gathering and maintaining the data needed, and completing and reviewing the collection of information. Send comments regarding this burden estimate or any other aspect of this collection of information, including suggestions for reducing this burden, to Washington Headquarters Services, Directorate for Information Operations and Reports, 1215 Jefferson Davis Highway, Suite 1204, Arlington, VA 22202-4302, and to the Office of Management and Budget, Paperwork Reduction Project (0704-0188), Washington, DC 20503.

1. AGENCY USE ONLY (Leave blank)	2. REPORT DATE	3. REPORT TYPE AND DATES COVERED	
	July 1994	Final, 1 Jul 91-1 Jul 93	
4. TITLE AND SUBTITLE  Normal Depth of Penetration Experiments in Ceramic/Metal Targets Simulated by Computer			5. FUNDING NUMBERS  WO: 4G020-301-T2
6. AUTHOR(S)  James Dehn			
7. PERFORMING ORGANIZATION NAME(S) AND ADDRESS(ES)  U.S. Army Research Laboratory ATTN: AMSRL-WT-TA Aberdeen Proving Ground, MD 21005-5066			8. PERFORMING ORGANIZATION REPORT NUMBER
9. SPONSORING / MONITORING AGENCY NAME(S) AND ADDRESS(ES)  U.S. Army Research Laboratory ATTN: AMSRL-OP-AP-L Aberdeen Proving Ground, MD 21005-5066			10. SPONSORING / MONITORING AGENCY REPORT NUMBER  ARL-TR-487
11. SUPPLEMENTARY NOTES			
12a. DISTRIBUTION / AVAILABILITY STATEMENT  Approved for public release; distribution is unlimited.		12b. DISTRIBUTION CODE	
13. ABSTRACT (Maximum 200 words)  Since ceramics are quite brittle they cannot be used alone as passive elements in vehicle armors because of multi-hit requirements. Consequently, layers of ceramic tiles embedded in more ductile metals are usually employed for this purpose. The performance of such arrays depends heavily on the geometry and materials used. To shorten the search for suitable arrangements, computer simulations can be alternated with experiments. Here we will discuss some current efforts to simulate the ballistic performance of ceramics against kinetic energy threats.			
14. SUBJECT TERMS  kinetic energy projectiles, armored vehicles, mathematical model			15. NUMBER OF PAGES  79
			16. PRICE CODE
17. SECURITY CLASSIFICATION OF REPORT  UNCLASSIFIED	18. SECURITY CLASSIFICATION OF THIS PAGE  UNCLASSIFIED	19. SECURITY CLASSIFICATION OF ABSTRACT  UNCLASSIFIED	20. LIMITATION OF ABSTRACT  UL

## 1. INTRODUCTION

Early experiments using ceramics confined by metals as armor candidates to protect against kinetic energy projectiles determined the ballistic limit velocity for thin ceramic tiles backed by thin aluminum plates (Wilkens, Kline, and Honodel 1969, 1971; Wilkens 1978). Subsequent experience with this technique found that it was not suitable as a method for ranking the performance of different ceramics. Like any ballistic limit test, it is specific to the conditions used and unsuitable for drawing more general conclusions. More recent work (Bless, Rosenberg, and Yoon 1987; Rosenberg and Yeshurun 1988; Woolsey, Mariano, and Kokidko 1989; Woolsey, Kokidko, and Mariano 1990; Woolsey 1992;\* Rosenberg and Tsaliah 1990; and Morris and Anderson 1991) has concentrated on the use of thick ceramic tiles with effectively semi-infinite lateral and rear metal confinement. By comparing depth of (residual) penetration into the metal backing with penetration into the metal alone, it is possible to rank the performance of different ceramics and make more general conclusions, provided we avoid tile overmatch and rod overmatch extremes (Woolsey, Kokidko, and Mariano 1990; Woolsey 1990). However, there is still a considerable dependence on the response of the whole system as pointed out by Hauver et al. (1992), who emphasize the importance of acoustic impedance throughout a target system in suppressing or enhancing target damage. In practical applications, a metal cover plate and some sort of binder between ceramic and metal are always included, which makes the total system response even more complicated. In addition, impacts at 0° obliquity are unlikely, and a variety of threats is likely in practice. This makes an interplay between computer simulations and experiments desirable as a means to hasten the optimization of an armor system. This report is a small step in that direction.

## 2. OVERVIEW OF COMPUTER SIMULATIONS

The examples given in this report were generated using the Cray 2 computer located at the U.S. Army Research Laboratory, Aberdeen Proving Ground, MD. An Eulerian code, HULL, public domain version 122, was employed (Matuska et al. 1978; Matuska and Durret 1978).\*\* In all cases, a two-dimensional rotationally symmetric coordinate system was used with a uniform grid and 1-mm cell size. Although the code has provisions for including work hardening in its yielding criteria, a perfectly

---

\* This is more widely available than Woolsey, Kokidko, and Mariano (1990), discussing methodology and examples using aluminum oxide.

\*\* This code is widely available in many versions. The most recent public domain version is available from Orlando Technology Incorporated (OTI) and other resources.

plastic model was used since insufficient experimental data was available to justify a more elaborate model. The code also permits a variety of failure models to be used. Here a simple tensile failure stress ( $T_f$ ) - failure strain ( $\epsilon_f$ ) model was used. These two parameters are shown in the last two rows of Table 1 for the six materials used in this study. For lack of better information, the  $\epsilon_f$  values for the four metals were all set to 0.5, while the  $\epsilon_f$  values for the two ceramics were both set to 0.05. More information was available for the yield stress (Y) of metals, so the second row in Table 1 gives values which are typical for a 93% tungsten Wa (4Ni-3Fe) alloy, rolled homogeneous armor (RHA), an aluminum (Al) alloy, and a 90% titanium (Ti) alloy. The Ti (Ti-6Al-4V) alloy has a yield strength near 1 GPa (Donachie 1988). Here we wish to compare RHA and Ti as candidates for the role of metal confinement of ceramics. Since their strengths are not very different, it was decided to use the same yield and failure criteria for both metals in order to emphasize the effects of density in our computer simulations. A weaker, less dense Al is also compared in the same role. The  $T_f$  values for the metals were taken to be about three times their yield values. Both the  $T_f$  and  $\epsilon_f$  values are higher than those obtained from quasi-static tensile tests and reflect an effort to simulate the effects of high strain rates and pressures.

Table 1. Key Material Properties Used in the Computer Simulation

	WA	RHA	Ti	Al	SiC	$\text{Al}_2\text{O}_3$
Density $\rho$ (g/cm <sup>3</sup> )	17.65	7.86	4.51	2.71	3.18	3.90
Compressive Yield stress Y, (dyne/cm <sup>2</sup> $\times 10^{-9}$ )	11.0	7.50	7.50	3.00	150.0	40.0
Tensile failure stress $T_f$ (dyne/cm <sup>2</sup> $\times 10^{-9}$ )	33.0	25.0	25.0	9.00	20.0	10.0
Failure strain $\epsilon_f$	0.5	0.5	0.5	0.5	0.05	0.05

The yield and failure criteria for the two ceramics are the most uncertain values in Table 1, especially in the case of silicon carbide (SiC). The compressive strength of 99.5% pure alumina ( $\text{Al}_2\text{O}_3$ ) is 2,618 MPa ( $26 \times 10^9$  dyne/cm<sup>2</sup>), while its tensile strength is one-tenth of this value, according to ASM International's Engineered Materials Handbook (1991). For SiC, only the compressive strength, 4,600 MPa, is known (AMS International 1991), since SiC is not yet as well established an engineered material as alumina. These values follow the trend of the hardness numbers reported for these materials as well (McColm 1990). We expect compressive strengths of ceramics to increase with pressure. For

silicon carbide, Anderson et al. (1992) report an increase of almost 50% for the compressive strength of SiC as the confining pressure is increased from atmospheric to 200 MPa, using a Split-Hopkinson Pressure Bar (SHPB) technique. Ballistic experiments on confined ceramics should also show a change in ceramic strength but in a time- and space-dependent manner. Here we can only use an average value. Our choices of  $40 \times 10^9$  dyne/cm<sup>2</sup> for the compressive yield strength of alumina and  $150 \times 10^9$  dyne/cm<sup>2</sup> for silicon carbide are higher than the handbook compressive strengths and were ultimately guided by a desire to make the simulation agree with the small amount of experimental ballistic data which is currently available. Our choices for the ceramic failure criteria were made in the same spirit. We have chosen  $T_f$  for alumina to be about 25% of the compressive yield strength,  $Y$ , in spite of the fact that the handbook tensile strength is only 10% of the compressive strength. For SiC, we have chosen  $T_f$  to be closer to 10% of the corresponding  $Y$ . The failure strains,  $\epsilon_f$ , were both chosen to be one-tenth the values chosen for the metals. To simulate failure, the code inserts air into cells where the  $T_f$  and  $\epsilon_f$  values have been exceeded. With our current choices, weak but ductile metals like Al will not fail under the same impact conditions which crack stronger but more brittle ceramics, namely, for compressions up to 10 GPa and tensions up to 2 GPa. For all of the materials considered, a Mie-Grüneisen equation of state was used.

Finally, there is the question of artificial viscosity (Zukas et al. 1982). Since shock widths are often smaller than the grid being used, artificial "ringing" will arise from numerical instability. Neumann and Richtmeyer added a term proportional to the derivative of the velocity to the pressure to smooth this ringing. For shock waves in air this damping artifice is required, since real viscosity is usually omitted in code simulations of wave structure. For solids under the conditions we are considering, artificial viscosity it is considerably less important than for gases like air. However, experience with the code shows that it has an effect not only on the clarity of wave simulations but also (to a lesser extent) on the final depth of penetration (DOP). Here we have chosen 0.15 for the linear coefficient of artificial viscosity and 0 for the quadratic coefficient. Not using any artificial viscosity leads to unphysical target distortions at late times. Using higher values like 0.5 tends to obscure the wave structure which controls important damage phenomena in ceramic metal targets. Anderson et al. (1992), have reported a similar need to include linear artificial viscosity in their HEMP code simulations.

Many of these choices of material properties and code parameters may seem to be rather arbitrary. Indeed, there is much room for improvement in all aspects of code calculations. Here we are attempting to simulate a variety of experimental penetration phenomena using the simplest models possible. Reasonable agreement with available experimental data might then encourage us to simulate experiments

not yet done. We will also use some of the time-resolved information which is generated by code simulations to conjecture about possible explanations of some of the phenomena. Unfortunately, this information cannot be compared to experiment at the moment, since the amount of time-resolved experimental information which is currently available is quite limited.

### 3. NUMERICAL SIMULATIONS OF L/D=10 WA RODS IMPACTING TARGETS AT 1,500 m/s

Since cylindrical coordinates were used, there was no need for a plane strain approximation. The 93% WA rod (Teledyne X21) had a hemispherical nose and length to diameter (L/D) ratio  $L/D=7.77 \text{ cm}/.777 \text{ cm}=10$ . The semi- $\infty$  targets were all 20 cm in diameter and 20 cm thick. Ceramic tile inserts were all 15 cm in diameter and 2.54 cm thick. When cover plates were used, they were 15 cm in diameter and 1.0 cm thick. All impacts were at  $0^\circ$  obliquity at the center of the target face. Simulations were also carried out for 10-cm-thick targets, which is closer to the value used in the experiments. In most cases, there were only minor differences in the DOP. In a few cases, there were qualitative differences in the appearance of the simulated residual rod, and these will be noted. Since the penetration depth was greater than 10 cm in some of the simulations, especially those involving Al or L/D=20 rods, it was decided to adopt 20 cm as a standard semi-infinite target thickness to avoid rear face bulges or perforations and to facilitate comparisons between simulations.

Figure 1 shows the rod about to impact a semi- $\infty$  RHA target at 1,500 m/s, while Figure 2 shows the resultant penetration at 200  $\mu\text{s}$  when the rod has ceased to move. Figure 3 shows the resultant penetration for a target 10 cm thick. The final DOP is indistinguishable from that in Figure 2, while the qualitative appearances of targets and rods are quite similar. Figure 4 (target 20 cm thick) shows the positions and speeds of the rod nose and tail as a function of time. The velocity of the rod nose drops to one-third of its striking value in the first few microseconds and then declines more gradually without showing anything which could reasonably be called a steady state. The final length of the rod is 1.5 cm, compared to its original length of 7.77 cm, and the total DOP is 7.2 cm, compared to an experimental value of 7.3 cm. An identical impact on a semi- $\infty$  Ti target gave a calculated residual rod length of 1.8 cm and a final DOP of 7.9 cm, compared to an experimental value of 8.0 cm (see Table 2).

Figure 5 shows the same rod about to impact an AD99.5 alumina tile in a semi- $\infty$  metal surround (in this case, RHA) at 1,500 m/s. Figure 6 gives the result 50  $\mu\text{s}$  after impact, showing a conical piece of broken ceramic being ejected from the impacted face. Figure 7 shows conditions 200  $\mu\text{s}$  after impact

Table 2. L/D=10 WA Rods Striking at 1,500 m/s

Target	Exper. <i>P</i> (cm)	<i>P</i> (cm)	<i>l</i> (cm)	<i>e<sub>m</sub></i>	<i>e<sub>s</sub></i>	<i>q</i> <sup>2</sup>
Semi-infinite Targets						
RHA $\infty$	7.3	7.2	1.5	1.0	1.0	1.0
Ti $\infty$	8.0	7.9	1.8	1.6	0.9	1.4
Al $\infty$	—	15.2	2.3	1.4	0.5	0.7
Ceramic Inserts						
2.54-cm Al <sub>2</sub> O <sub>3</sub> in RHA $\infty$	6.4	6.2	1.4	1.4	1.1	1.5
2.54-cm Al <sub>2</sub> O <sub>3</sub> in Ti $\infty$	—	6.9	1.7	1.9	1.0	1.9
2.54-cm Al <sub>2</sub> O <sub>3</sub> in Al $\infty$	—	12.0	2.3	1.6	0.6	1.0
2.54-cm SiC in RHA $\infty$	5.6	5.6	1.5	1.8	1.3	2.3
2.54-cm SiC in Ti $\infty$	—	5.8	1.6	2.5	1.2	3.0
Covered Inserts						
2.54-cm SiC in Al $\infty$	—	9.0	1.8	2.2	0.8	1.8
1-cm RHA on 2.54-cm Al <sub>2</sub> O <sub>3</sub> in RHA $\infty$	—	6.4	1.5	1.4	1.1	1.5
1-cm Ti on 2.54-cm Al <sub>2</sub> O <sub>3</sub> in Ti $\infty$	—	7.0	1.7	1.9	1.0	1.9
1-cm Al on 2.54-cm Al <sub>2</sub> O <sub>3</sub> in Al $\infty$	—	12.3	2.1	1.6	0.6	1.0
1-cm RHA on 2.54-cm SiC in RHA $\infty$	—	5.3	1.7	1.9	1.3	2.5
1-cm Al on 2.54-cm SiC in Al $\infty$	—	7.7	1.3	2.7	0.9	2.4
1-cm Al on 2.54-cm SiC in RHA $\infty$	—	5.9	1.5	1.9	1.2	2.3

Note: Penetration depths *P*, residual rod lengths *l*, and ballistic efficiencies *e<sub>m</sub>*, *e<sub>s</sub>*, and *q*<sup>2</sup> for L/D=10 WA rods striking at 1,500 m/s. Four experimental values of *P* are given for comparison.

when forward motion has ceased. Incipient tile damage can be seen halfway out from the tile center. Figure 8 gives the speeds and positions not only of the rod nose and tail but also of an axial point originally at the interface between the ceramic and the metal backing. This point begins to move a few microseconds after impact when the compression wave reaches the interface. After 60  $\mu$ s, all the ceramic has been pushed aside and it rides the rod nose until both stop together. The fact that there is finally no distance between these points in Figure 8 indicates that there is no ceramic trapped between the rod nose and the metal backing, in agreement with experiment. Figure 8 also shows that initially, the rod nose is rapidly decelerated in the hard ceramic. However, when the rod nose emerges from the back of the tile into the RHA, it picks up speed temporarily, then slows to a halt. The calculated total DOP is 6.2 cm

while the experimental value is 6.4 cm. Figure 9 can be compared with Figure 6 and shows how the stronger SiC tile delays the progress of the rod more than the weaker  $\text{Al}_2\text{O}_3$ . The final DOP for the case of Figure 9 was 5.6 cm, in agreement with experiment (Woolsey and Kokidko 1992). Again, there is no ceramic left between the remnant rod and the metal backing. In Figure 10, the confinement has been changed to Ti but the result resembles Figure 9. The lower density of Ti compared to RHA seems to allow a flatter top to the ceramic which is being pushed aside in front of the rod. Figure 11 is similar to Figure 8 although it is for SiC confined by Ti instead of  $\text{Al}_2\text{O}_3$  confined by RHA. The stronger SiC decelerates the rod even more in the first 20  $\mu\text{s}$ . Finally, there is no ceramic left between rod and backing. This was true of all the simulations carried out for ceramic/metal targets without covers struck by L/D=10 Wa rods at 1,500 m/s.

Figure 12 is a late time, 650  $\mu\text{s}$ , of the simulation shown in Figure 9. Although the details of this simulation are limited by the 1-mm cell size, the trend is clearly toward tile destruction, in agreement with what is found after an experiment. Any damaged ceramic which remains in the metal confinement after a test is off the shotline. Figures 13 and 14 show the same SiC tile subject to the same threat but without confinement at 200  $\mu\text{s}$  and 650  $\mu\text{s}$ . In Figure 13, the rear fracture cone is larger than the front cone. The remnant rod is visible at the top of Figure 13. In Figure 14, the original tile has almost completely disintegrated. Figure 15 shows the same rod about to strike an RHA plate of the same size as the ceramic tiles used. Figures 16 and 17 can be compared with Figures 13 and 14. The failure criteria used in the simulations seem to produce results which approximate the qualitative differences expected between the behavior of ductile metals and brittle ceramics subjected to ballistic impact.

In Table 2, we see the total DOP,  $P$ , and residual rod lengths,  $l$ , found for each simulation. We have also calculated the space and mass efficiencies, defined in the next paragraph, in order to compare the performance of the various targets against this particular threat. The last six cases in the table include 1-cm-thick metal covers. In a few of these, there seemed to be some ceramic left between the remnant rod and the metal backing.

In view of these simulation results, we should modify the traditional formulas for ballistic efficiencies. For the cases in Table 2, we have included the thickness of the ceramic cap in the total DOP,  $P$ , so the space efficiency becomes  $e_s = P(RHA\infty)/P$  for each case. Likewise, the mass efficiency becomes  $e_m = \rho P(RHA\infty)/\sum_i [\rho T]_i$ , where the summation in the denominator consists of three parts here. The first part is the density of the cover material times the cover thickness of 1 cm. The second part is the density

of the ceramic times the thickness of ceramic penetrated, namely, 2.54 cm minus the cap thickness. Finally, we add the density of the metal backing times  $R$ , the residual penetration into the backing. When there is a ceramic cap,  $R$  is measured from the original tile/backing interface position (here 3.54) to the top of the cap. This definition reduces to the usual definition when the cap thickness is zero and tends to be on the conservative side for the cases we are dealing with.

The last column in Table 2 gives the quality factor for each case, namely, a combination of mass and space efficiencies  $q^2 = e_m e_s$ . Here semi- $\infty$  Ti has a higher  $q^2$  than RHA, while the semi- $\infty$  Al  $q^2$  is lower. Very high  $q^2$  values were calculated for the semi- $\infty$  ceramic blocks. Such cases are curiosities, since ceramics are too brittle to be used alone in practical multihit armors, even if such large blocks could be manufactured at a reasonable cost. Consequently, they have been omitted here.

The next six cases in Table 2 are for ceramic tiles in metal surrounds without metal covers. There alumina in Al has no better  $q^2$  value than RHA, since its higher mass efficiency is offset by its lower space efficiency. Except for one other case involving Al, the remaining simulations have space efficiencies as good as or better than RHA and  $q^2$  values ranging from 1.5 to 3.0. We recall that the case of SiC in RHA has been established experimentally as well as computationally.

Since practical armors require cover plates, we can move on to the last six cases. Once again, the alumina surrounded by Al has no better  $q^2$  value than RHA for the same reason as before. It is interesting to note that adding 1-cm covers on  $\text{Al}_2\text{O}_3$ , using the same metal as the backing, gives no improvement over the corresponding cases without covers. At least the practical requirement of covers does not hurt, since the  $q^2$  values are unchanged. However, when we add covers to SiC, using the same metal as the backing, we see  $q^2$  value improvements compared to the corresponding cases without covers. Only the use of Al back and front gives  $e_s$  values less than 1.0 in this group.

These simulations are idealized in many respects. For example, one shortcoming is the inability to model thin layers of epoxy or other materials which are commonly used at ceramic/metal interfaces. We expect to overcome a good part of this limitation in the future by using domain decomposition, a technique which uses small cell sizes only in those parts of a computational grid where they are required. This could be a significant improvement over the rather restricted subgridding techniques which are currently available.

#### 4. SIMULATIONS INVOLVING RODS OF VARIOUS L/D RATIOS AND STRIKING SPEEDS

While Table 2 offers food for thought, we must remember that even for WA rods striking the center of a symmetrical target at 0° obliquity, there are variations which could look less promising. For example, suppose the same rods strike the same targets at higher or lower speeds. Or suppose the L/D ratio is smaller or larger. In this section, we will examine some simulations involving the same rod striking at a lower speed as well as some cases of shorter and longer rods striking at different speeds.

Table 3 shows the same sort of information as Table 2, but for L/D=10 WA rods striking at 1,000 m/s. Under these conditions, ceramics in metals without covers all defeated such a slow rod. Figures 20 and 21 illustrate this point for alumina in RHA. These figures may be compared with Figures 7 and 8. Here we are interested in checking how well the last three more practical targets in Table 3 performed against this threat. In these cases too, the metal backing was penetrated by having unperforated ceramic pushed into it with the rod greatly overmatched and stopped in the ceramic. This is illustrated in Figure 22. The  $e_m$  value for the target in Figure 22 is lower than for the target in Figure 23 (without cover) because the density of the metal cover is greater than the density of the SiC tile. The reverse is true of an Al surround, so this appears better than Ti for this particular threat.

Table 3. L/D=10 WA Rods Striking at 1,000 m/s

Target	$P$ (cm)	$l$ (cm)	$e_m$	$e_s$	$q^2$
RHA $\infty$	3.4	2.3	1.0	1.0	1.0
Ti $\infty$	4.0	2.6	1.5	0.8	1.2
Al $\infty$	11.0	4.0	0.9	0.3	0.3
1-cm RHA on 2.54-cm SiC in RHA $\infty$	3.9	1.6	1.7	0.9	1.5
1-cm Ti on 2.54-cm SiC in Ti $\infty$	4.0	1.4	2.3	0.8	1.8
1-cm Al on 2.54-cm SiC in Al $\infty$	4.3	1.4	2.5	0.8	2.0

Note: Penetration depths  $P_2$ , residual rod lengths  $l$ , and ballistic efficiencies  $e_m$ ,  $e_s$ , and  $q^2$  for L/D=10 WA rods striking at 1,000 m/s. No comparisons with experiment were available.

Tables 4 and 5 show some simulations involving an L/D=3.2 WA rod striking similar targets at 1,500 and 1,000 m/s. Penetration into semi- $\infty$  RHA at 1,500 m/s was 7.5 cm compared to an experimental value of 7.2 cm. At 1,000 m/s it was 4.3 cm, compared to an experimental value of 4.0 cm. Again, our main interest here is checking the performance of a shorter rod against SiC tiles in Ti. As we can see from these tables, the total penetration is slightly greater with a cover than without at both impact speeds.

Figures 24–29 show this short rod impacting an SiC tile in Ti at 1,500 m/s with and without a Ti cover. The  $q^2$  values in Table 4 are reasonably good, while those in Table 5 are better, even with a cover.

Table 4. L/D=3.2 WA Rods Striking at 1,500 m/s

Target	exper. $P$ (cm)	$P$ (cm)	$l$ (cm)	$e_m$	$e_s$	$q^2$
RHA $\infty$	7.2	7.5	1.4	1.0	1.0	1.0
2.54-cm SiC in Ti $\infty$	—	7.2	1.5	2.3	1.0	2.3
1-cm Ti on 2.54 cm SiC in Ti $\infty$	—	7.5	1.9	2.0	1.0	2.0

Note: Penetration depths  $P$ , residual rod lengths  $l$ , and ballistic efficiencies  $e_m$ ,  $e_s$ , and  $q^2$  for L/D=3.2 WA rods striking at 1,500 m/s. One experimental value of  $P$  is given for comparison.

Table 5. L/D=3.2 WA Rods Striking at 1,000 m/s

Target	exper. $P$ (cm)	$P$ (cm)	$l$ (cm)	$e_m$	$e_s$	$q^2$
RHA $\infty$	4.0	4.3	2.5	1.0	1.0	1.0
2.54-cm SiC in Ti $\infty$	—	3.4	1.2	4.4	1.3	5.7
1-cm Ti on 2.54 cm SiC in Ti $\infty$	—	4.0	0.6	4.7	1.1	5.2

Note: Penetration depths  $P$ , residual rod lengths  $l$ , and ballistic efficiencies  $e_m$ ,  $e_s$ , and  $q^2$  for L/D=3.2 WA rods striking at 1,000 m/s. One experimental value of  $P$  is given for comparison.

Figure 30 shows an L/D=20 WA rod about to impact at 1,612 m/s on a target of a somewhat different design than we have seen so far. It consists of 4.0-cm-thick alumina tile surrounded by RHA, including a 1.27-cm-thick RHA cover inset 1.27 cm from the origin on the axis. Figure 31 shows the final position

of the rod in the backing, while Figure 32 shows the final DOP to be 10.8 cm measured from the origin. The residual penetration into the backing is 4.3 cm, compared to an experimental value of 4.15 cm. This is our check point for the simulation in Tables 6 and 7. Our reference simulation in Table 6 is semi- $\infty$  RHA shown in Figure 34. The depth of 9.4 cm compares with 9.7 cm found experimentally. The second target in Table 6 is illustrated by Figures 35–37, while the third target appears in Figures 38–40. No ceramic caps appeared in any of these simulations. The  $q^2$  value of 2.6 is comparable to the value 2.0 for the same target against the L/D=3.2 rod in Table 4. In Figure 36, we see that the code allows failed material to "heal" unphysically at a later time.

Table 6. L/D=20 WA Rods Striking at 1,500 m/s

Target	exper. $P$ (cm)	$P$ (cm)	$l$ (cm)	$e_m$	$e_s$	$q^2$
RHA $\infty$	9.7	9.4	1.6	1.0	1.0	1.0
2.54-cm SiC in Ti $\infty$	—	7.7	1.7	2.3	1.2	2.8
1-cm Ti on 2.54-cm SiC in Ti $\infty$	—	7.8	2.0	2.2	1.2	2.6

Note: Penetration depths  $P$ , residual rod lengths  $l$ , and ballistic efficiencies  $e_m$ ,  $e_s$ , and  $q^2$  for L/D=20 WA rods striking at 1,500 m/s. One experimental value of  $P$  is given for comparison.

Table 7 is similar to Table 6 except for the speed of 1,000 m/s. It is interesting to note that the penetration in semi- $\infty$  RHA in Table 7 is the same as for the L/D=10 rod in Table 3 at this speed, since they had the same mass, namely, 65 g. The L/D=3.2 rod in Table 4 had a mass of 213 g and penetrated more deeply at this impact speed. Once again, we see that the 2.54-cm ceramic tile in a metal surround overmatches a slow rod, as shown by the  $q^2$  value for the second target and Figure 41. Figure 42 shows how the addition of a Ti cover plate allows the same penetration into the ceramic tile, but adds penetration of the cover plate and so lowers the efficiency.

Table 7. L/D=20 WA Rods Striking at 1,000 m/s

Target	$P$ (cm)	$l$ (cm)	$e_m$	$e_s$	$q^2$
RHA $\infty$	3.4	2.6	1.0	1.0	1.0
2.54-cm SiC in Ti $\infty$	2.8	1.4	6.3	1.2	7.5
1-cm Ti on 2.54-cm SiC in Ti $\infty$	3.8	0.2	3.1	0.9	2.8

Note: Penetration depths  $P$ , residual rod lengths  $l$ , and ballistic efficiencies  $e_m$ ,  $e_s$ , and  $q^2$  for L/D=20 WA rods striking at 1,000 m/s. No comparisons with experiment were available.

## 5. SIMULATIONS OF WAVE MOTION IN IMPACT PROBLEMS

In this section, we will use some of the tools which are available in the HULL code to explore the possible influence of wave phenomena on the ballistic performance of targets employing ceramics.

Figures 43–45 show pressure contours of  $10^8$  dyne/cm<sup>2</sup> (10 MPa or 100 times atmospheric pressure). These contours are just one part of the wave system which propagates in front of the L/D=10 WA rod which has struck at 1,500 m/s three different targets: RHA, Ti, and SiC. Since the bulk sound velocity of RHA and Ti are about the same, there are only minor differences between Figures 43 and 44. In Figure 45, the wave has clearly progressed farther into the target since the bulk sound speed of SiC is more than 50% higher than that of RHA or Ti. Such small amplitude waves are of no importance to our problem, since the stresses they produce are much lower than the yield or failure stresses in Table 1. Of more interest is the large amplitude wave which follows the elastic precursor. The speed of this wave depends on its strength. For ceramics, the experiments carried out by Gust and coworkers are helpful (Gust, Holt, and Royce, 1973; Gust and Royce 1971), since they show this dependence.

Figures 46–49 show both the elastic precursor and the stronger wave which follows. These are pressure histograms along the shotline in front of the rod. The subtitle above the right half of these figures shows the actual location to be 0.05 cm off the axis. This is the center of the first column of cells in the simulation grid. In Figure 46, the pressure a few millimeters in front of the rod nose peaks near  $5 \times 10^{10}$  dyne/cm<sup>2</sup>, 5 GPa, or 500 times the amplitudes shown in Figures 43–45. The front of the wave in Figure 51 (10  $\mu$ s) after impact corresponds closely to the front of the wave in Figure 44 at the same time, showing how relatively unimportant the elastic precursor is. According to Figure 47, the precursor has already developed a small negative or tensile component about 3 cm behind the leading edge. In Figure 48 (20  $\mu$ s after impact), the wave system has progressed, but little else has changed. In Figure 49, the front of the wave system is the superposition of one part still approaching the rear surface and another part reflected from the rear surface.

Figure 50 is similar to Figure 44 except that a 1-cm-thick SiC tile has been inserted in the Ti block. A comparison with Figures 44 and 45 shows that the position of the wave front in Figure 50 is intermediate between the positions in Figures 44 and 45 since some time has been spent moving at a higher speed in SiC and some time has been spent moving at a lower speed in Ti. We also see that reflection and refraction have occurred at the interface, following the usual laws of small-amplitude

acoustics. The same event shown in Figure 50 is shown again in Figure 51 in the form of a histogram along the axis. Although the wave has been split into transmitted and reflected components by the interface, the pressure on both sides of the interface is still positive, at least along the shotline. Figure 51 may be compared to Figures 47 and 48, where there are no interfaces and thus no reflections. However, a few centimeters off the shotline as shown in Figure 52, strong tensile waves have been generated, especially on the ceramic side of the interface. If we were able to represent the interface more realistically, including a 0.1-cm-thick layer of epoxy as used in experiments, we might see some incipient separation at this time.

Figure 53 shows the same event as Figures 50–52 from still another viewpoint. Here we see pressure histograms for two horizontal lines just below and just above the ceramic/metal interface. In the right half of the figure on the metal side, the pressure is positive on the axis and radially outward until about 2 cm when it turns negative. In the left half of the figure on the ceramic side, the pressure at the axis is positive (about  $6 \times 10^{10}$  dynes/cm<sup>2</sup>) and larger than on the metal side, in agreement with Figure 51 which shows only pressure at the axis. Just off the axis we see in Figure 53 that the superposition of incoming and reflected waves has resulted in a strong tensile wave. However, farther from the axis the net pressure is still positive at this time. Figure 54 shows the same scene 10  $\mu$ s later (20  $\mu$ s after impact) while the rod nose is still approaching the interface. The vertical scales of Figures 53 and 54 are different. However, it is clear that on the metal side, the pressure is about the same at the axis, although it turns negative closer to the axis than before. On the ceramic side, the scene is similar to before, although the net tensile wave near the axis is stronger than it was earlier.

## 6. SUMMARY

In this report, we have illustrated the use of the wavecode HULL to simulate various ceramic-in-metal targets impacted centrally at 0° obliquity at two different speeds by WA rods of three different L/D ratios. In a limited number of cases we were able to compare our simulations with experiments and found reasonable agreement. This encouraged us to extrapolate our simulations into unexplored territory, including some cases with ceramic caps.

One might argue that such caps could make the rod more effective by providing harder noses to penetrate deeper into the metal. On the other hand, there might be enough rod energy wasted in forming these caps that it would favor the target. Backman et al. (1992) have reported various observations of caps formed during penetration and have even proposed a tentative theory.

We have also given some illustrations of how time- and space-dependent wave patterns might influence the outcome of ballistic simulations and perhaps experiments. This is an area in which computer simulations might prove helpful to experimentation, so our future plans include further work along these lines.

## 7. RECOMMENDATIONS

Even within the context of  $0^\circ$  impacts on centers of symmetry, our simulations are not complete. We hope to expand the present work to include other thicknesses as well as other ceramics, and multiple tiles as well as single tiles. Future plans also include simulations of off-center impacts and a variety of obliquities, using depleted uranium and steel rods as well as WA rods.

Of necessity, the present report has treated the ceramic/metal bond as perfect. In practice, adhesives are often used without regard to impedance matching. We would advocate an experimental study using various techniques to maintain an impedance match which is fairly close and should not be worsened by an adhesive. Various metallizing processes could be used. Hot-press bonding as well as graded powder bonding or diffusion bonding should also be investigated. Some targets should be sectioned to see whether the notion of a ceramic cap is real.

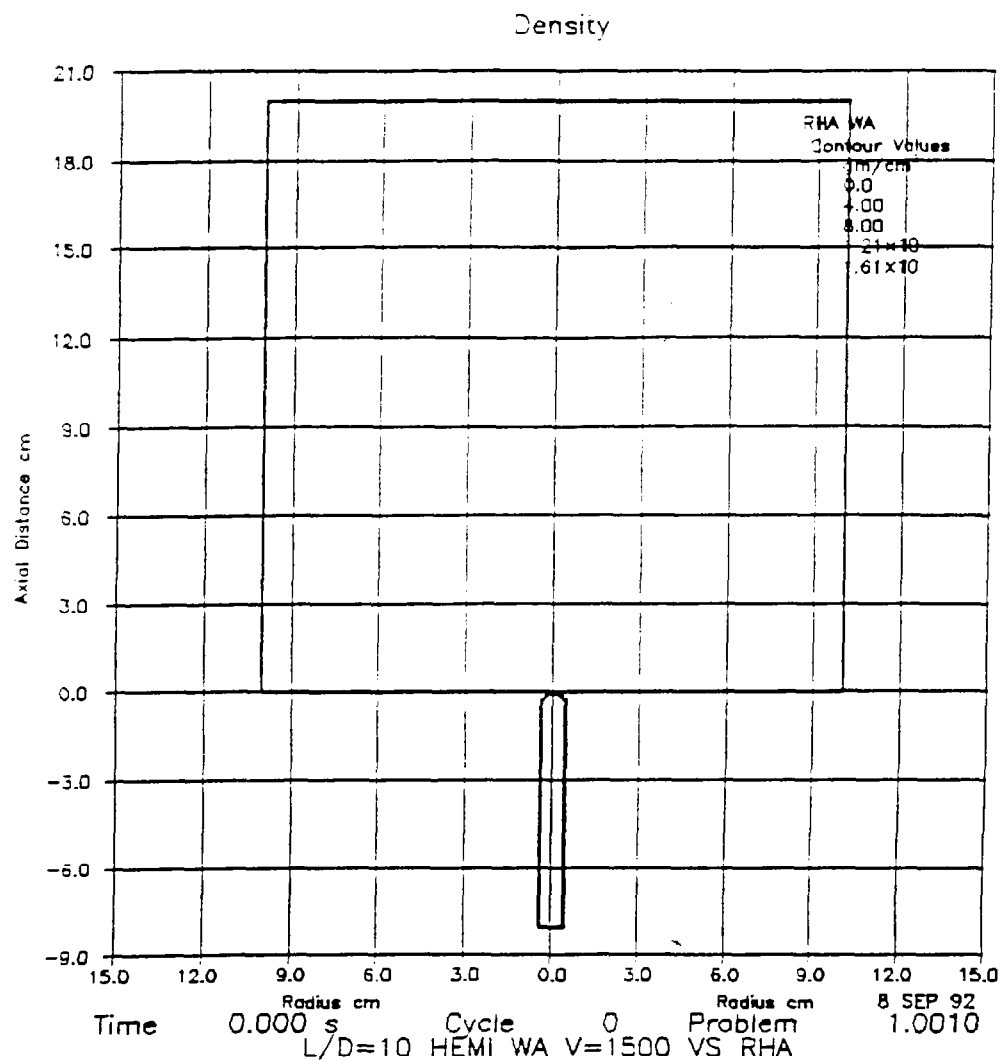


Figure 1. L/D=10 WA rod at 1,500 m/s against  $\infty$  RHA at 0 time.

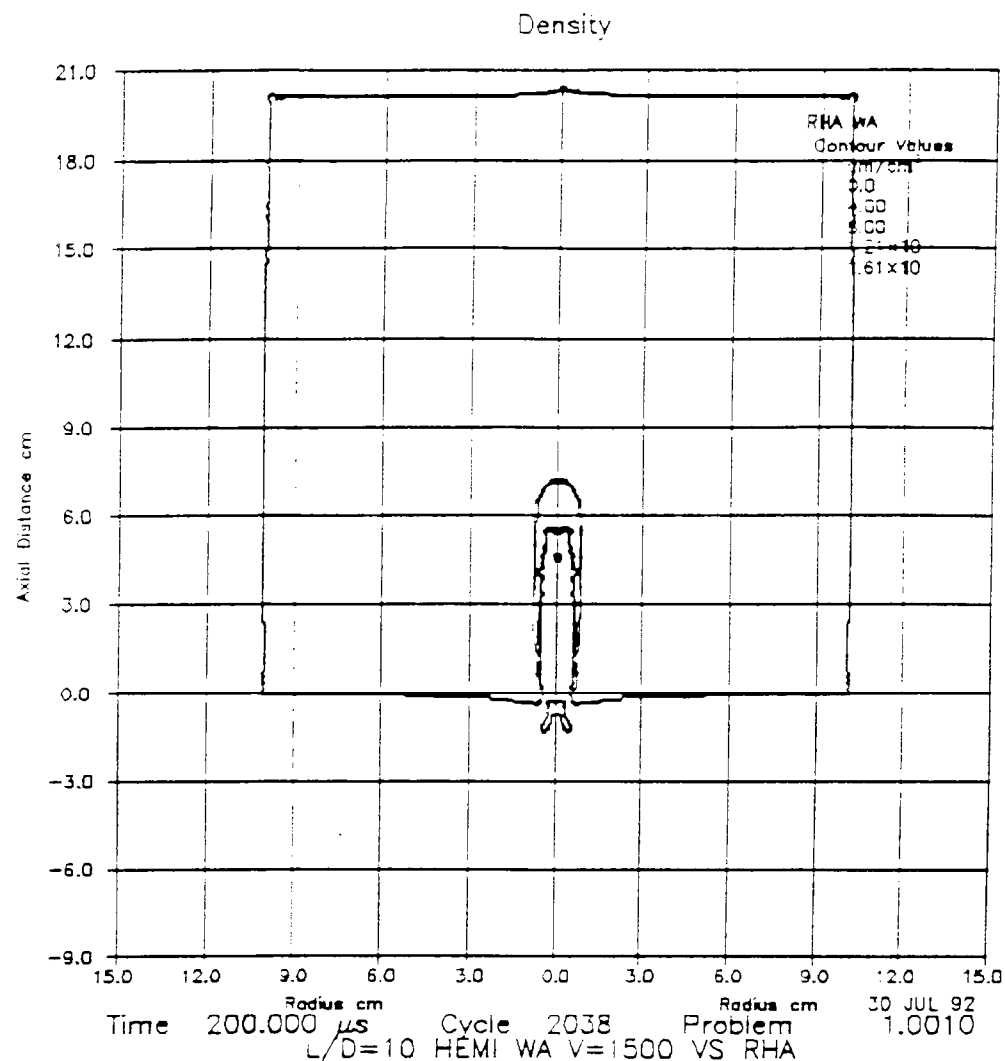


Figure 2. L/D=10 WA rod at 1,500 m/s against  $\infty$  RHA at 200  $\mu$ s.

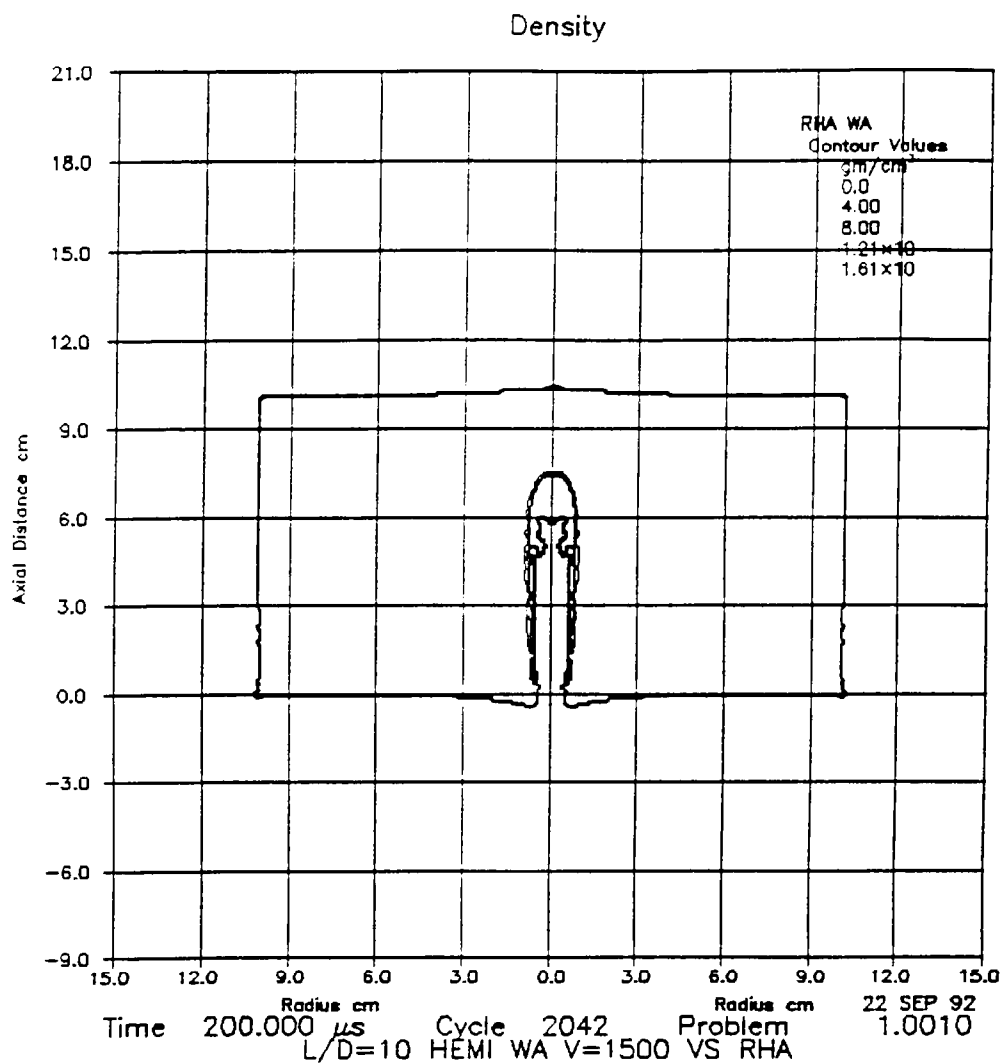


Figure 3. L/D=10 WA rod at 1,500 m/s against 10-cm RHA at 200  $\mu$ s.

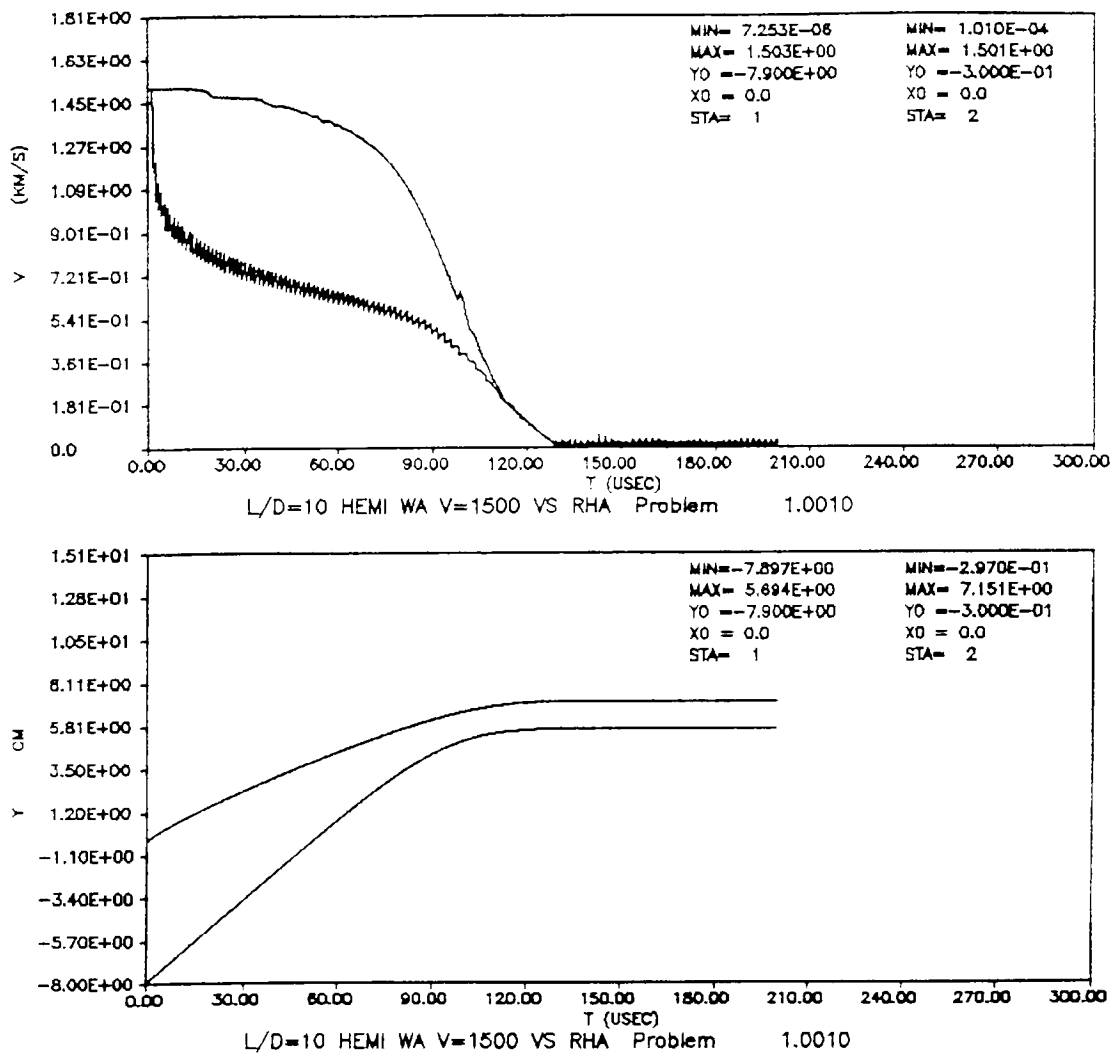


Figure 4. L/D=10 WA rod at 1,500 m/s against RHA: speed and position of rod nose and tail as a function of time.

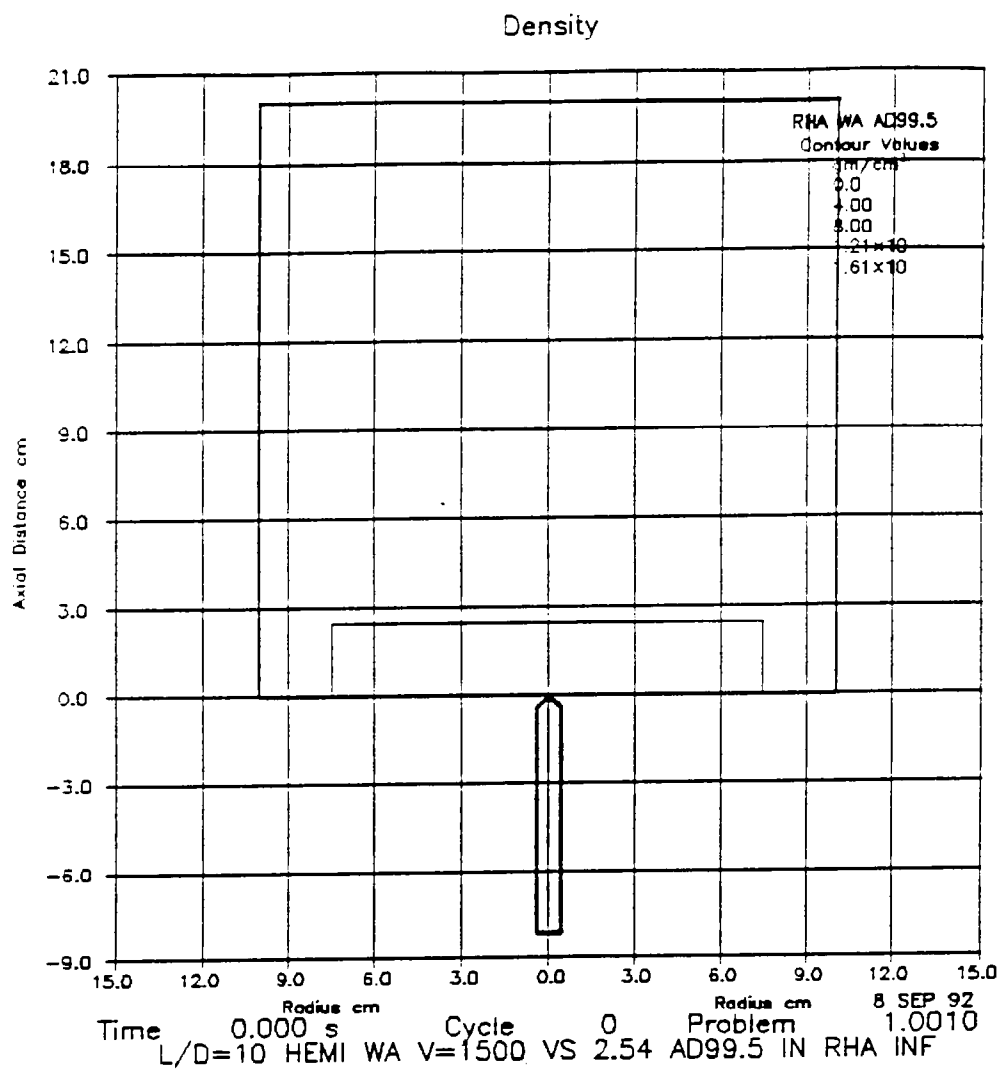


Figure 5. L/D=10 WA rod at 1,500 m/s against 2.54-cm AD99.5 in  $\infty$  RHA at 0 time.

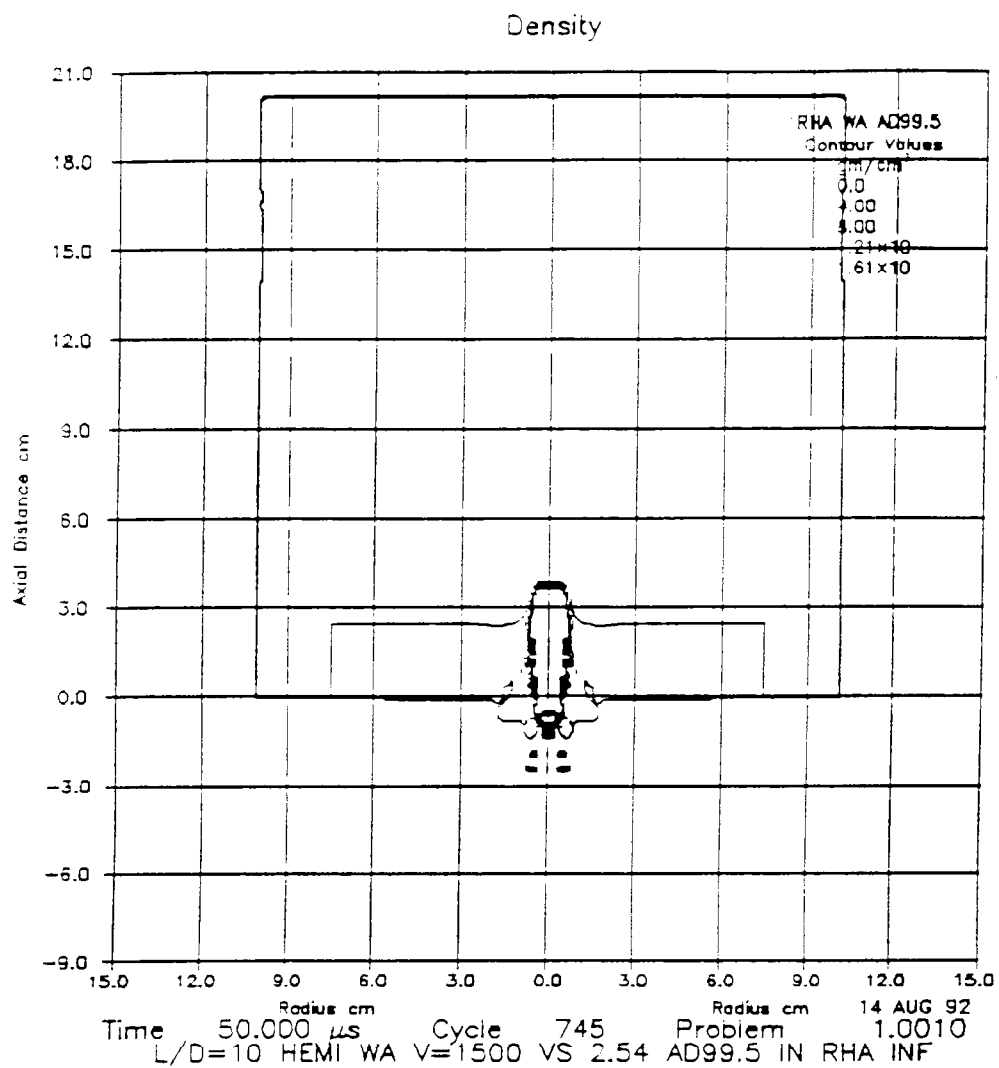


Figure 6. L/D=10 WA rod at 1,500 m/s against 2.54-cm AD99.5 in  $\infty$  RHA at 50  $\mu$ s.

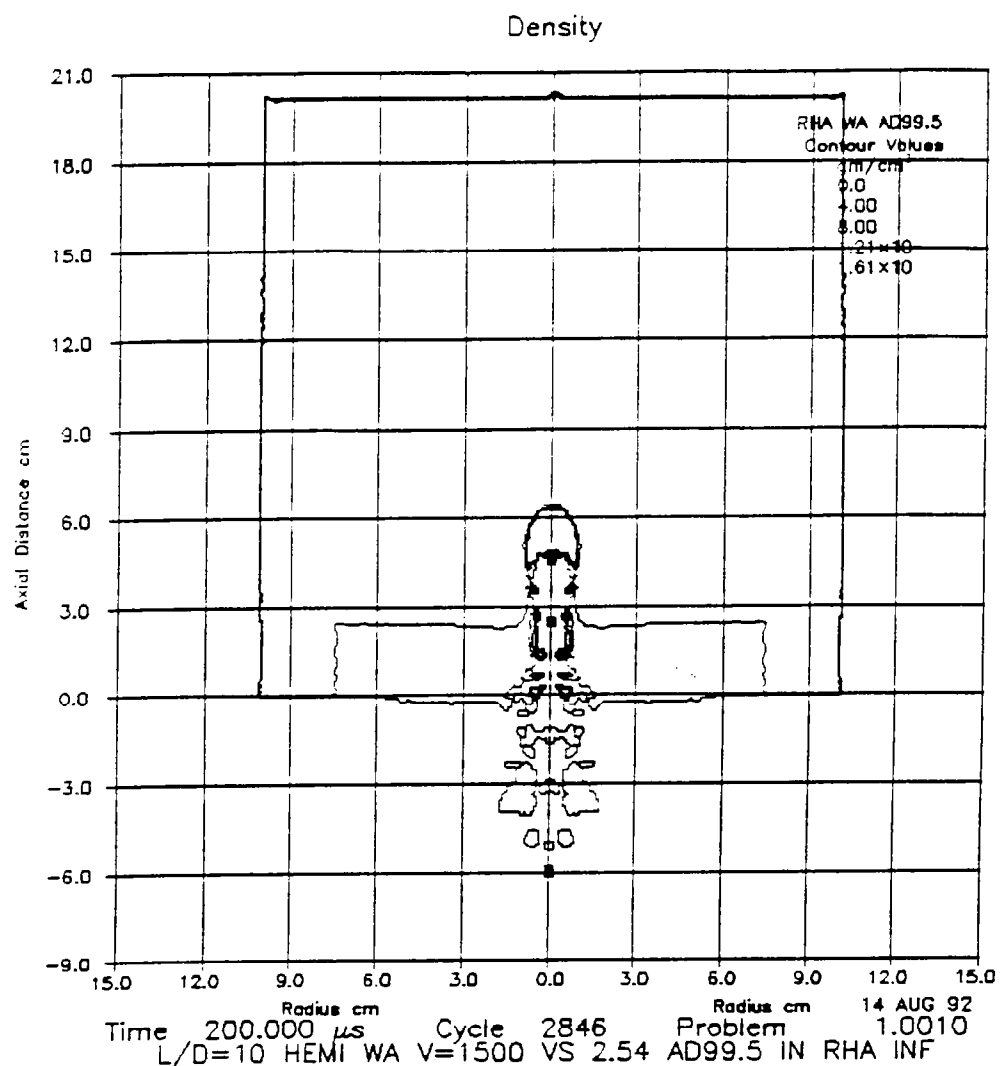


Figure 7. L/D=10 WA rod at 1,500 m/s against 2.54-cm AD99.5 in  $\infty$  RHA at 200  $\mu$ s.

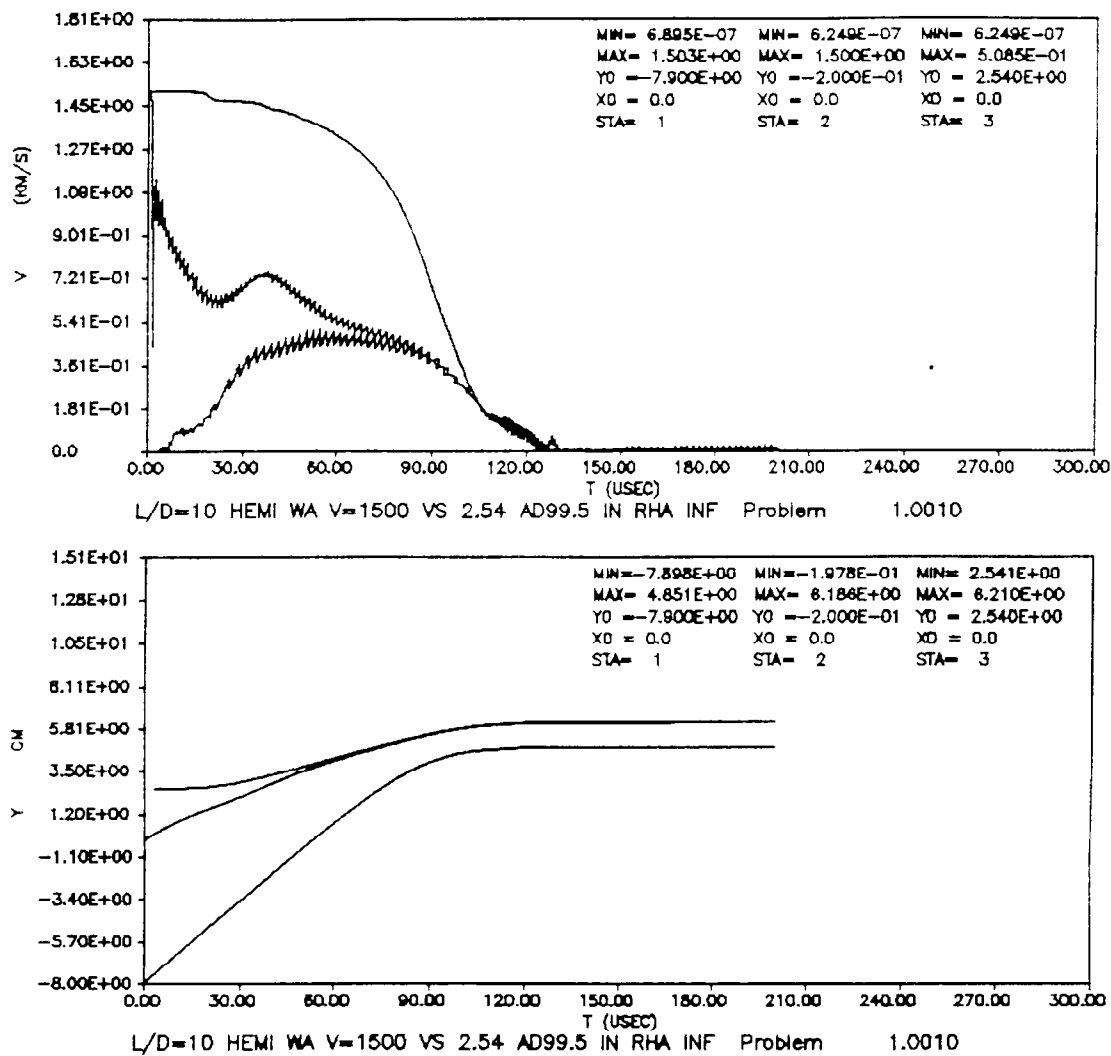


Figure 8. L/D=10 WA rod at 1,500 m/s against 2.54-cm AD99.5 in  $\infty$  RHA: speed and position of rod nose and tail and tile back vs. time.

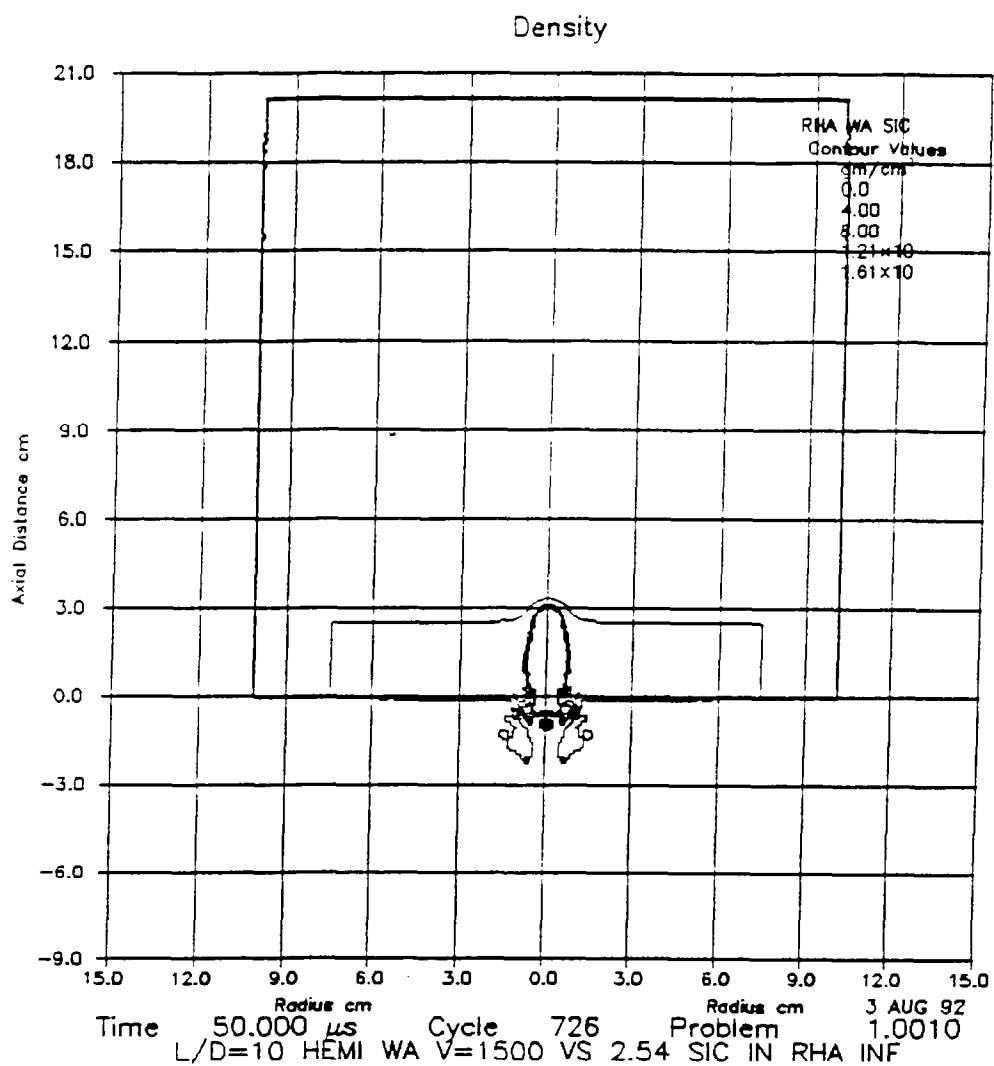


Figure 9. L/D=10 WA rod at 1,500 m/s against 2.54-cm SiC in  $\infty$  RHA at 50  $\mu$ s.

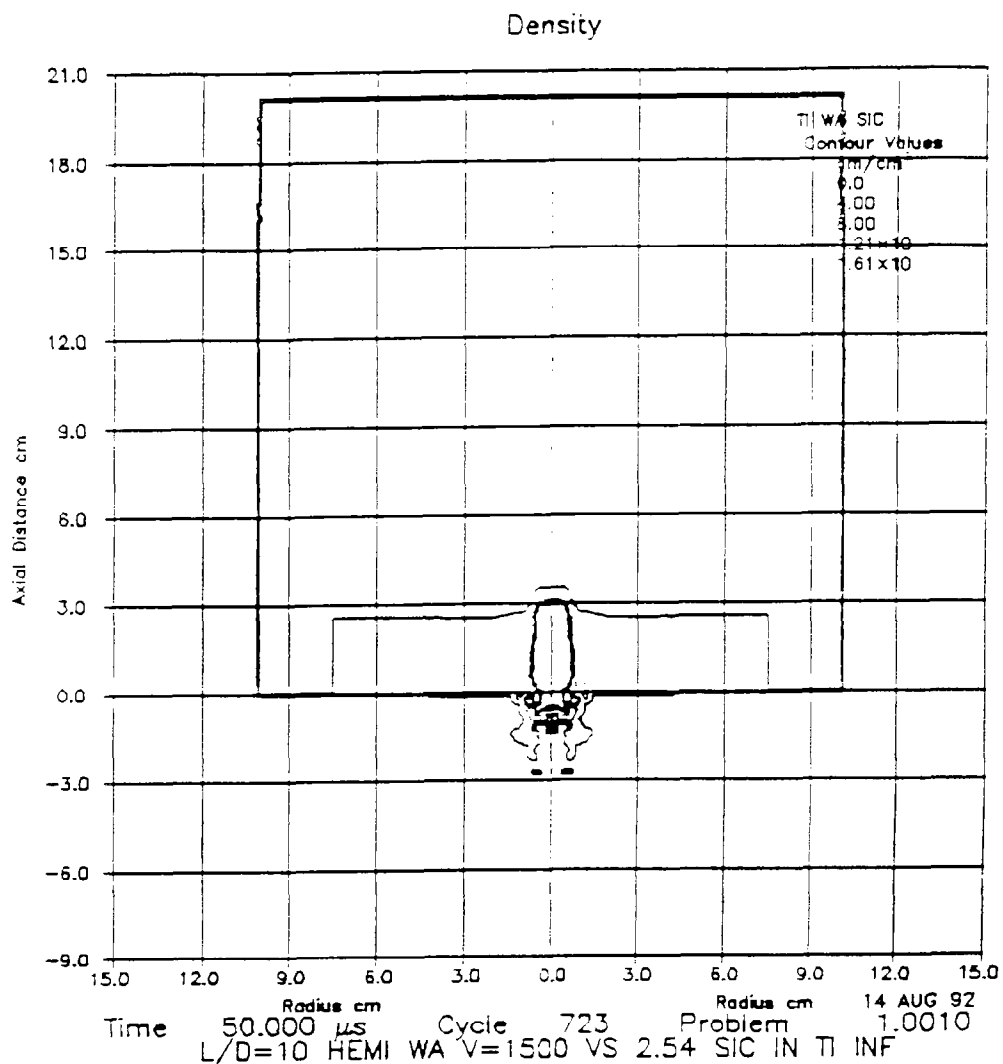


Figure 10. L/D=10 WA rod at 1,500 m/s against 2.54-cm SiC in  $\infty$  Ti at 50  $\mu$ s.

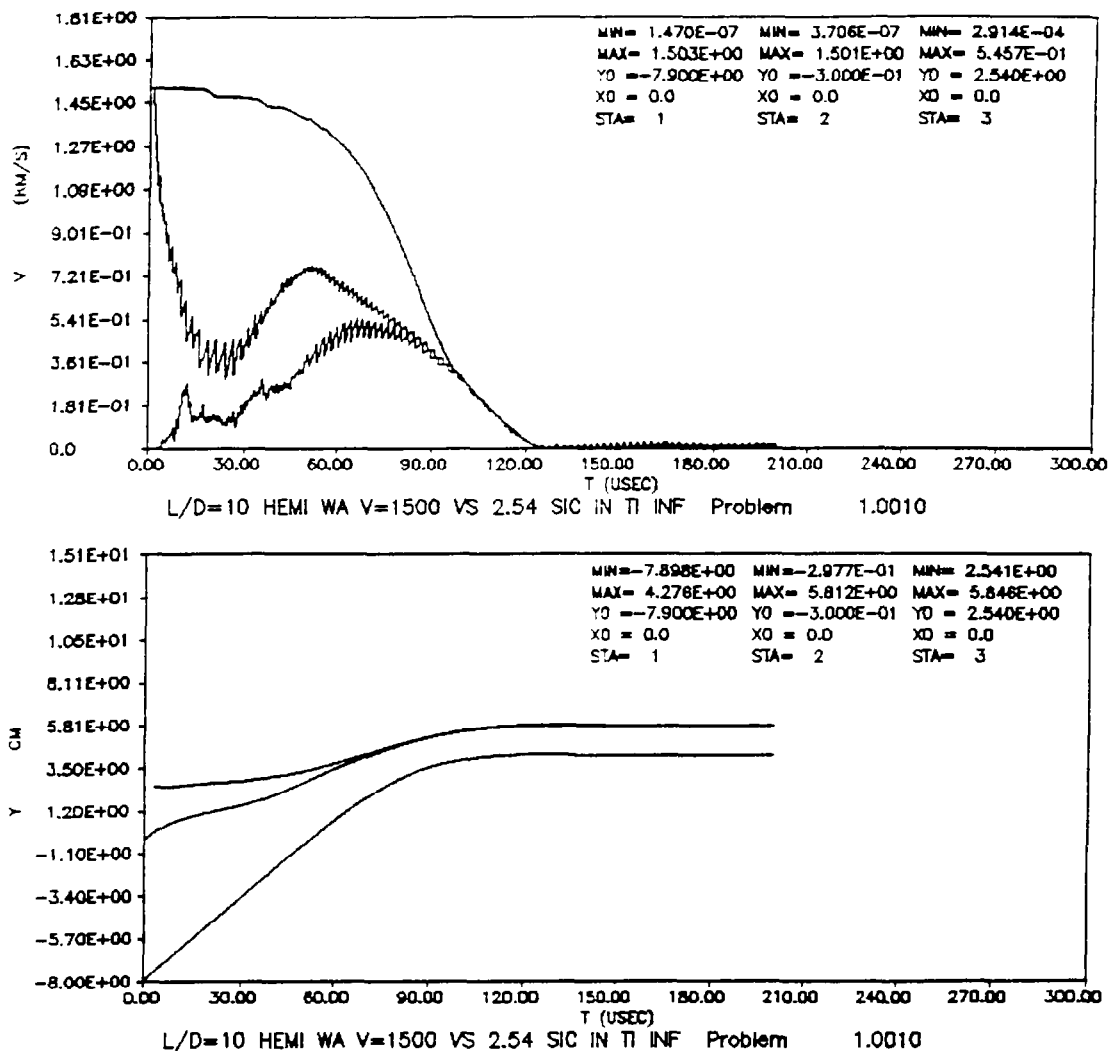


Figure 11. L/D=10 WA rod at 1,500 m/s against 2.54-cm AD99.5 in  $\infty$  Ti: speed and position of rod nose and tail and tile back vs. time.

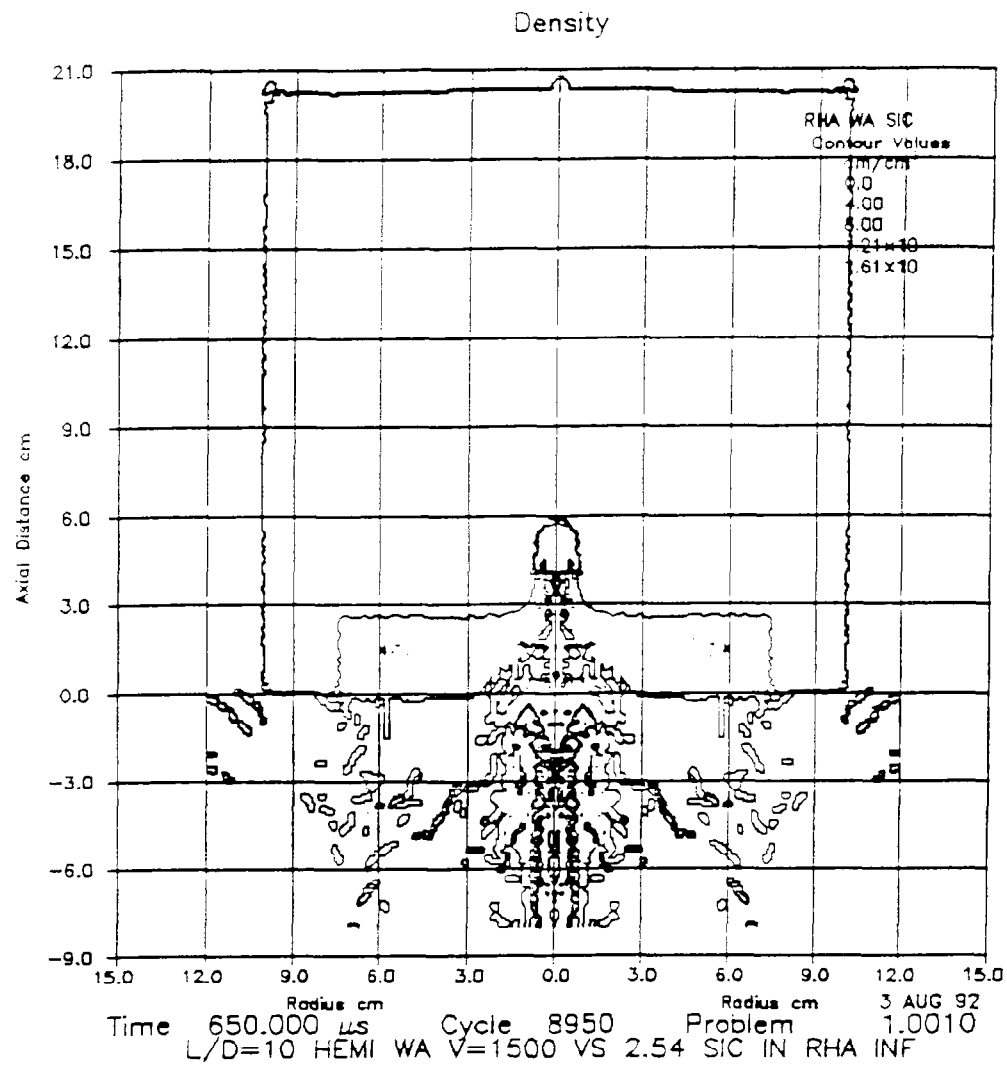


Figure 12. L/D=10 WA rod at 1,500 m/s against 2.54-cm SiC in  $\infty$  RHA at 650  $\mu$ s.

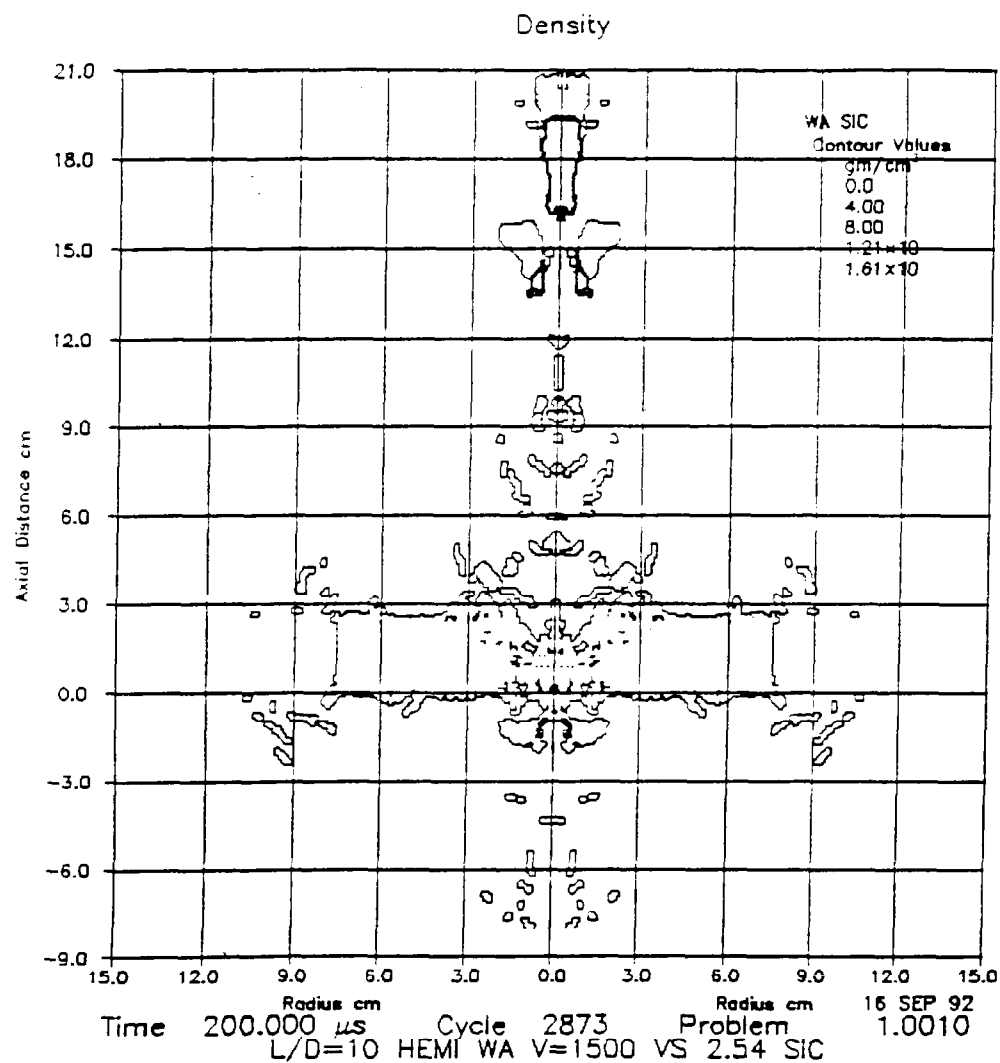


Figure 13. L/D=10 WA rod at 1,500 m/s against 2.54-cm SiC at 200  $\mu$ s.

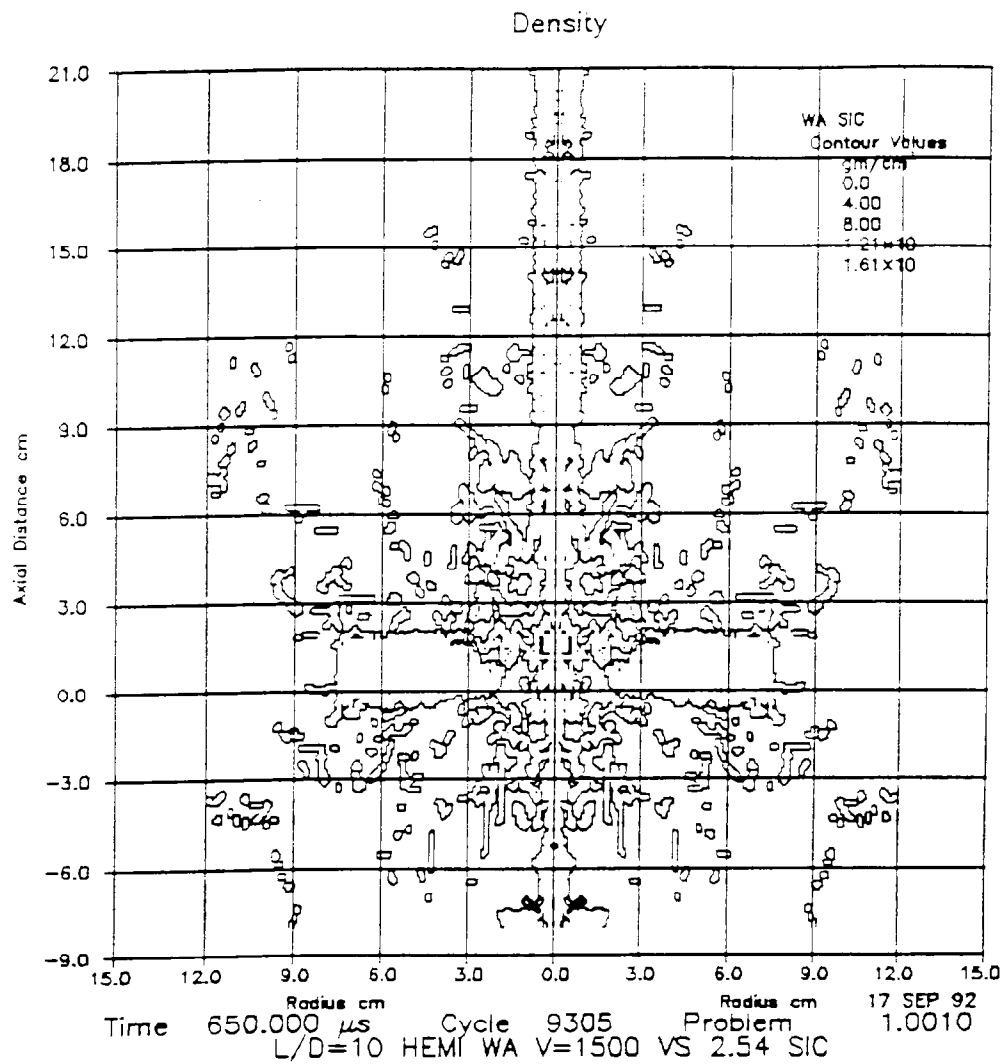


Figure 14. L/D=10 WA rod at 1,500 m/s against 2.54-cm SiC at 650  $\mu$ s.

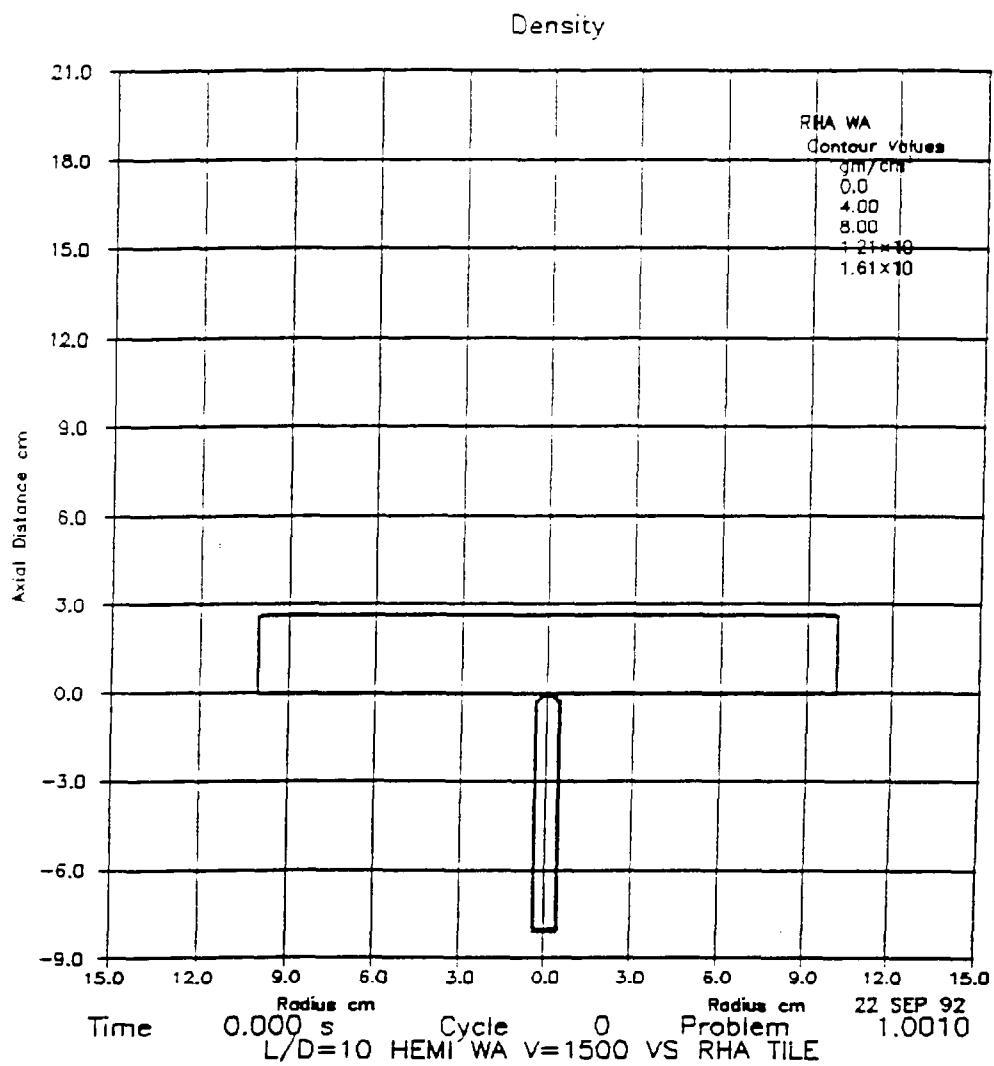


Figure 15. L/D=10 WA rod at 1,500 m/s against 2.54-cm RHA at 0  $\mu$ s.

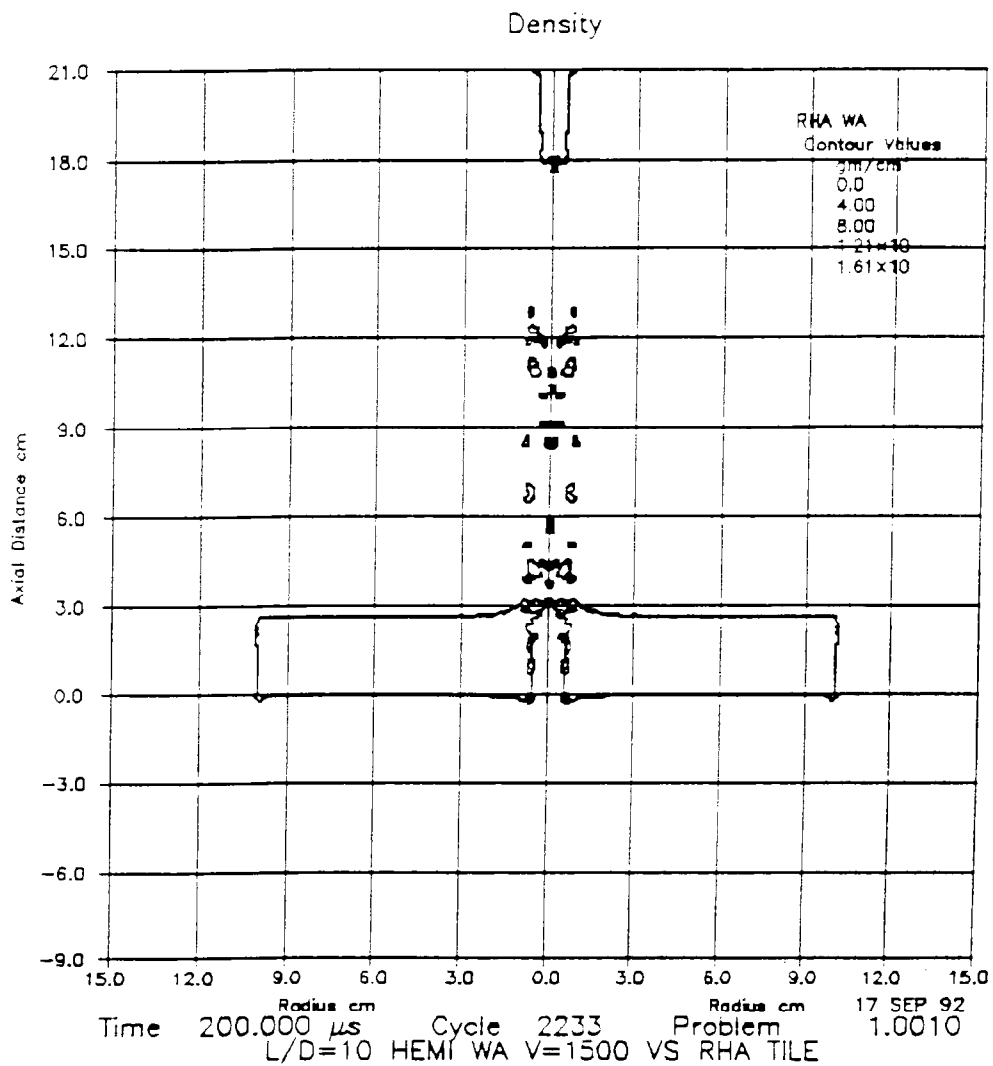


Figure 16. L/D=10 WA rod at 1,500 m/s against 2.54-cm RHA at 200  $\mu$ s.

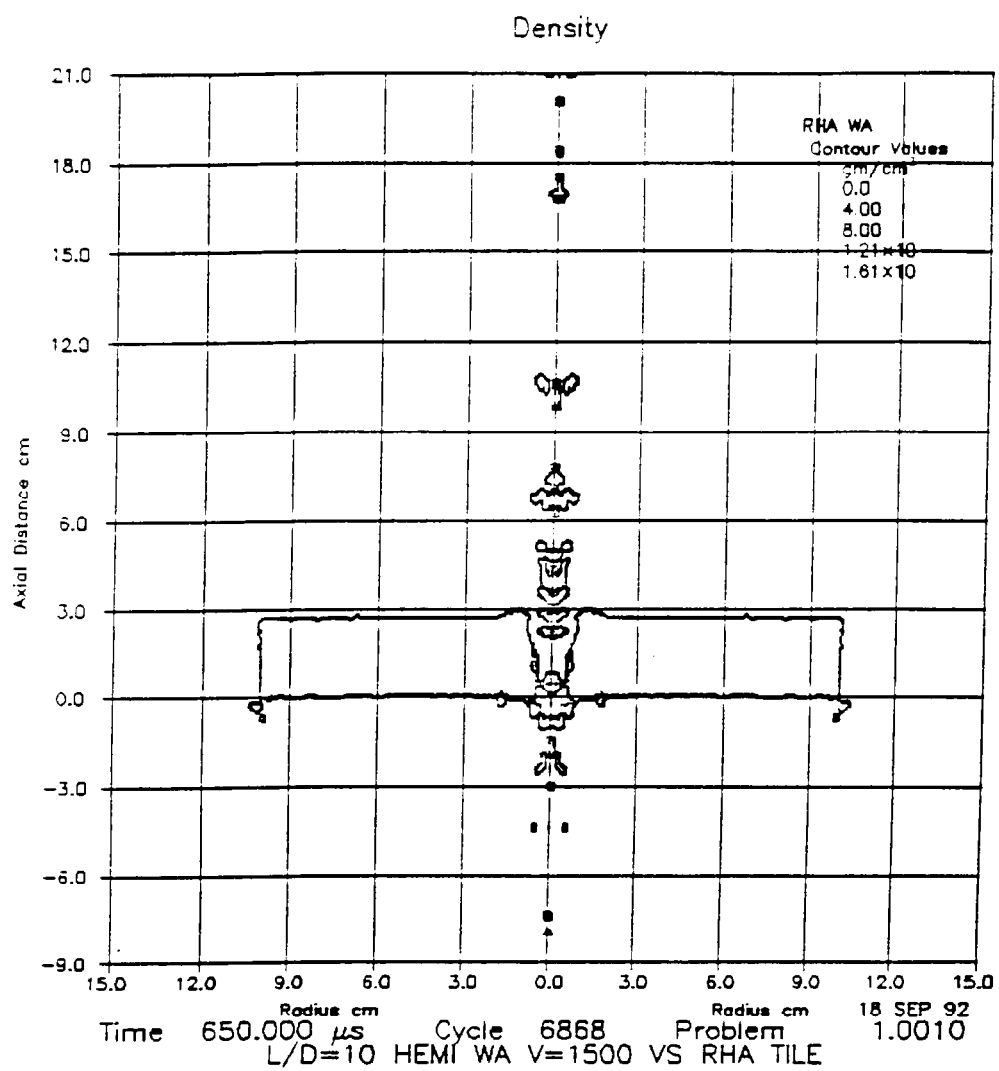


Figure 17. L/D=10 WA rod at 1,500 m/s against 2.54-cm RHA at 650  $\mu$ s.

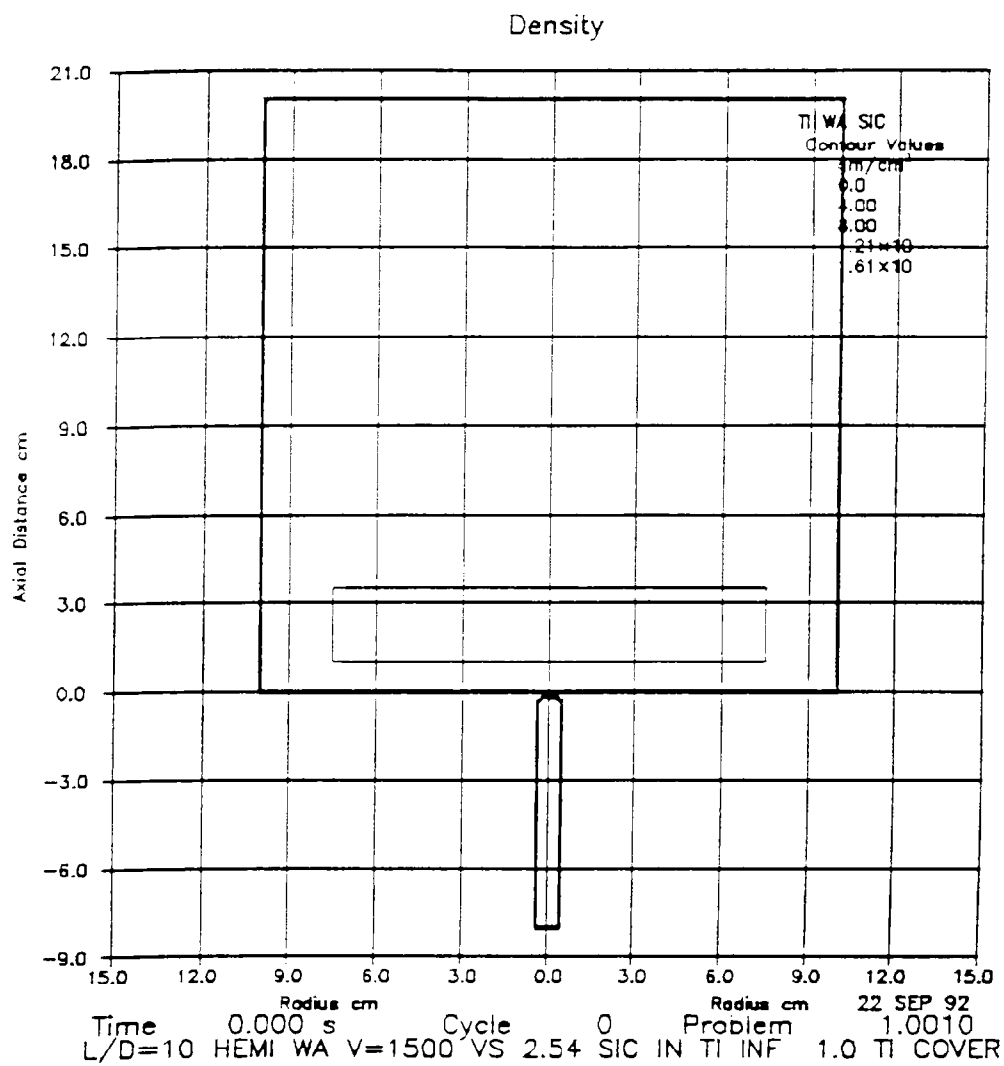


Figure 18. L/D=10 WA rod at 1,500 m/s against 2.54-cm SiC in  $\infty$  Ti covered by 1-cm Ti at 0 time.

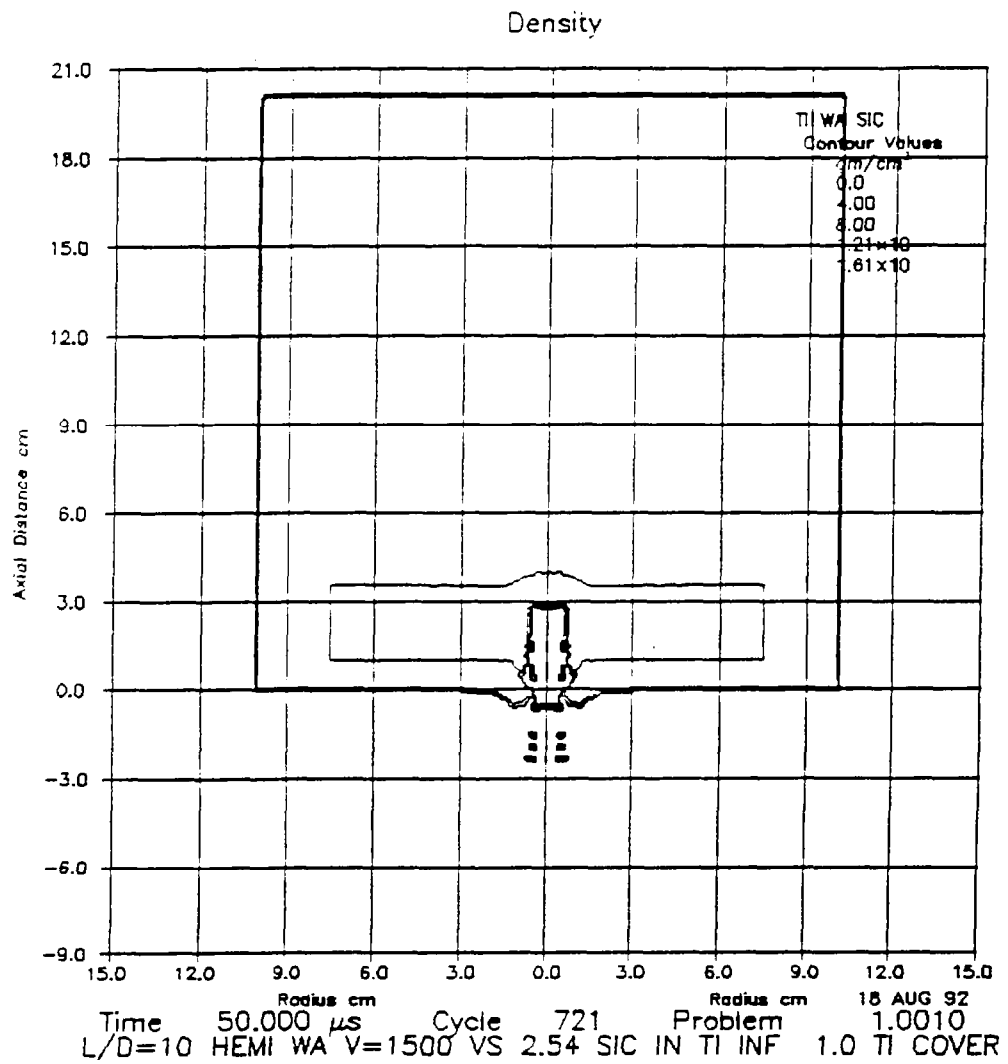


Figure 19. L/D=10 WA rod at 1,500 m/s against 2.54-cm SiC in  $\infty$  Ti covered by 1-cm Ti at 50  $\mu$ s.

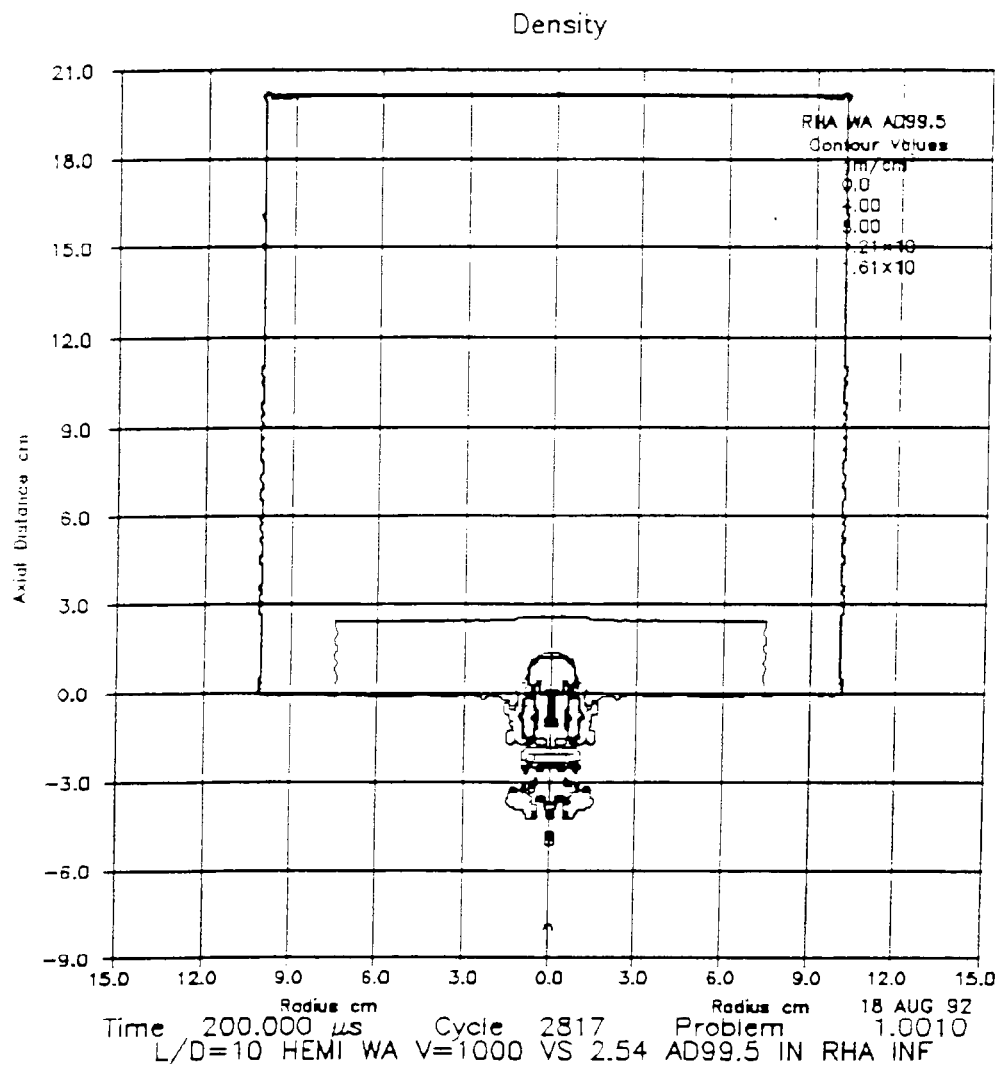


Figure 20. L/D=10 WA rod at 1,000 m/s against 2.54-cm AD99.5 in  $\infty$  RHA at 200  $\mu$ s.

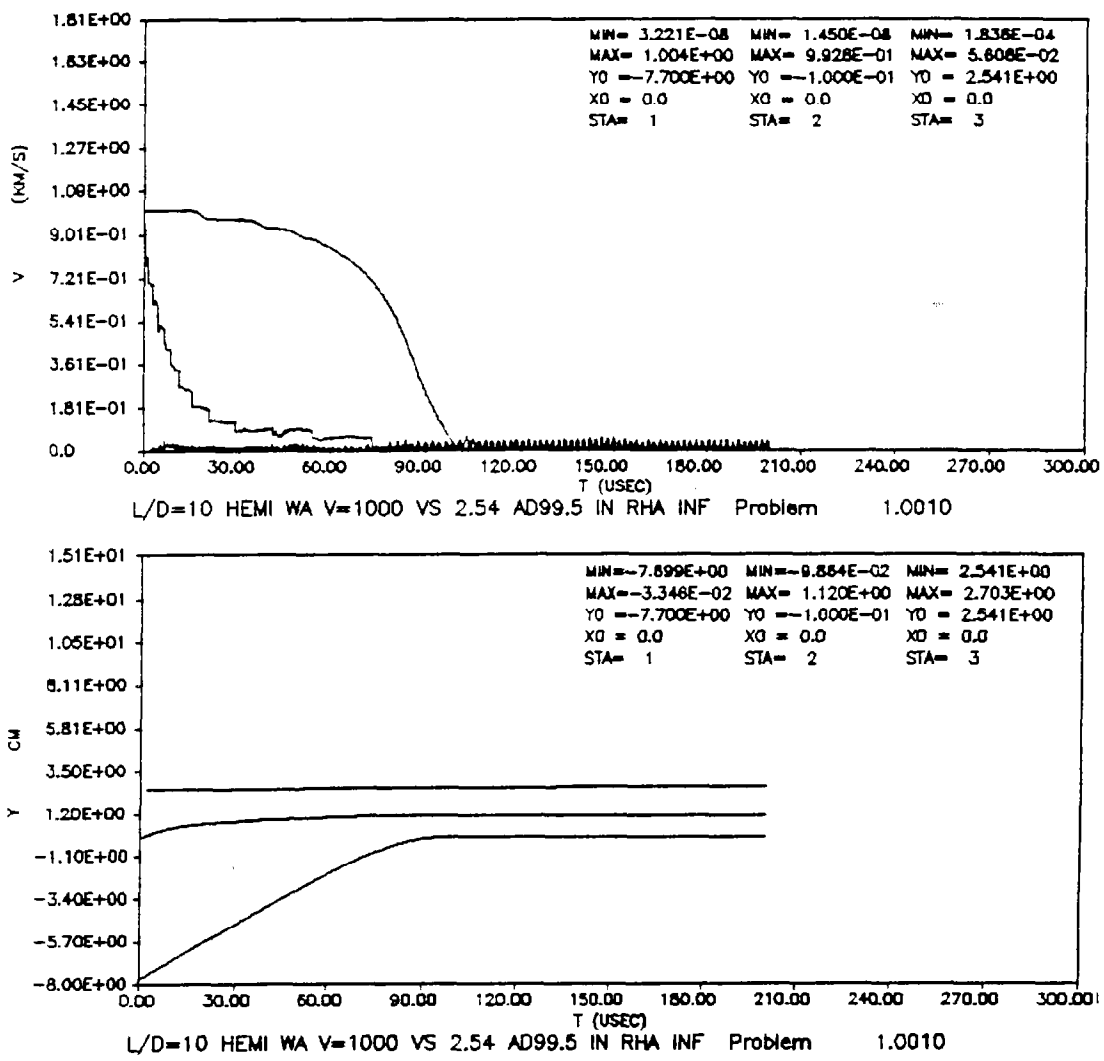


Figure 21.  $L/D=10$  WA rod at 1,000 m/s against 2.54-cm AD99.5 in  $\infty$  RHA: speed and position of rod nose and tail and tile back vs. time.

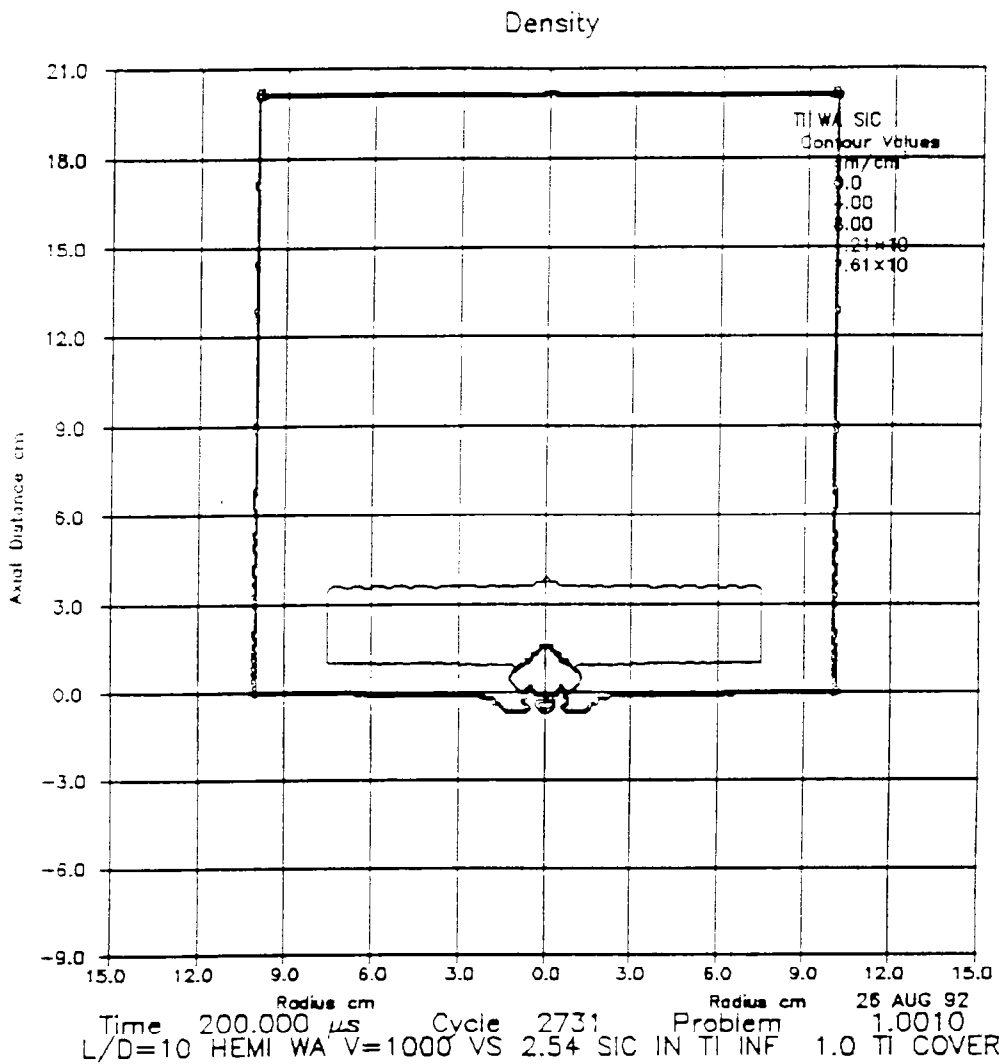


Figure 22. L/D=10 WA rod at 1,000 m/s against 2.54-cm SiC in  $\infty$  Ti covered by 1-cm Ti at 200  $\mu$ s.

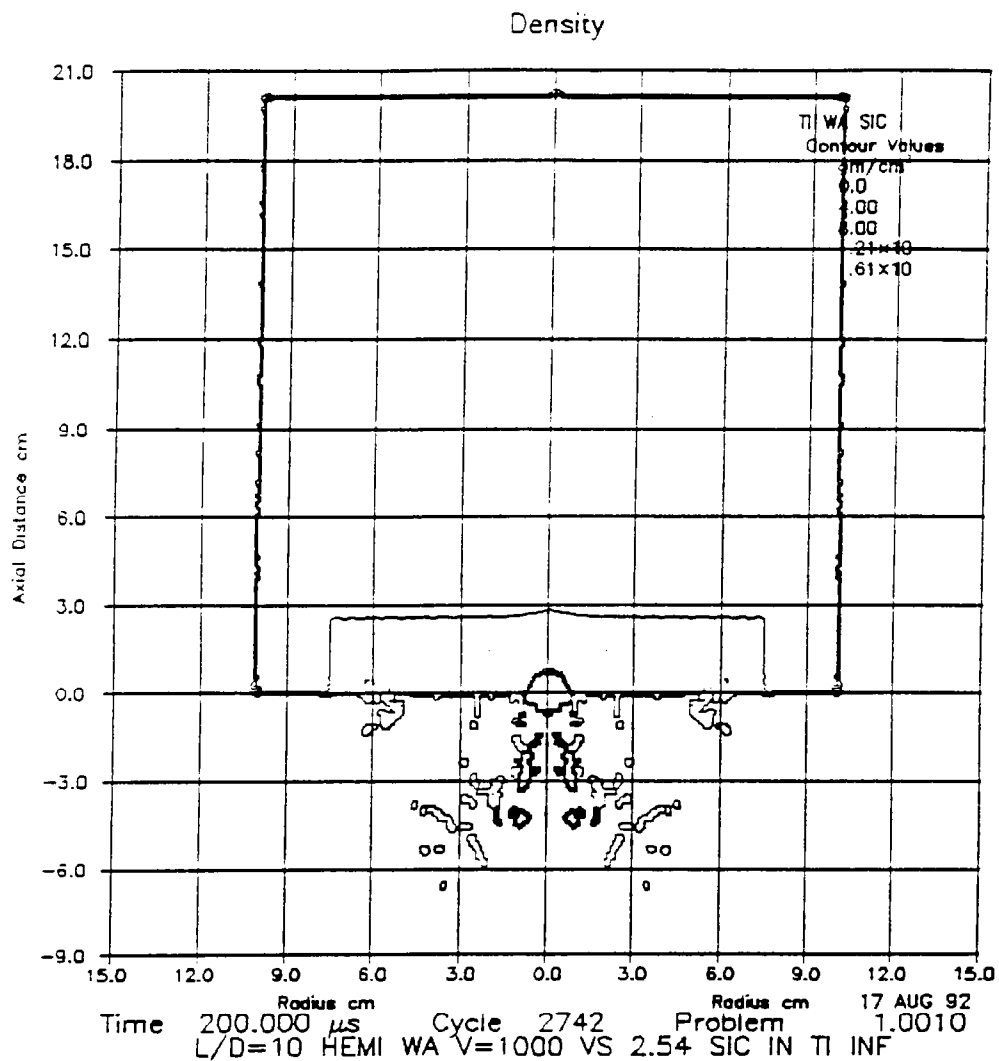


Figure 23. L/D=10 WA rod at 1,000 m/s against 2.54-cm SiC in  $\infty$  Ti at 200  $\mu$ s.

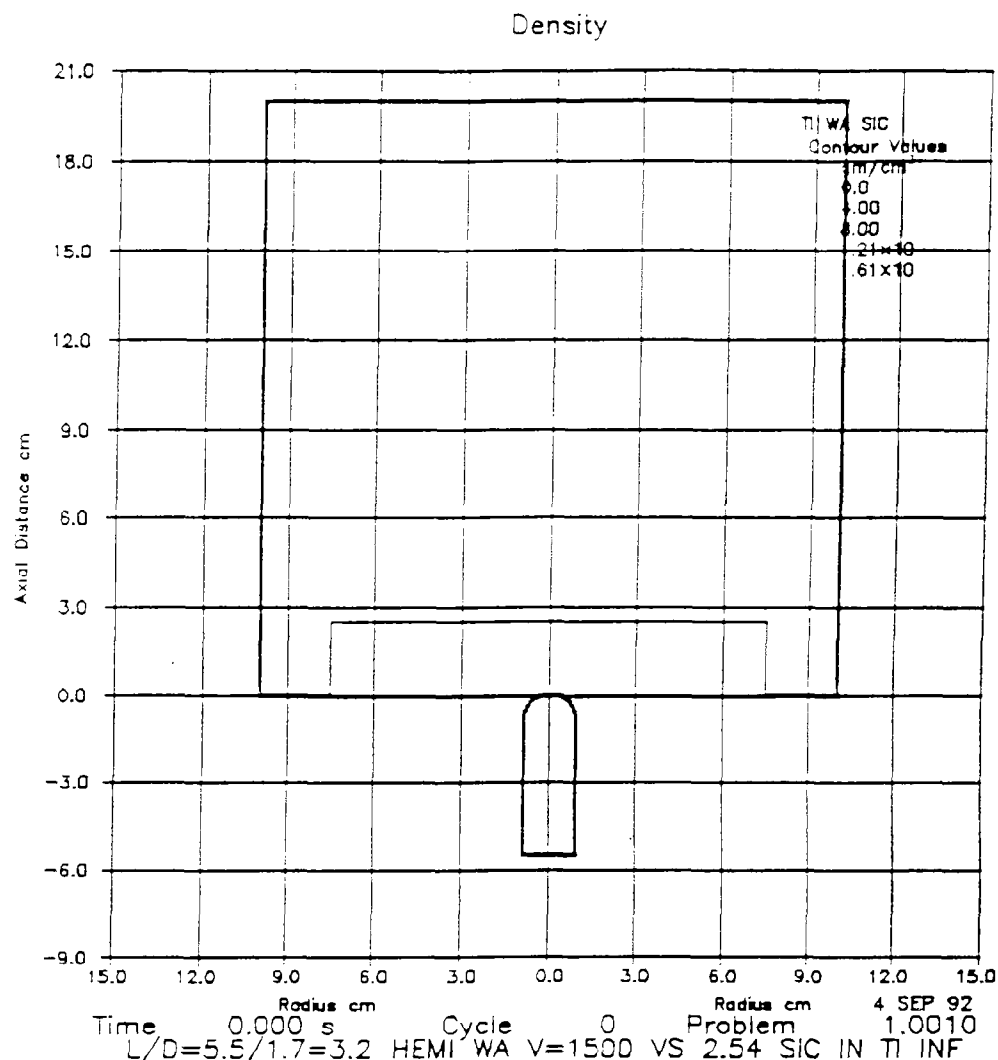


Figure 24. L/D=3.2 WA rod at 1,500 m/s against 2.54-cm SiC in  $\infty$  Ti at 0  $\mu$ s.

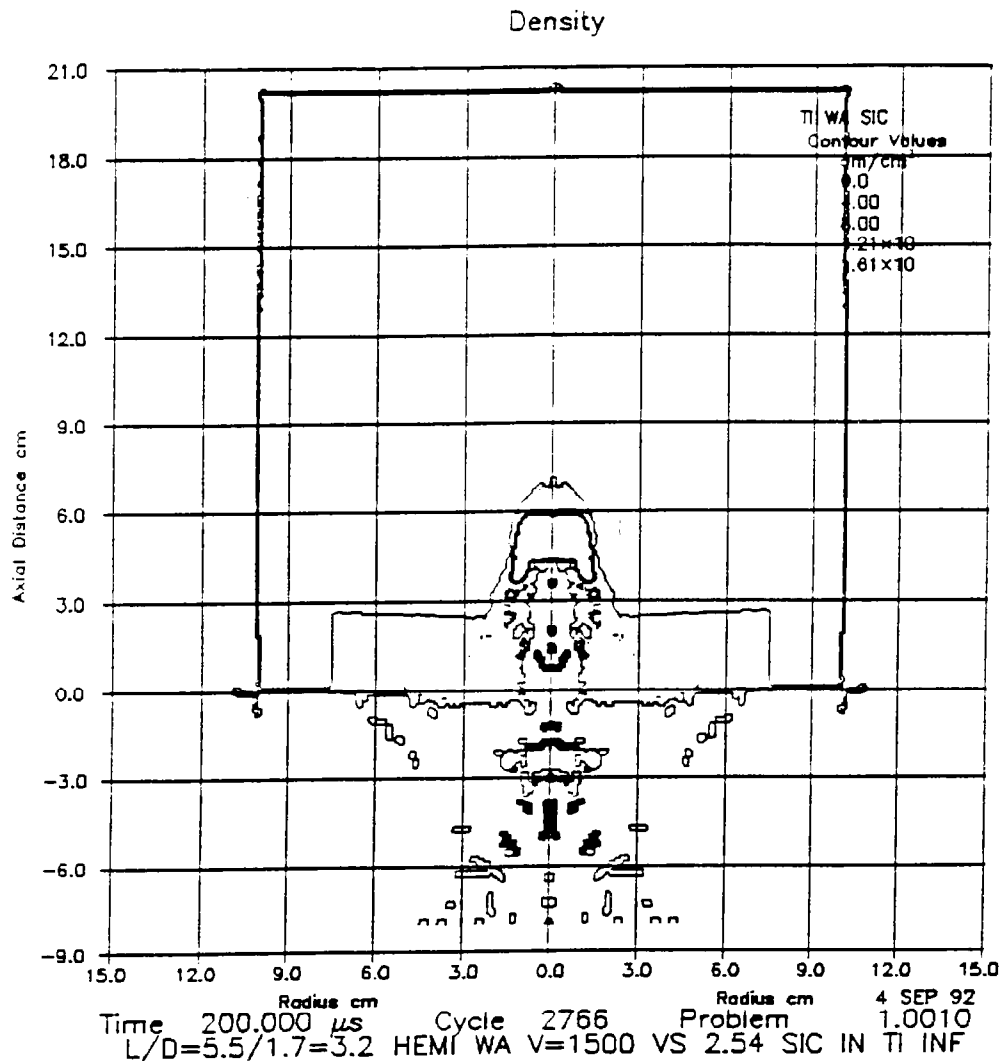


Figure 25. L/D=3.2 WA rod at 1,500 m/s against 2.54-cm SiC in  $\infty$  Ti at 200 s.

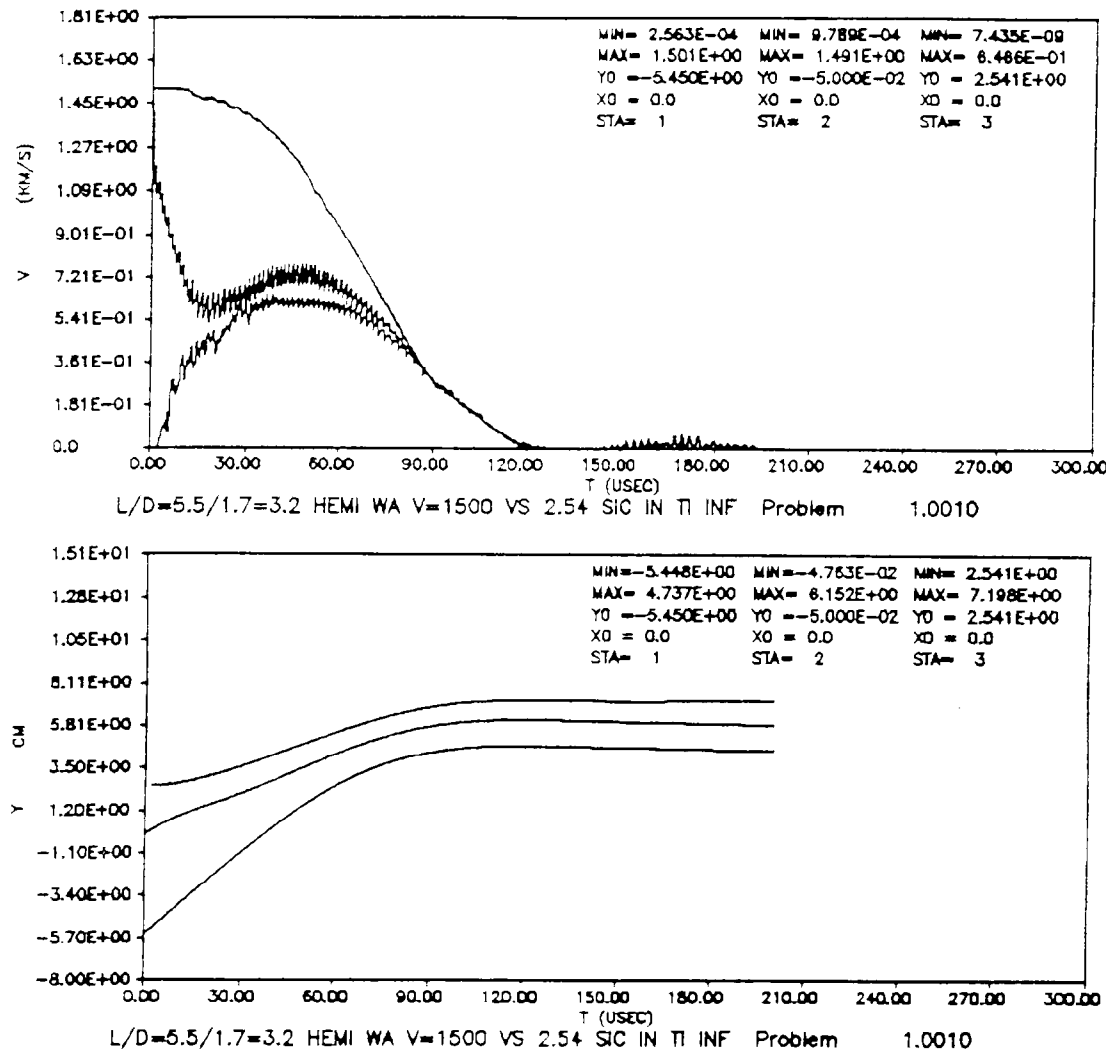


Figure 26.  $L/D=3.2$  WA rod at 1,500 m/s against 2.54-cm SiC in  $\infty$  Ti: speed and position of rod nose and tail and tile back vs. time.

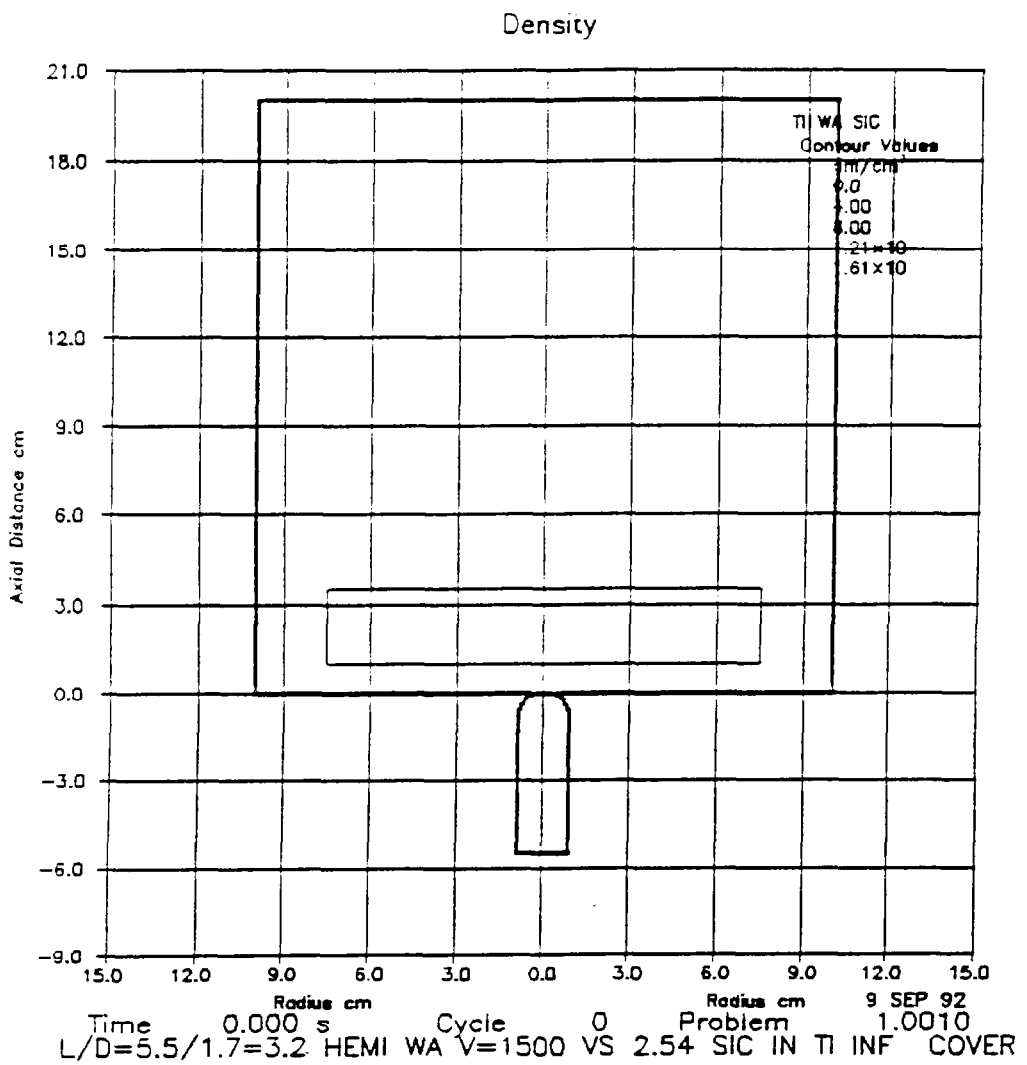


Figure 27. L/D=3.2 WA rod at 1,500 m/s against 2.54-cm SiC in  $\infty$  Ti covered by 1-cm Ti at 0  $\mu$ s.

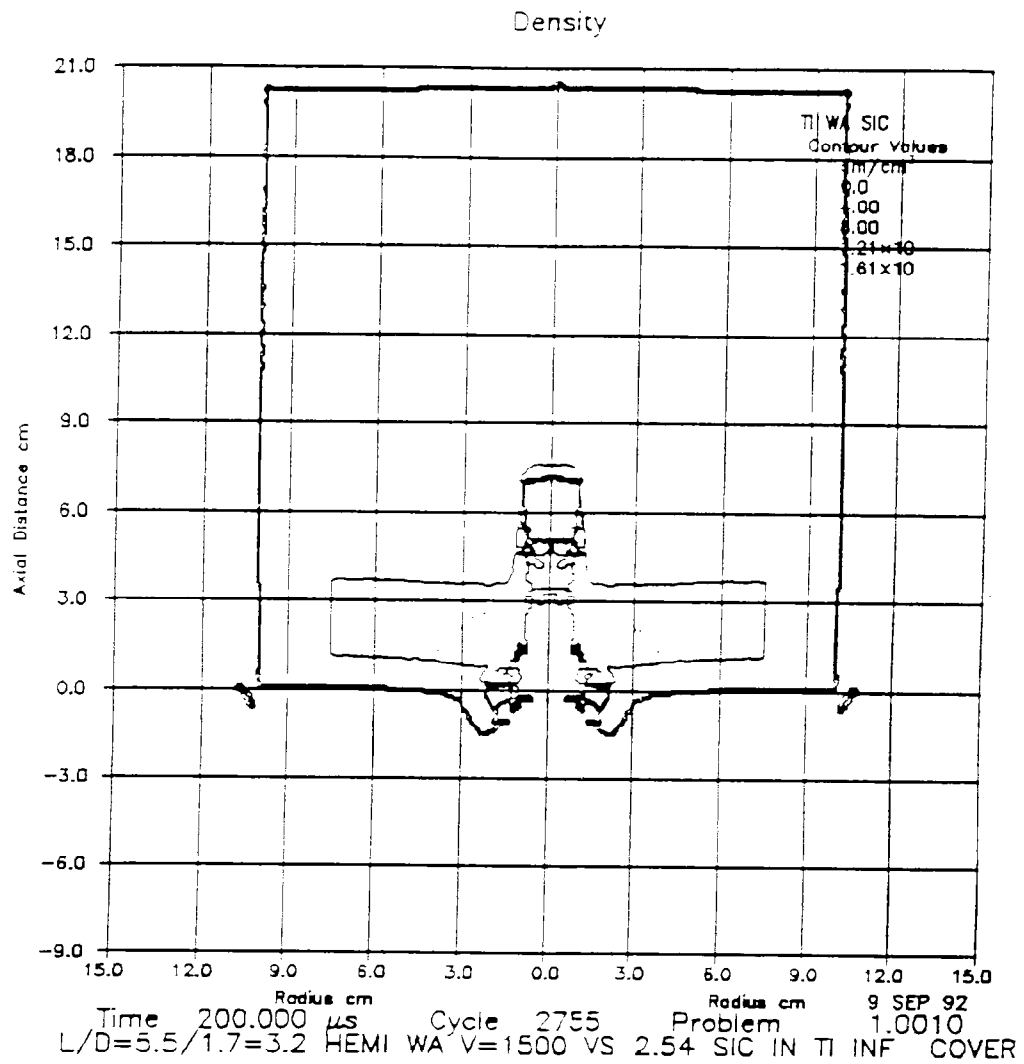


Figure 28. L/D=3.2 WA rod at 1,500 m/s against 2.54-cm SiC in  $\infty$  Ti covered by 1-cm Ti at 200  $\mu$ s.

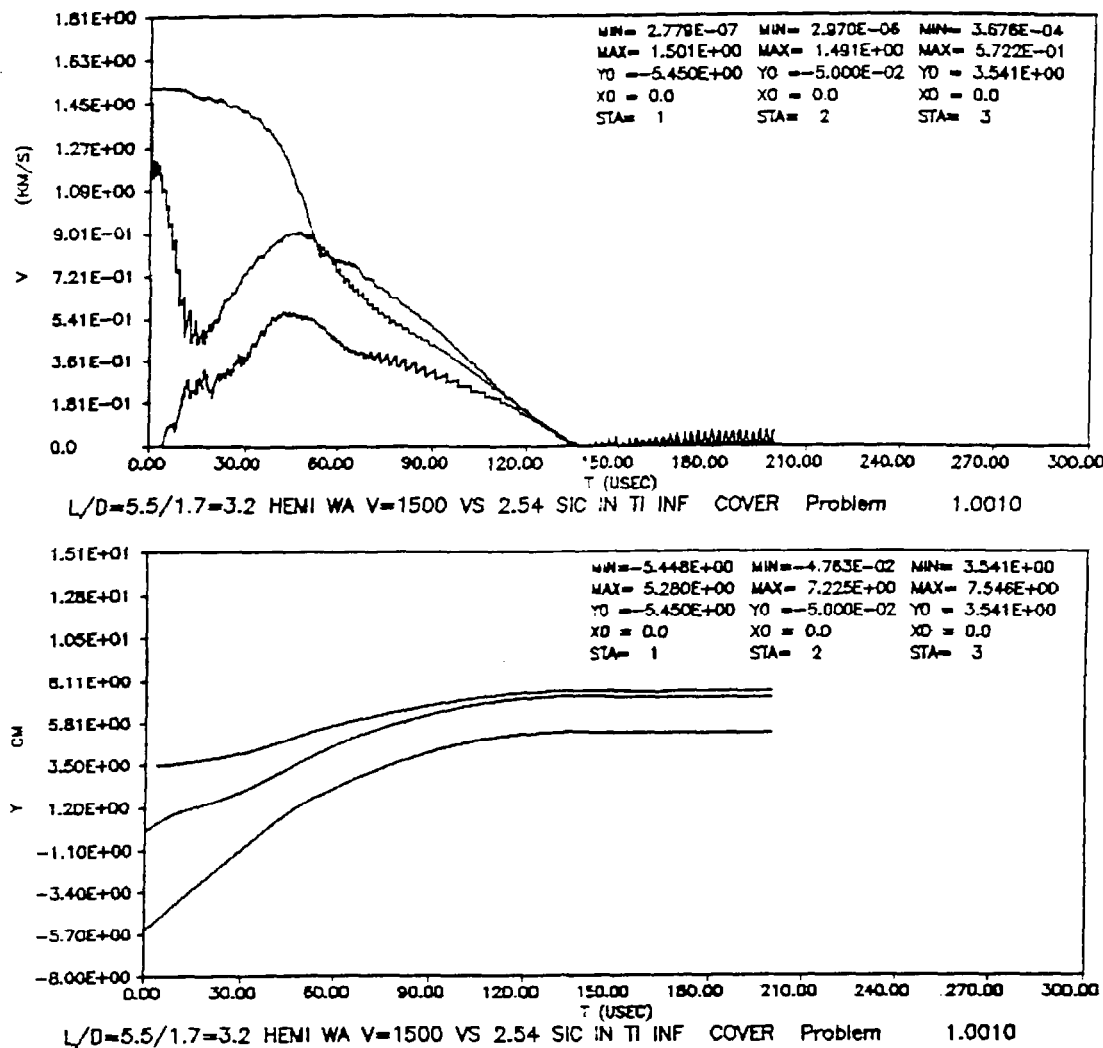


Figure 29.  $L/D=3.2$  WA rod at 1,500 m/s against 2.54-cm SiC in  $\infty$  Ti covered by 1-cm Ti; speed and position of rod nose and tail and tile back vs. time.

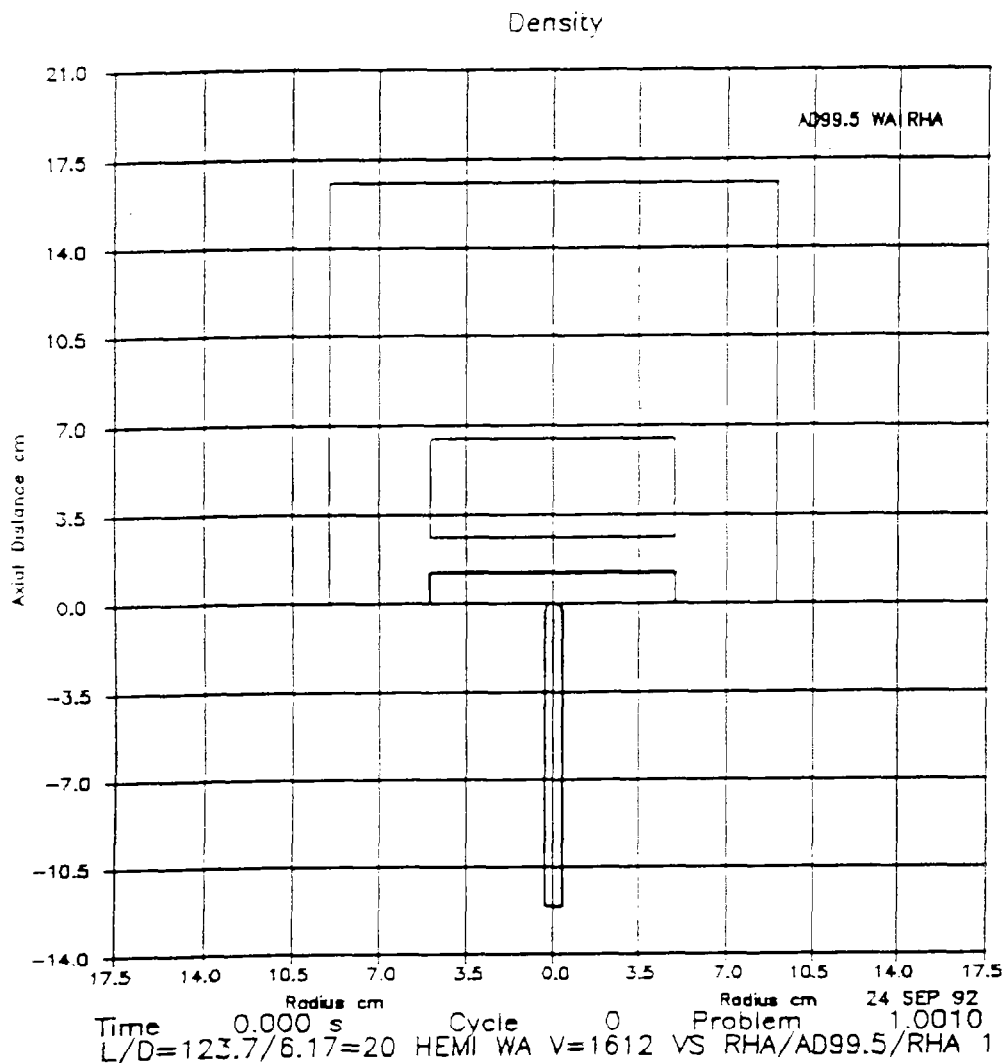


Figure 30. L/D=20 WA rod at 1,612 m/s against 4.00-cm AD99.5 in  $\infty$  RHA covered by 1.27-cm RHA at 0  $\mu$ s.

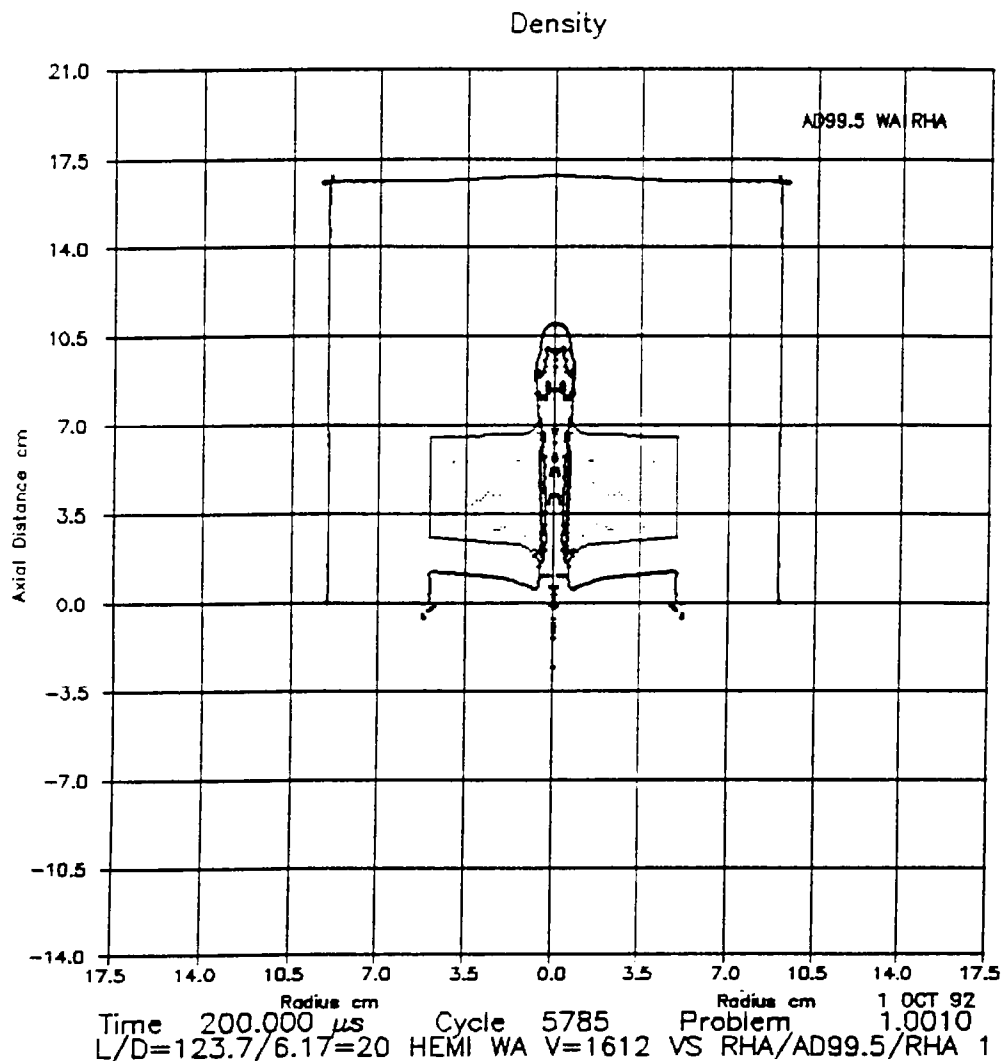


Figure 31. L/D=20 WA rod at 1,612 m/s against 4.00-cm AD99.5 in  $\infty$  RHA covered by 1.27-cm RHA at 200  $\mu$ s.

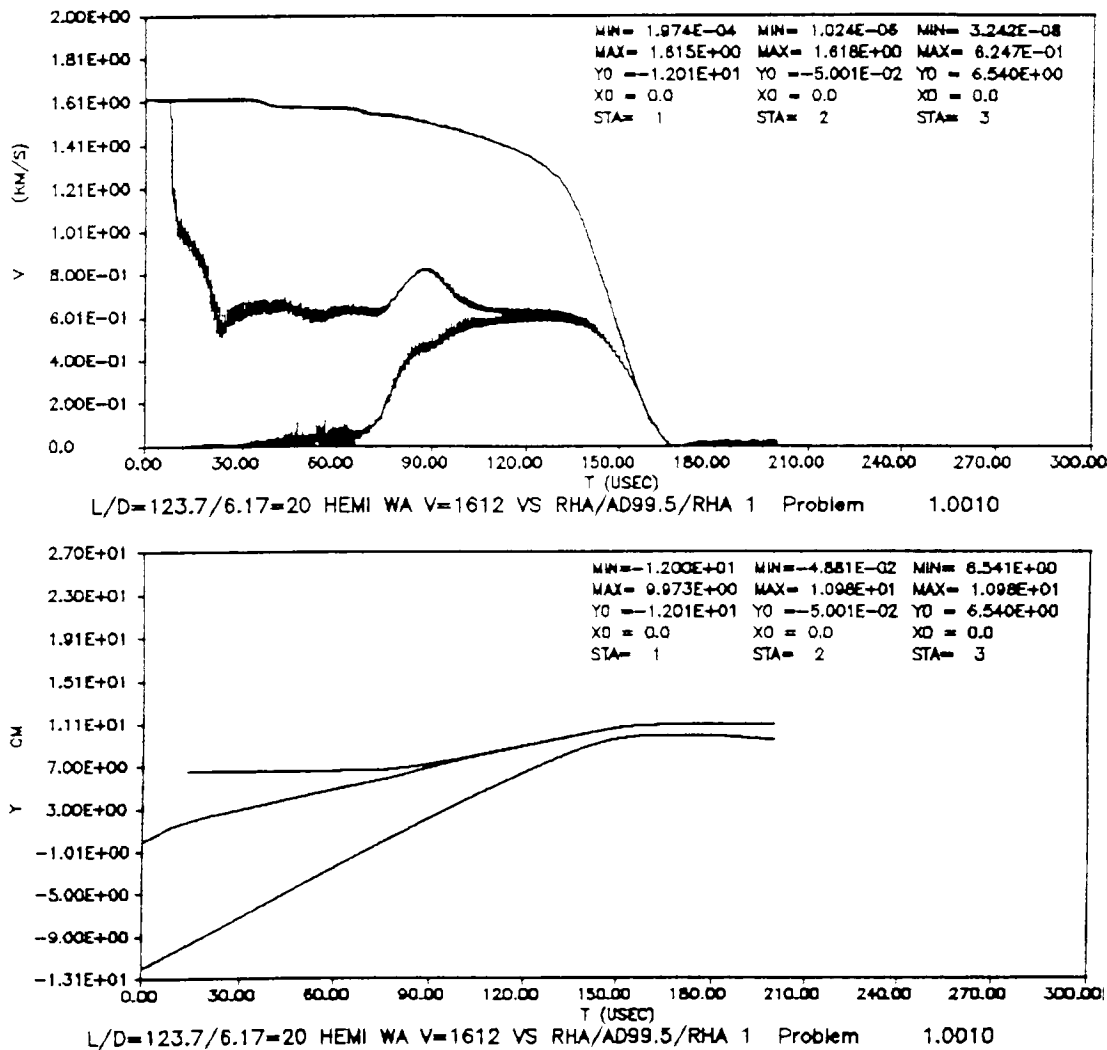


Figure 32.  $L/D=20$  WA rod at 1,612 m/s against 4.00-cm AD99.5 in  $\infty$  RHA covered by 1.27-cm RHA: speed and position of rod nose and tail and tile back vs. time.

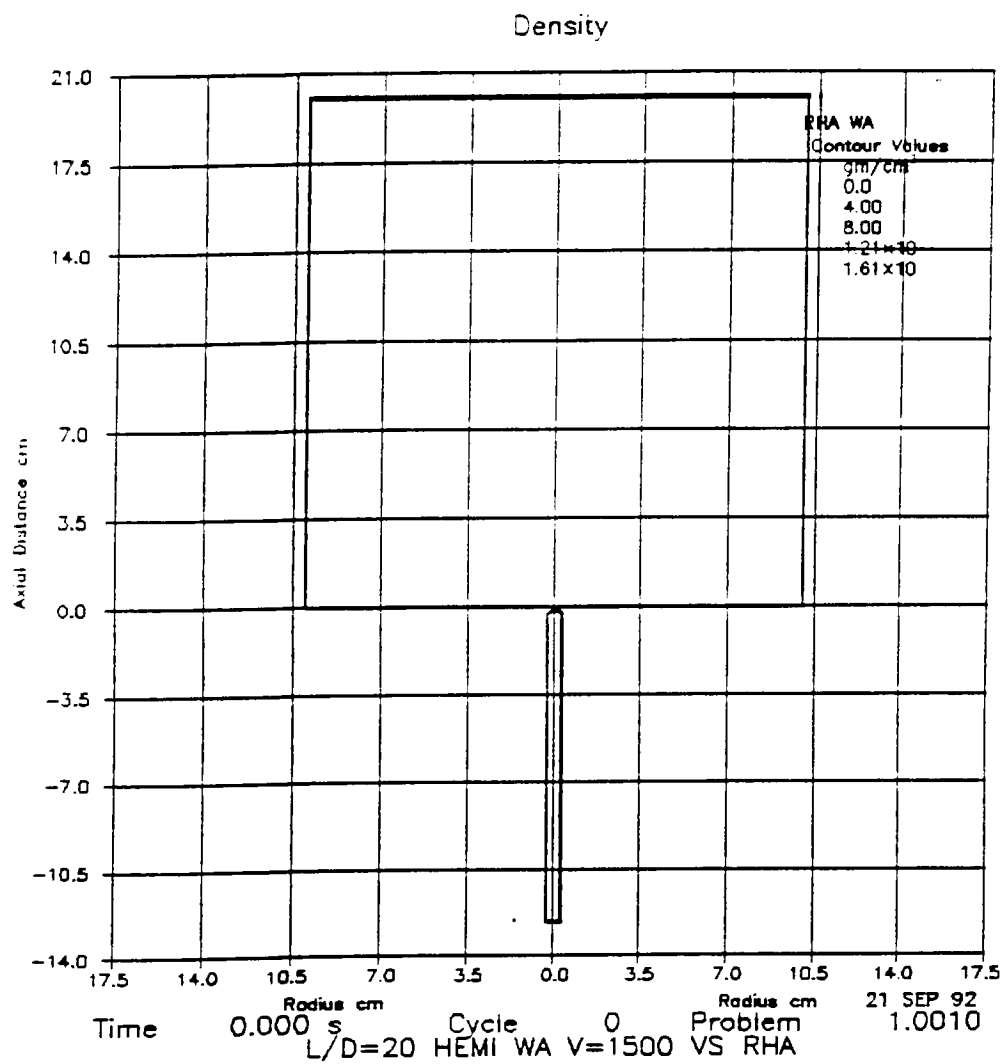


Figure 33. L/D=20 WA rod at 1,500 m/s against  $\infty$  RHA at 0 ps.

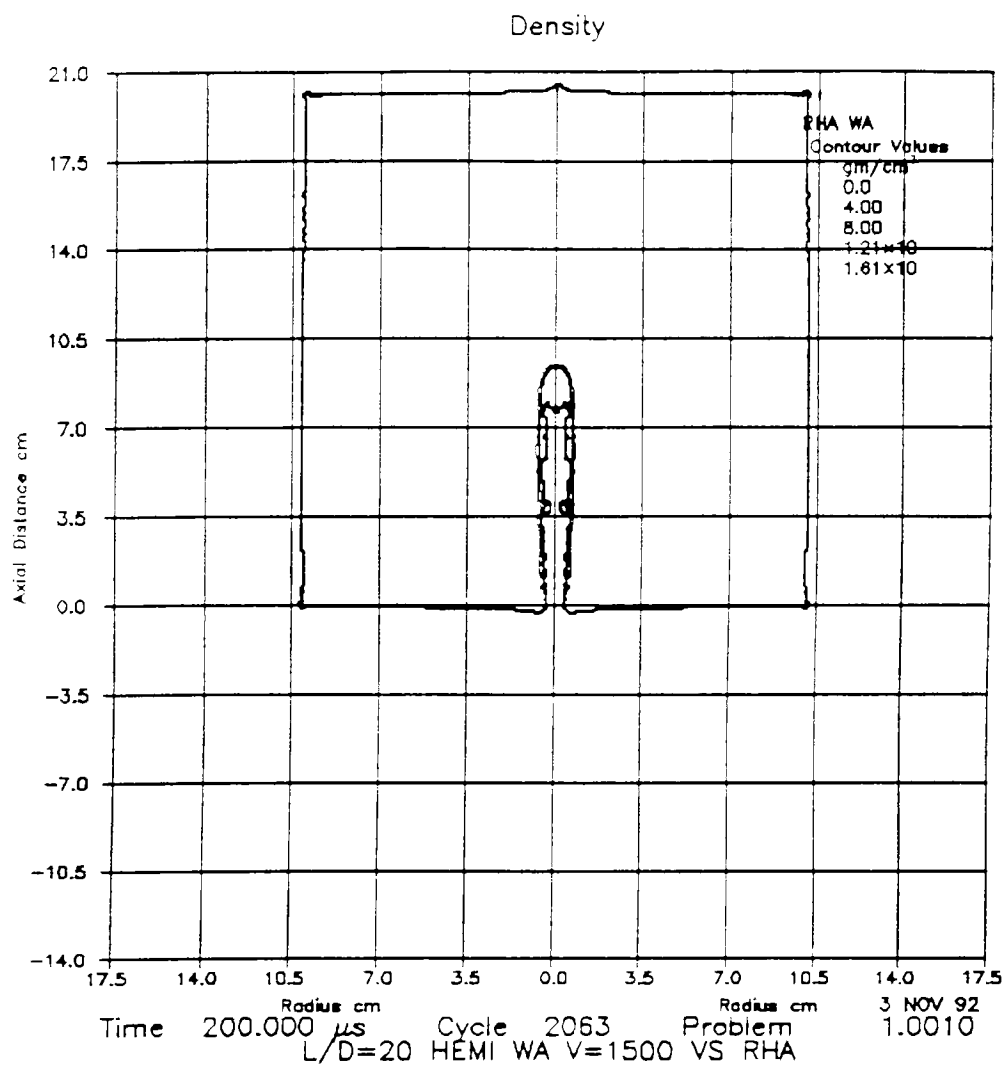


Figure 34. L/D=20 WA rod at 1,500 m/s against  $\infty$  RHA at 200  $\mu$ s.

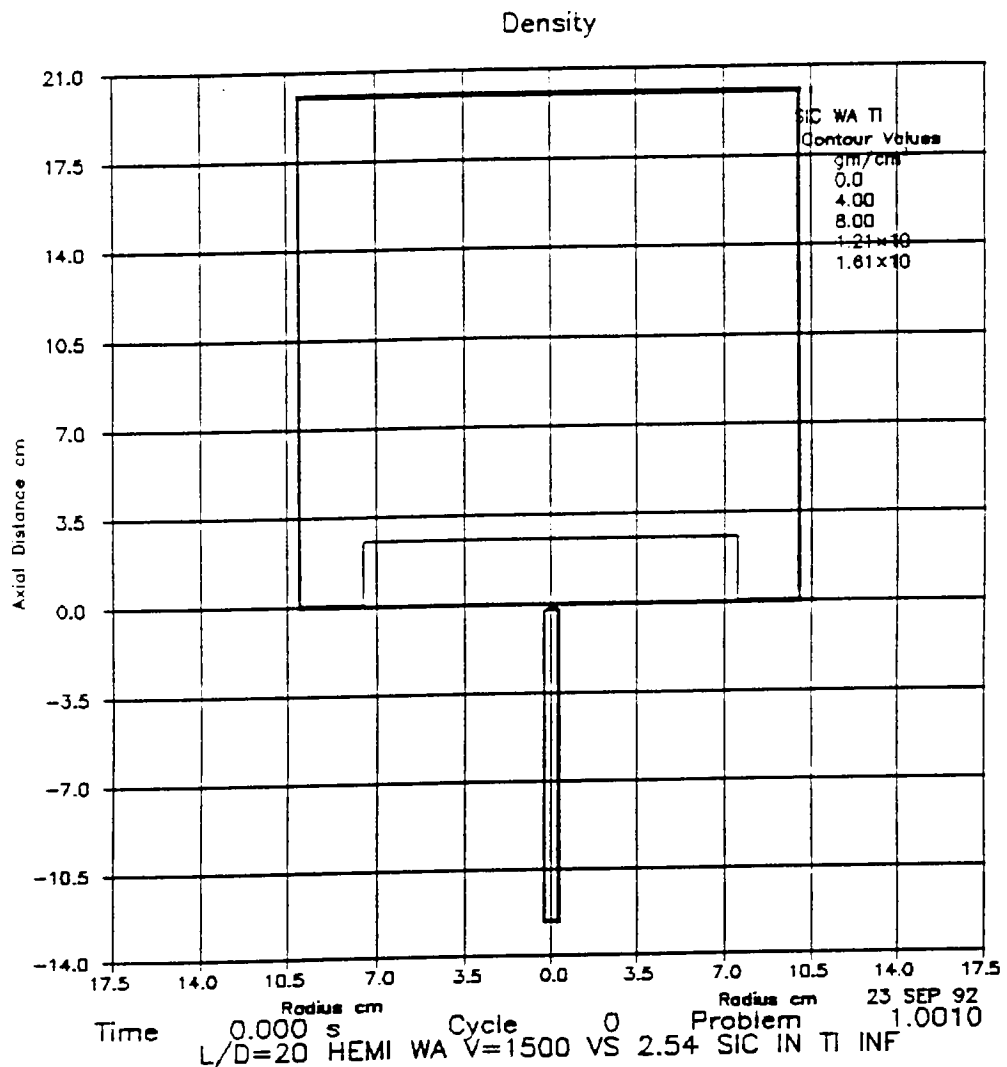


Figure 35.  $L/D=20$  WA rod at 1,500 m/s against 2.54-cm SiC in  $\infty$  Ti at 0  $\mu$ s.

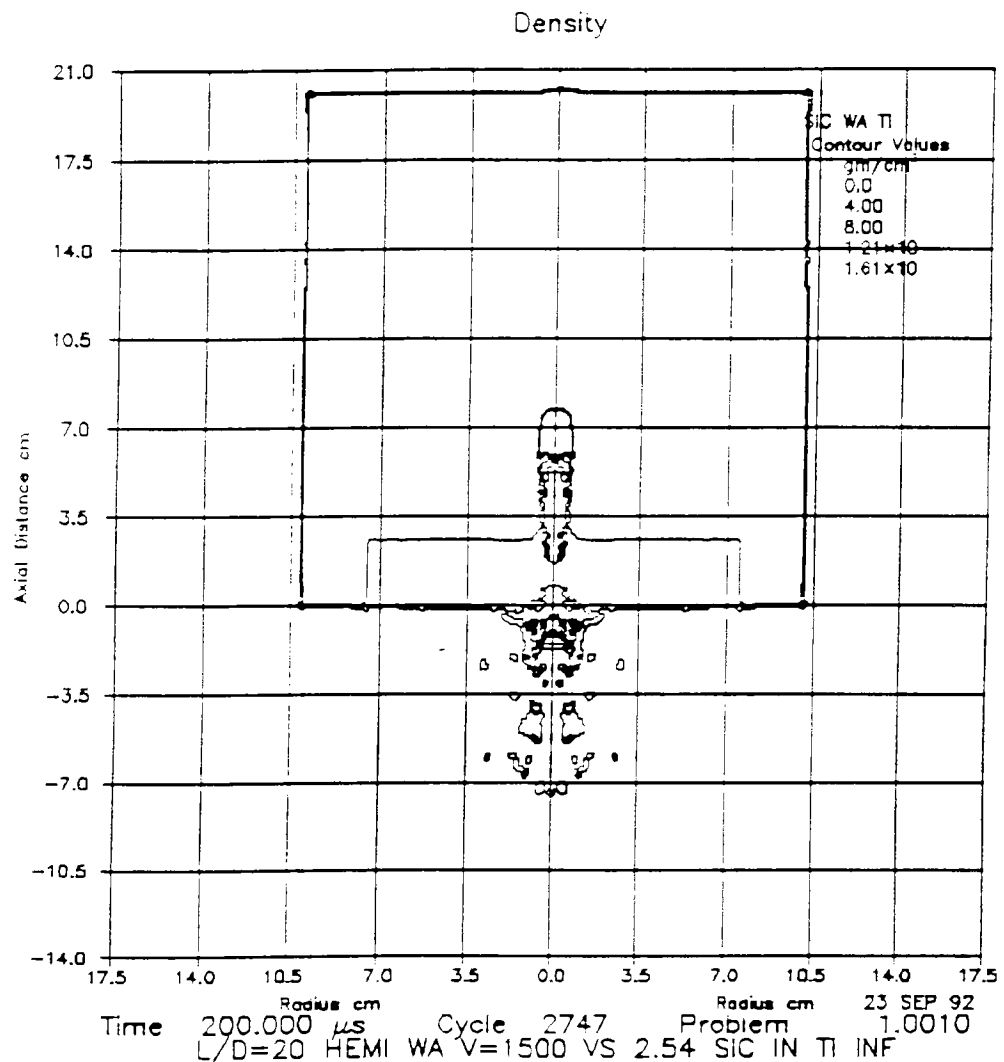


Figure 36. L/D=20 WA rod at 1,500 m/s against 2.54-cm SiC in  $\infty$  Ti at 200  $\mu$ s.

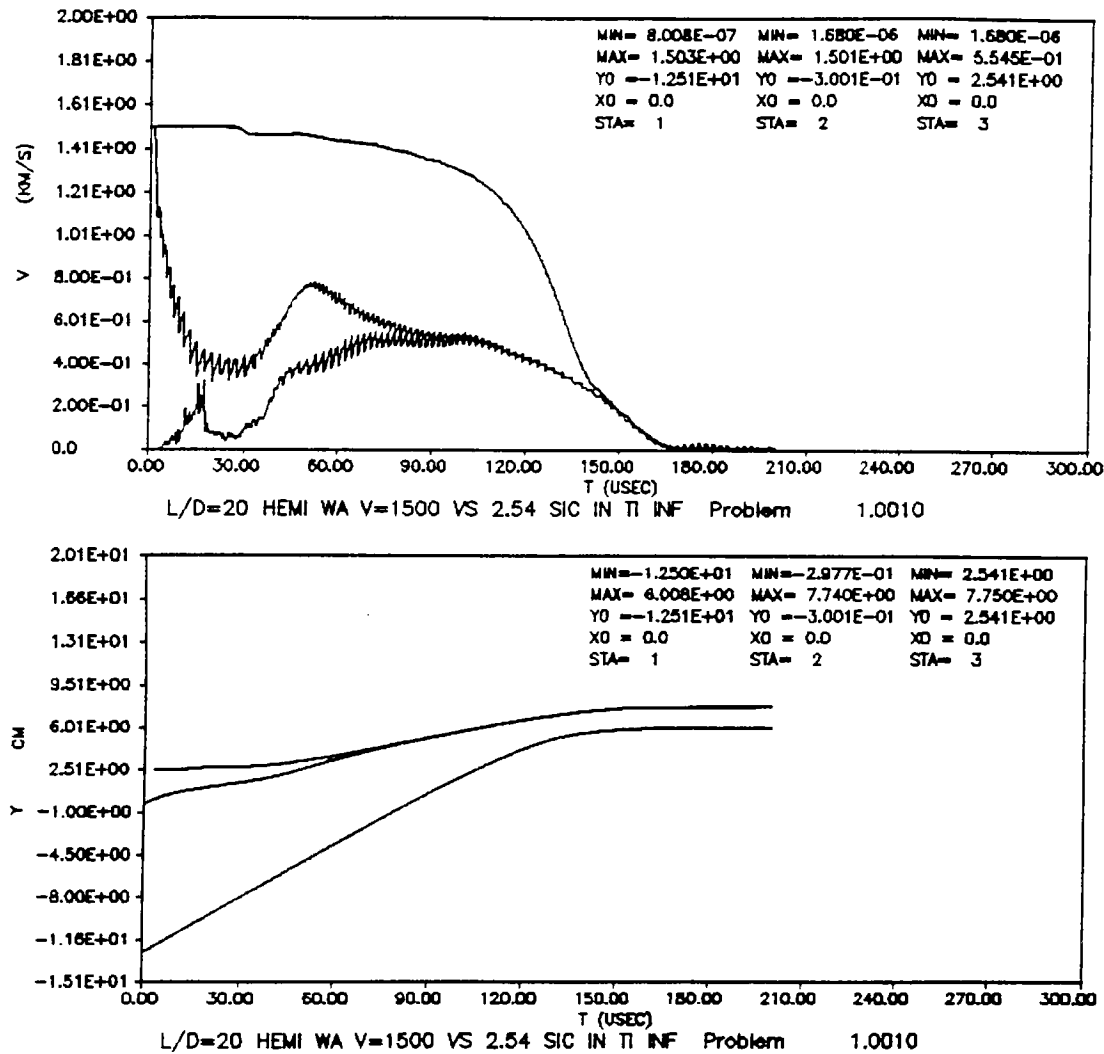


Figure 37.  $L/D=20$  WA rod at 1,500 m/s against 2.54-cm SiC in  $\infty$  Ti: speed and position of rod nose and tail and tile back vs. time.

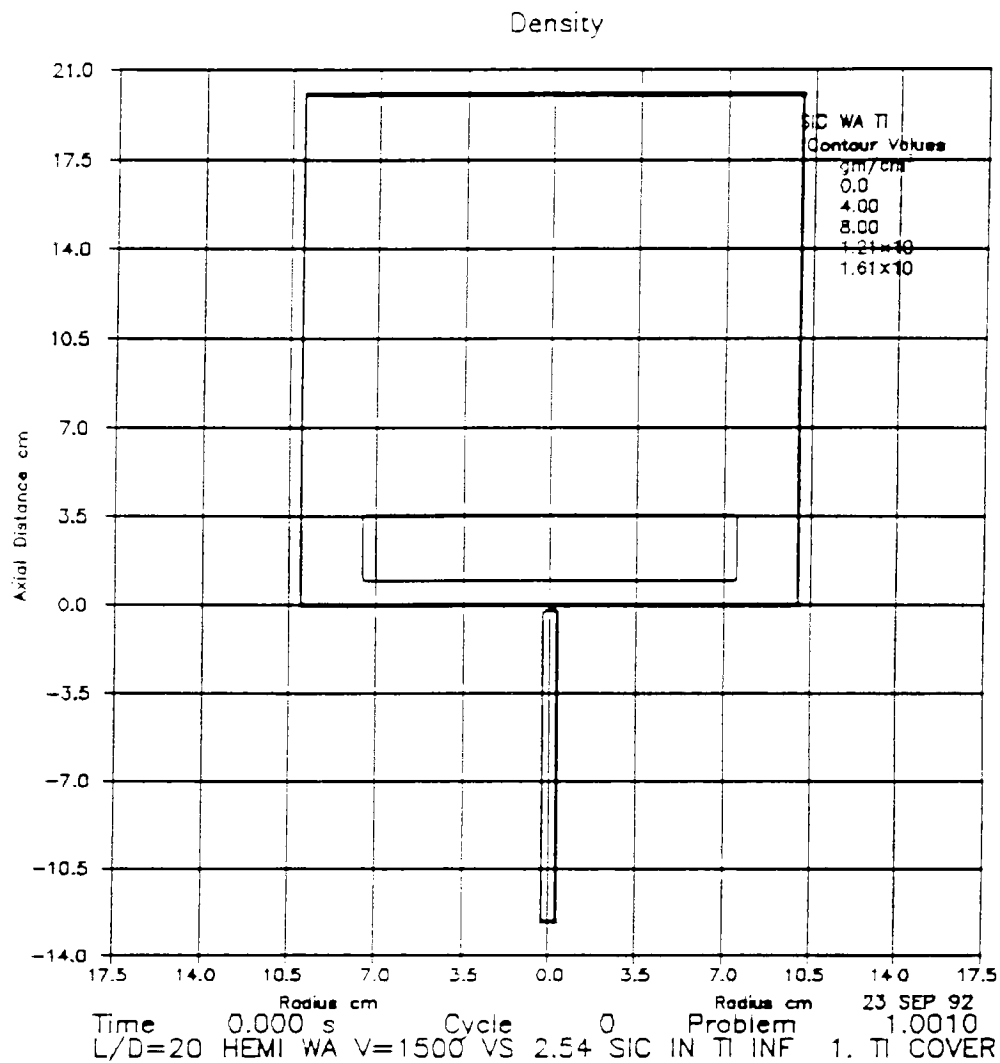


Figure 38. L/D=20 WA rod at 1,500 m/s against 2.54-cm SiC in  $\infty$  Ti covered by 1-cm Ti at 0  $\mu$ s.

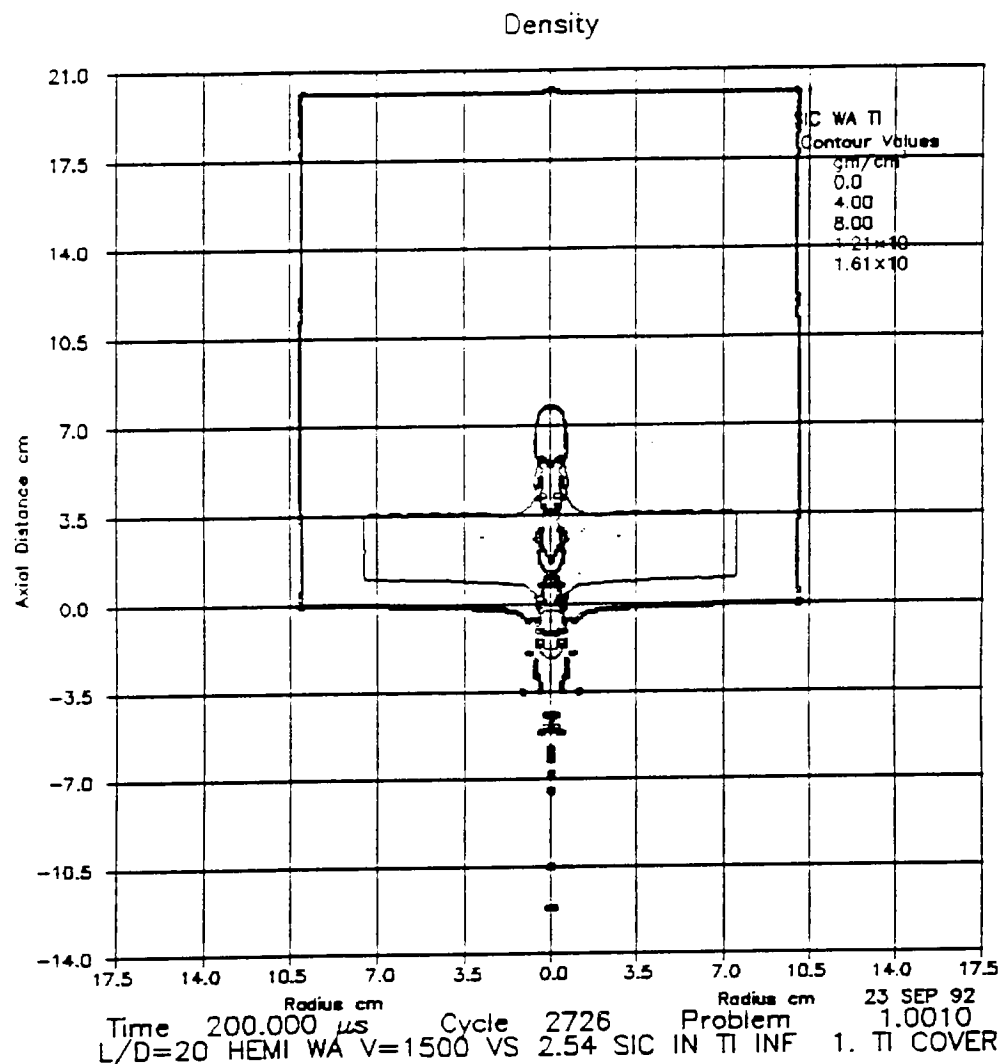


Figure 39. L/D=20 WA rod at 1,500 m/s against 2.54-cm SiC in  $\infty$  Ti covered by 1-cm Ti at 200  $\mu$ s.

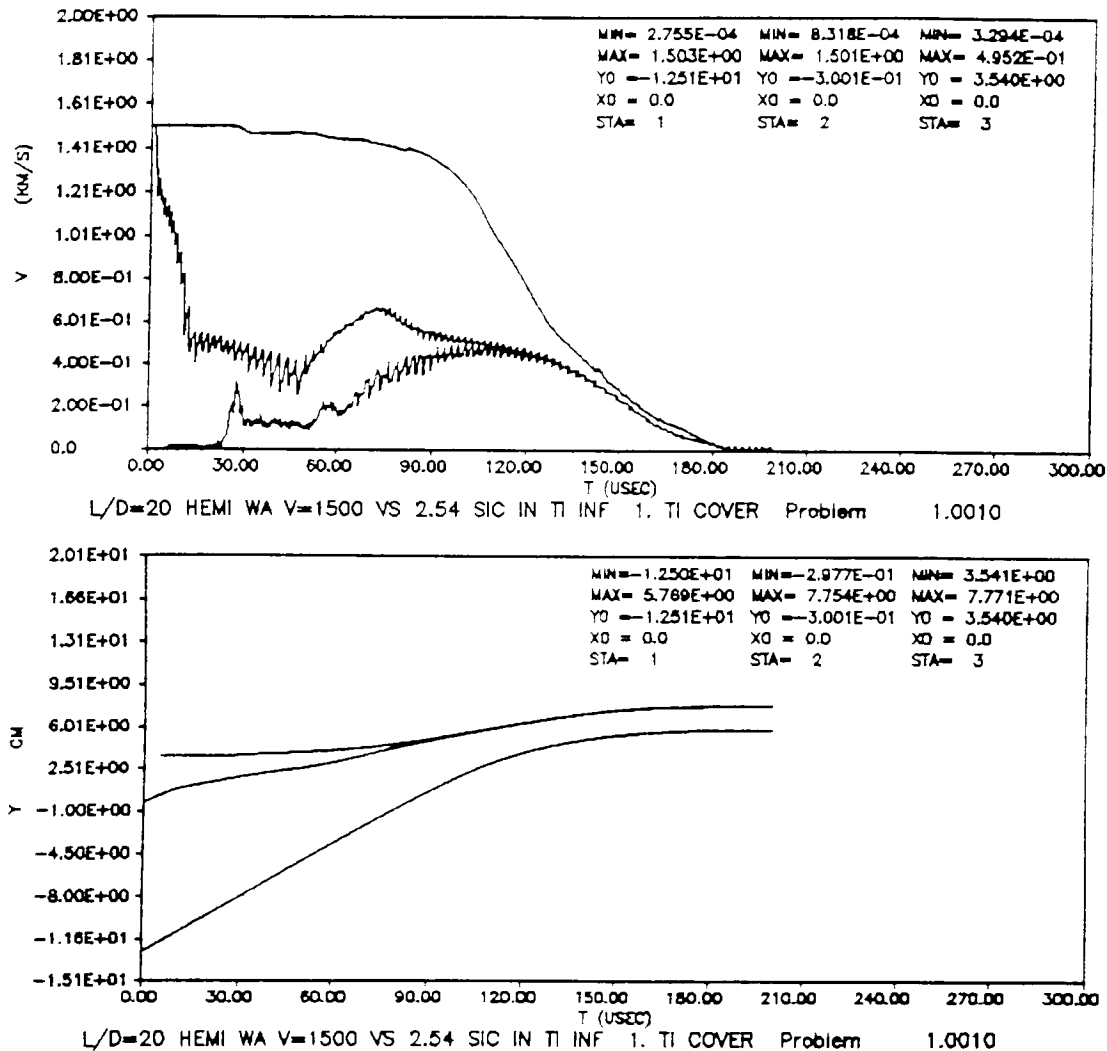


Figure 40. L/D=20 WA rod at 1,500 m/s against 2.54-cm SiC in  $\infty$  Ti covered by 1-cm Ti: speed and position of rod nose and tail and tile back vs. time.

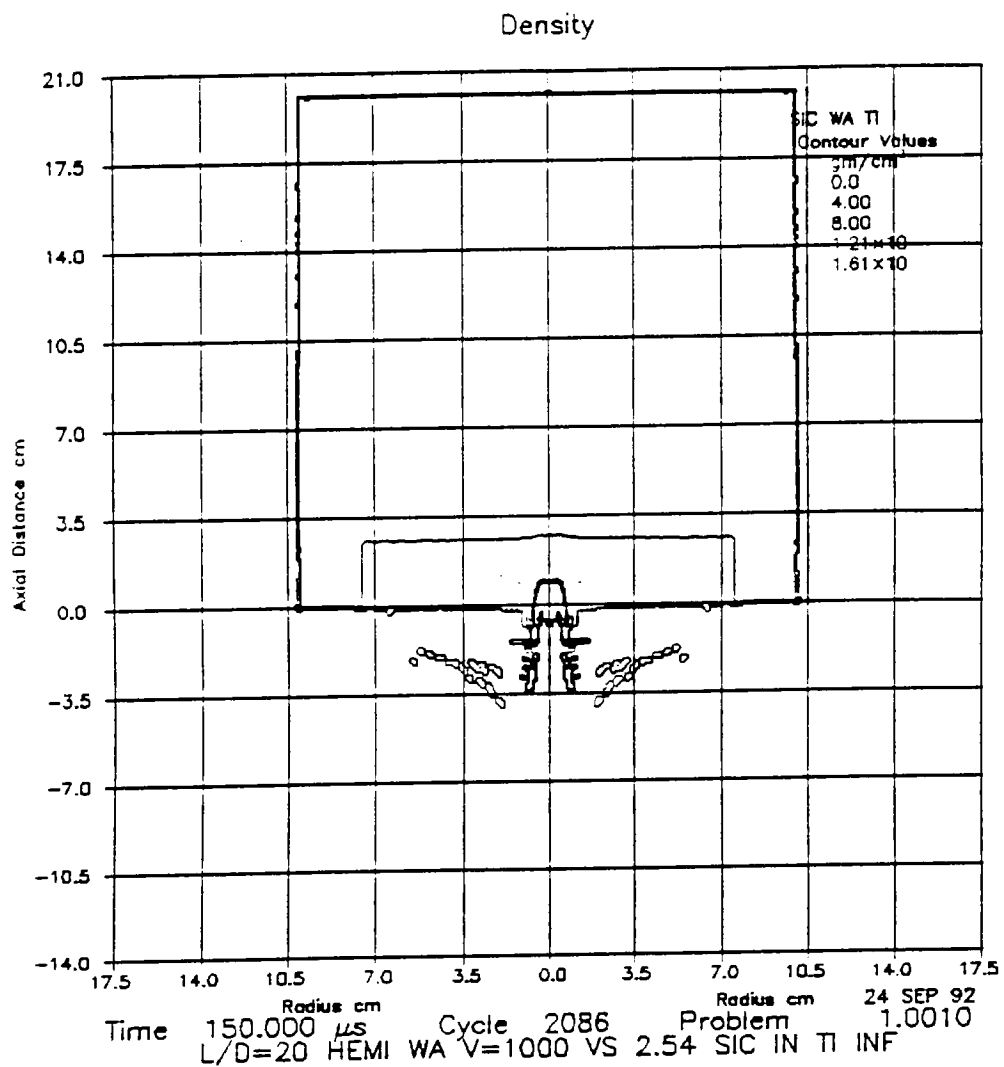


Figure 41. L/D=20 WA rod at 1,000 m/s against 2.54-cm SiC in  $\infty$  Ti at 150  $\mu$ s.

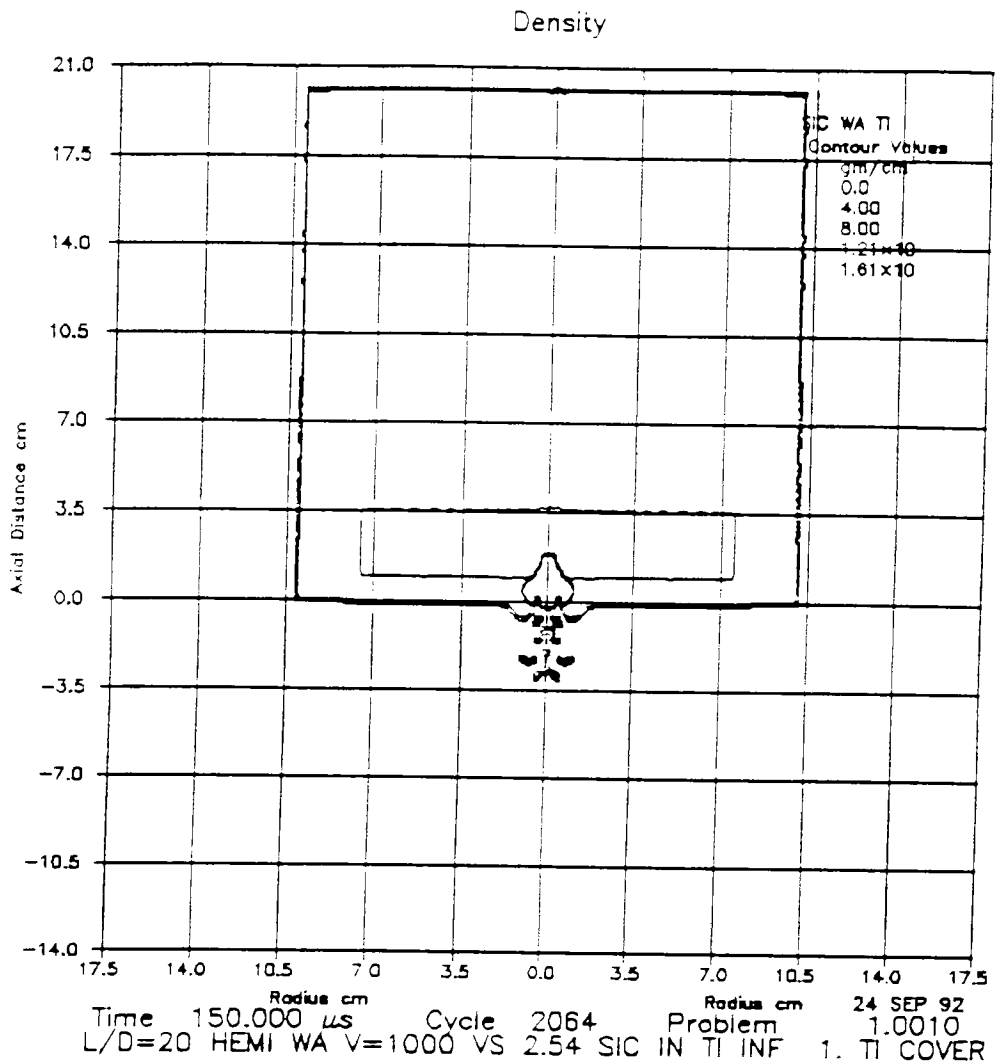


Figure 42. L/D=20 WA rod at 1,000 m/s against 2.54-cm SiC in  $\infty$  Ti covered by 1-cm Ti at 150  $\mu$ s.

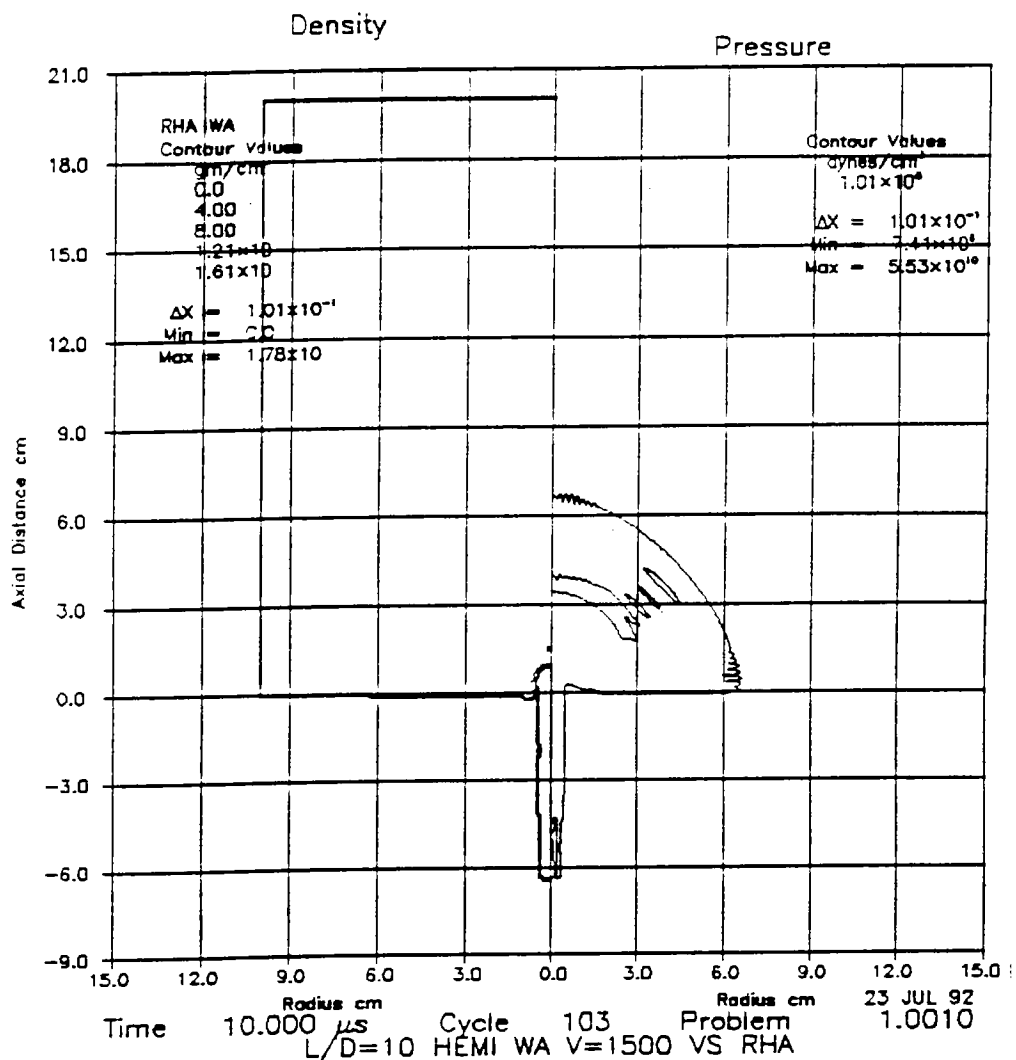


Figure 43. L/D=10 WA rod at 1,500 m/s against  $\infty$  RHA at 10  $\mu$ s:  $10^8$ -dynes/cm<sup>2</sup> pressure contours.

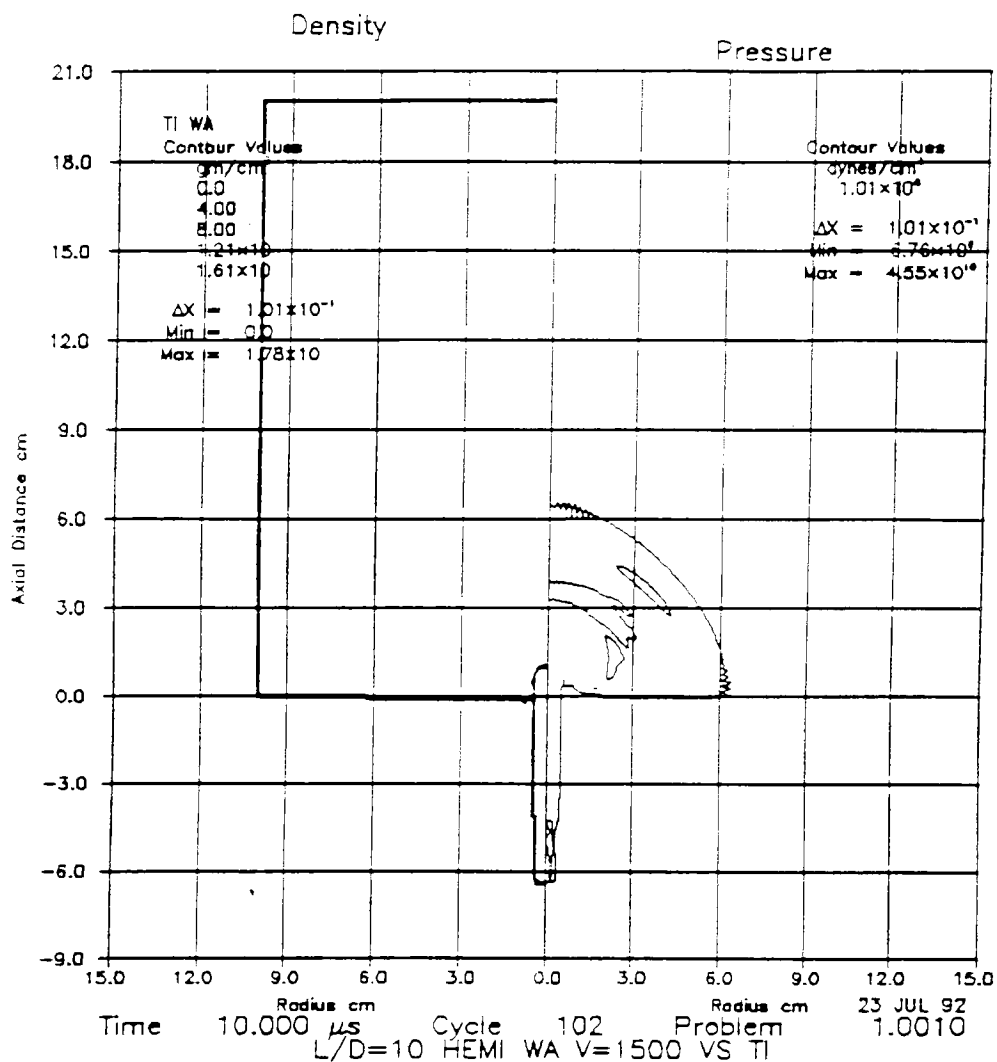


Figure 44. L/D=10 WA rod at 1,500 m/s against  $\infty$  Ti at 10  $\mu$ s:  $10^8$ -dynes/cm<sup>2</sup> pressure contours.

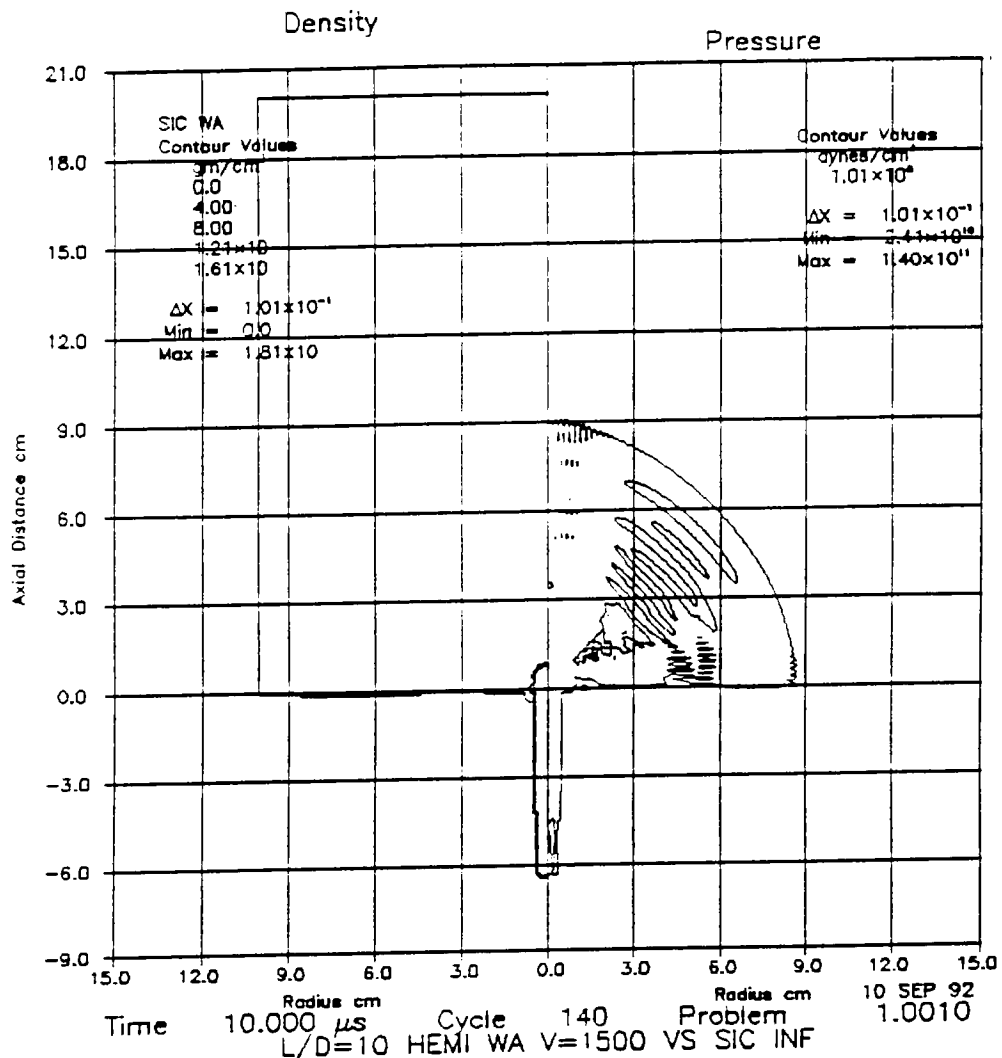


Figure 45. L/D=10 WA rod at 1,500 m/s against  $\infty$  SiC at 10  $\mu$ s:  $10^8$ -dynes/cm<sup>2</sup> pressure contours.

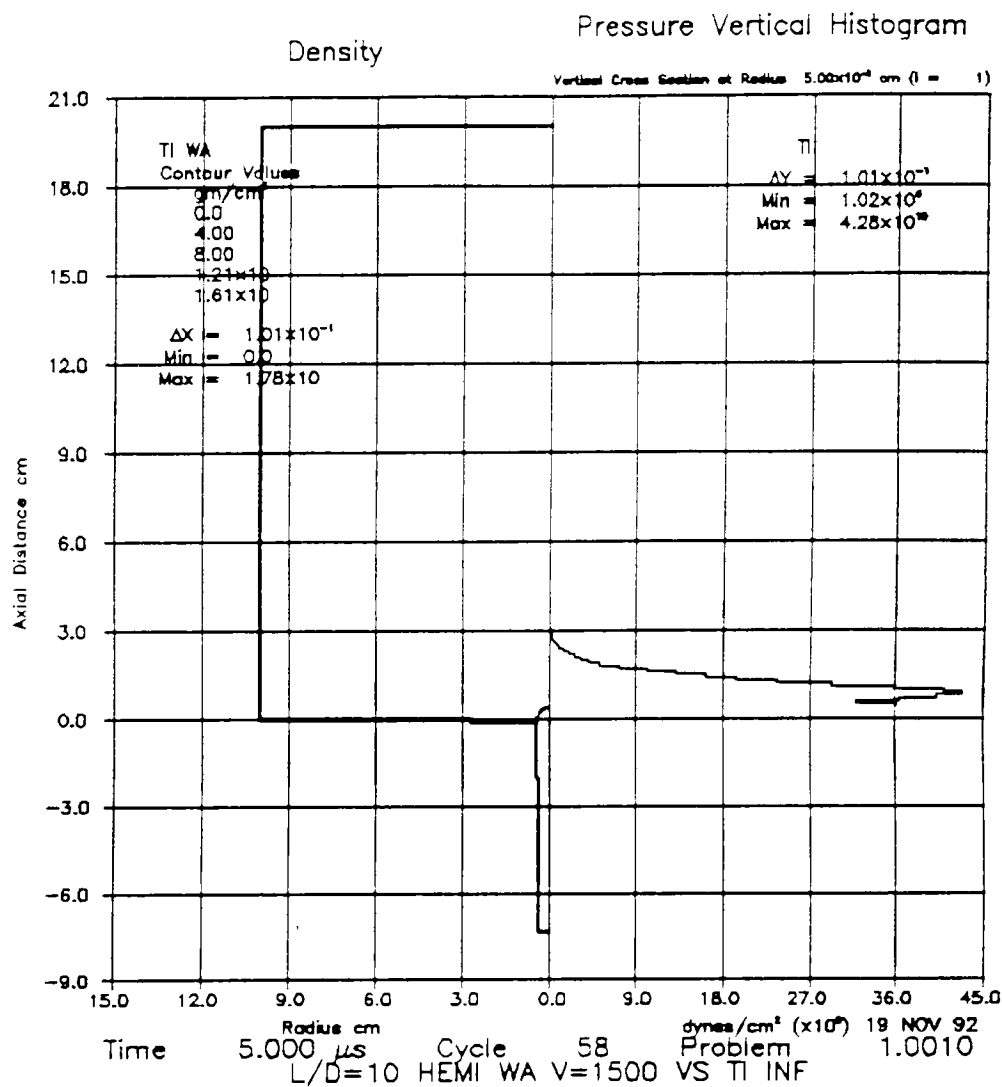


Figure 46. L/D=10 WA rod at 1,500 m/s against  $\infty$  Ti at 6  $\mu$ s: pressure vertical histogram on the shotline.

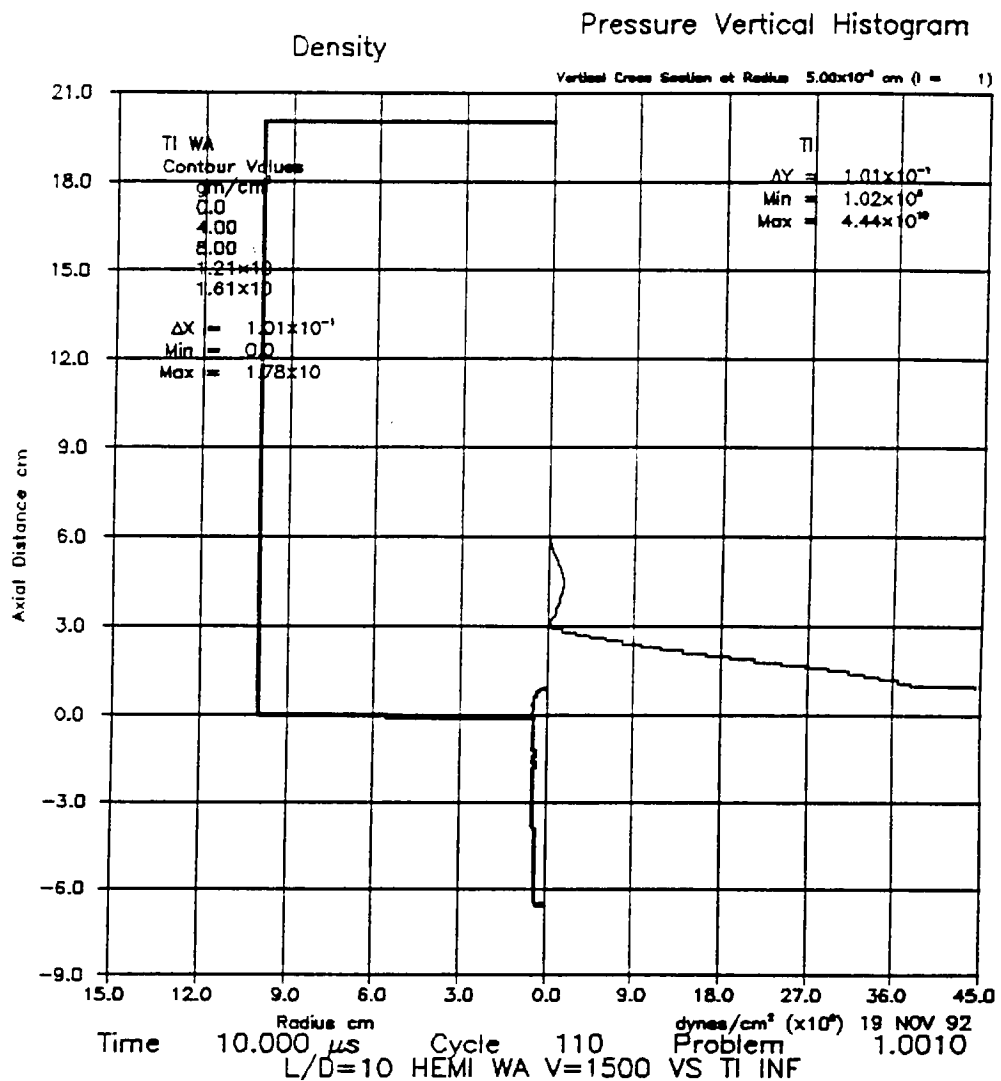


Figure 47. L/D=10 WA rod at 1,500 m/s against  $\infty$  Ti at 10  $\mu$ s: pressure vertical histogram on the shotline.

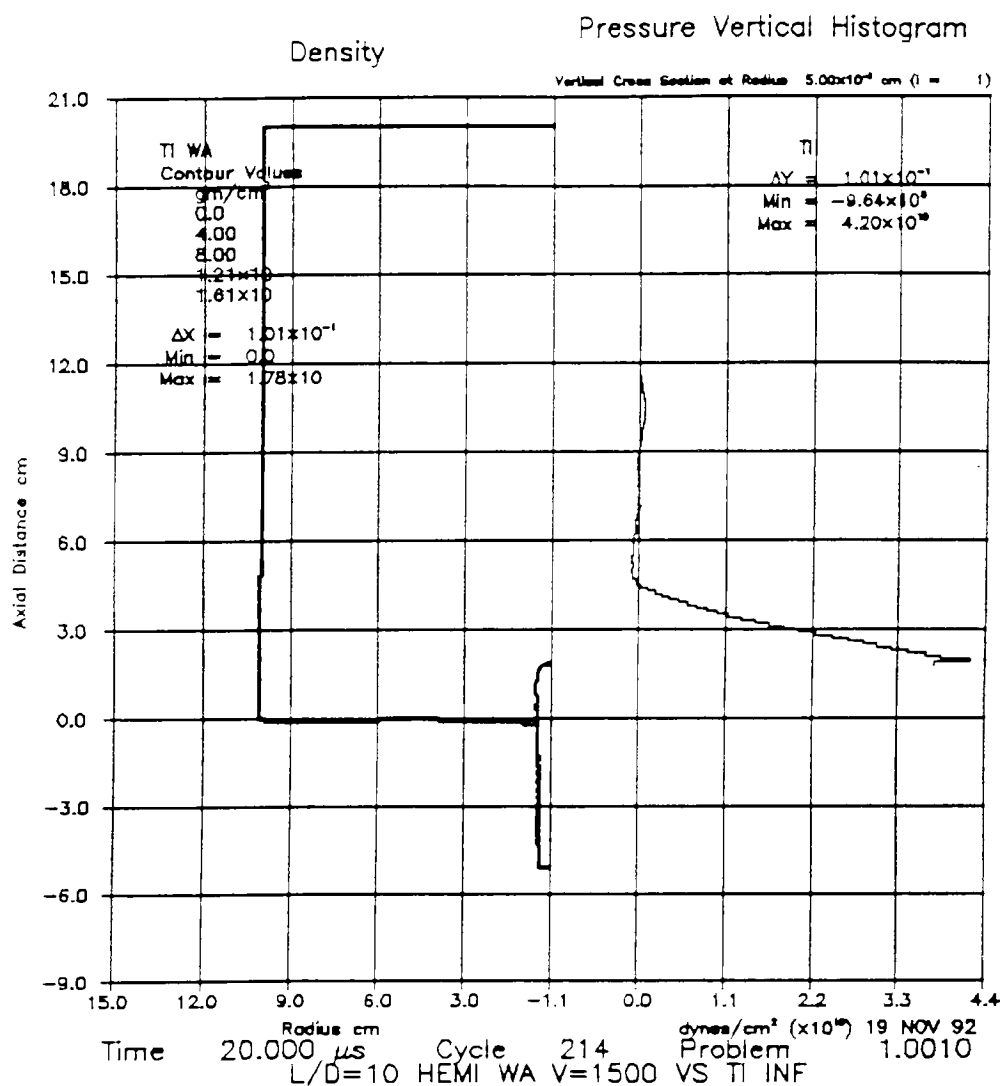


Figure 48. L/D=10 WA rod at 1,500 m/s against  $\infty$  Ti at 20  $\mu\text{s}$ : pressure vertical histogram on the shotline.

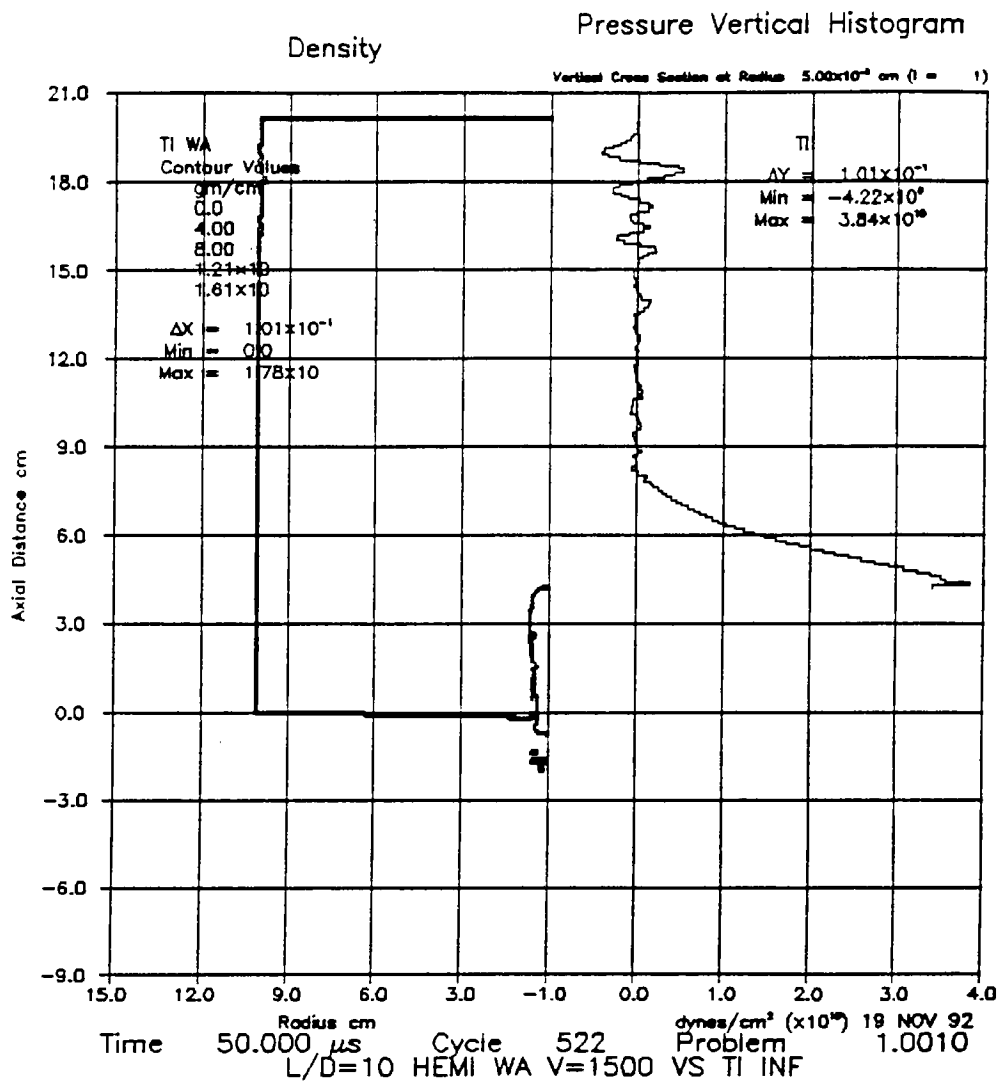


Figure 49. L/D=10 WA rod at 1,500 m/s against  $\infty$  Ti at 50  $\mu\text{s}$ : pressure vertical histogram on the shotline.

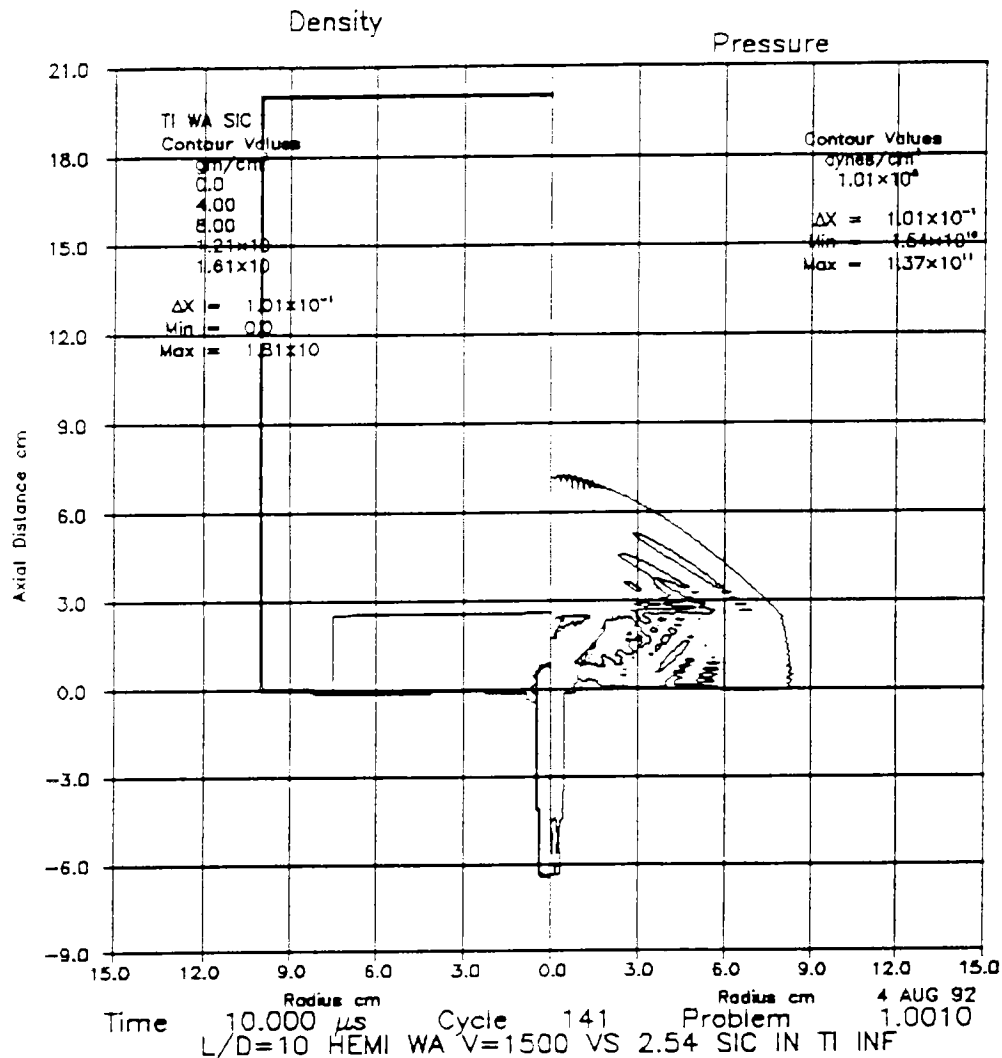


Figure 50. L/D=10 WA rod at 1,500 m/s against 2.54-cm SiC in  $\infty$  Ti at 10  $\mu$ s:  $10^8$ -dynes/cm $^2$  pressure contours.

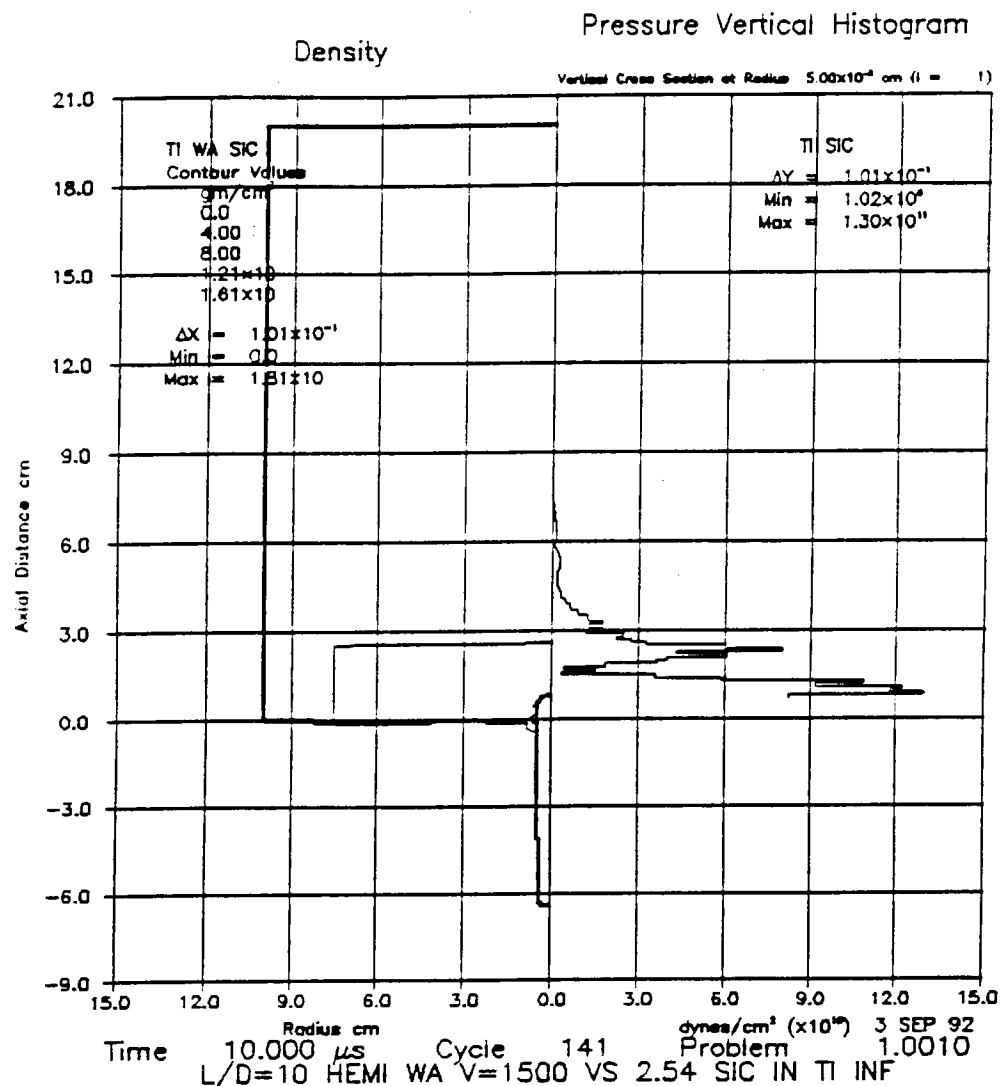


Figure 51. L/D=10 WA rod at 1,500 m/s against 2.54-cm SiC in  $\infty$  Ti at 10  $\mu$ s: pressure vertical histogram on the shotline.

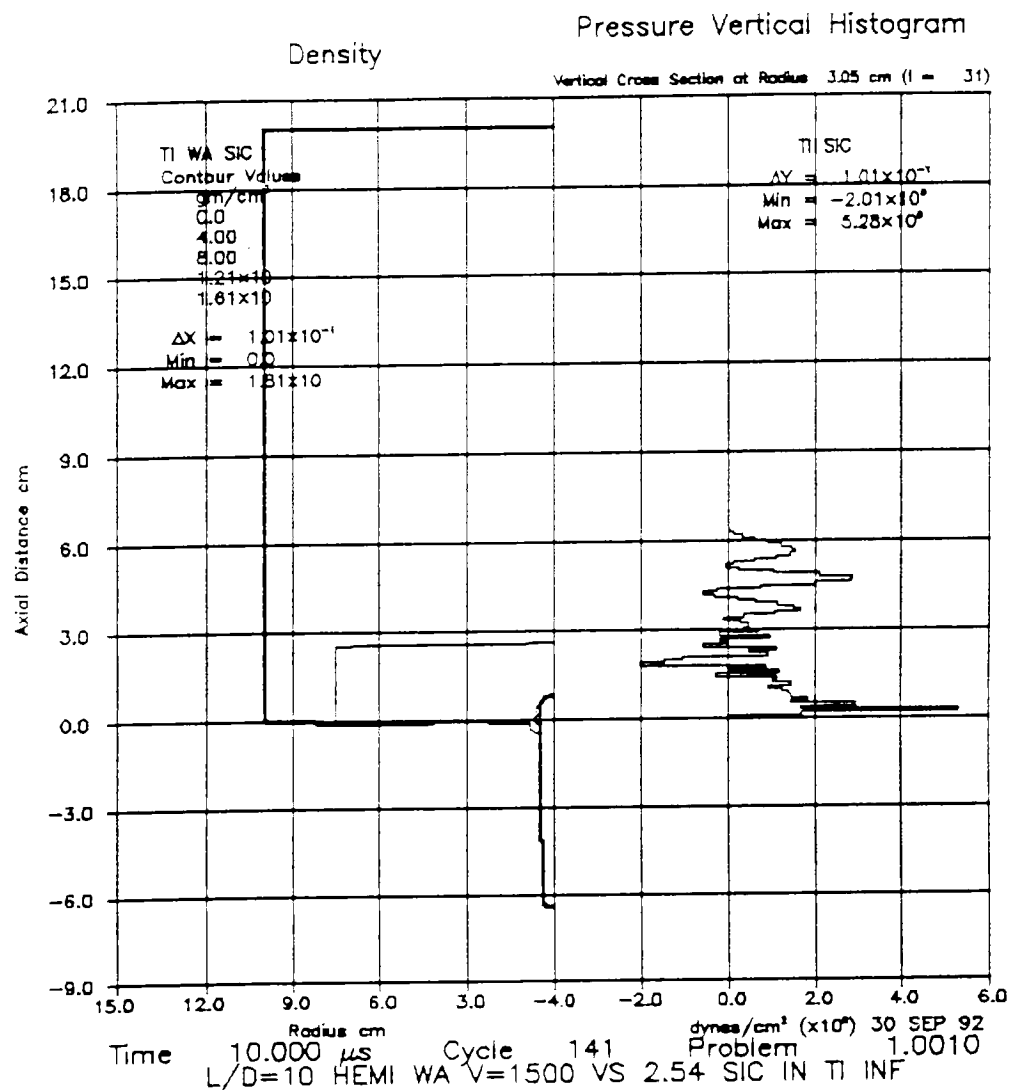


Figure 52. L/D=10 WA rod at 1,500 m/s against 2.54-cm SiC in  $\infty$  Ti at 10  $\mu$ s: pressure vertical histogram 3 cm from the shotline.

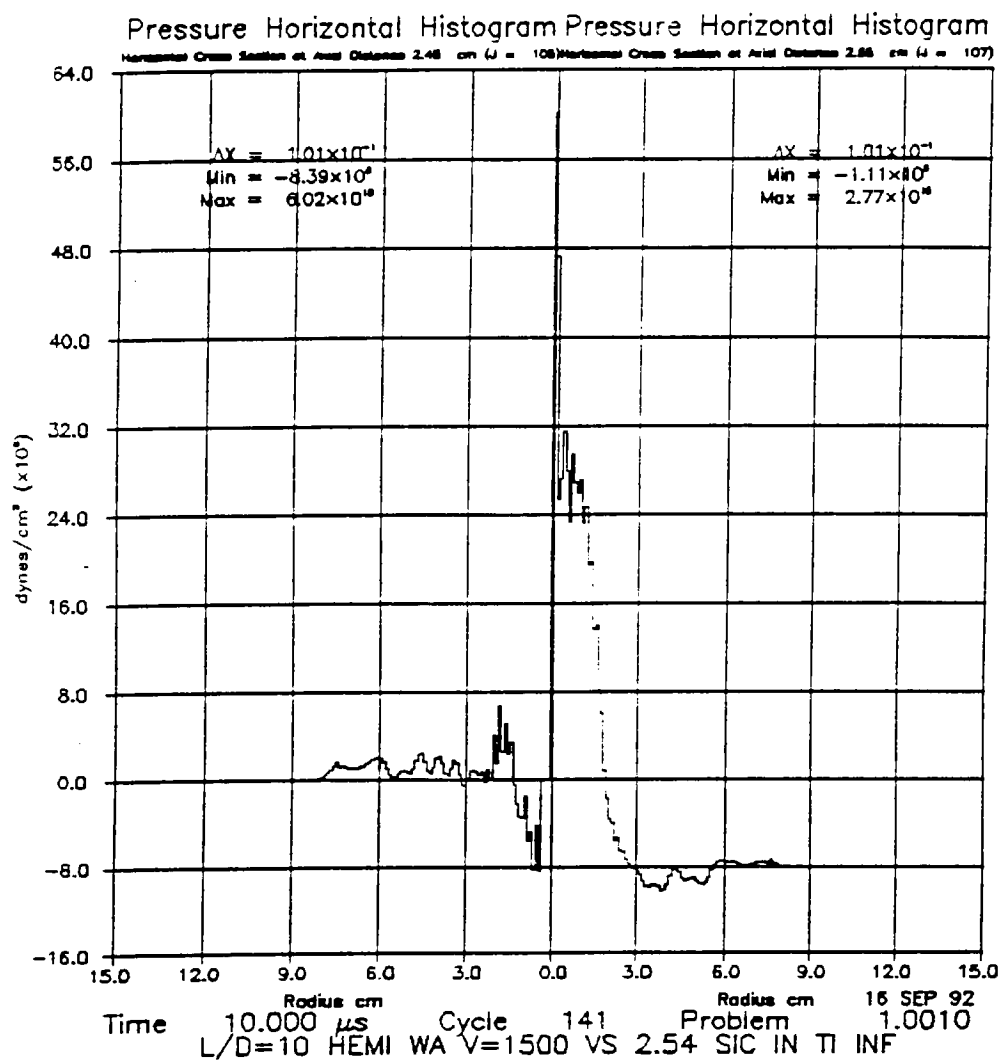


Figure 53. L/D=10 WA rod at 1,500 m/s against 2.54-cm SiC in  $\infty$  Ti at 10  $\mu$ s: pressure horizontal histograms at  $y=2.45$  cm and  $y=2.65$  cm just below and above the tile back.

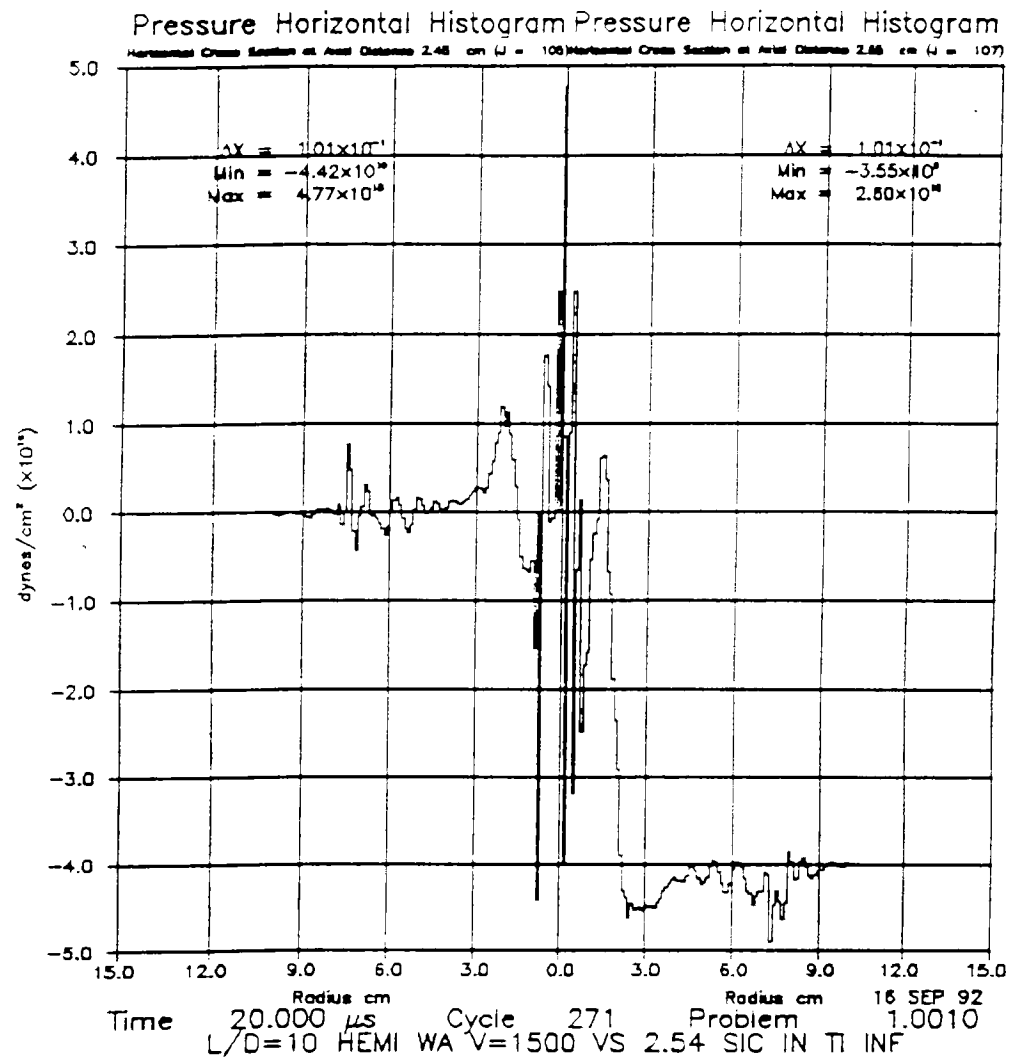


Figure 54. L/D=10 WA rod at 1,500 m/s against 2.54-cm SiC in  $\infty$  Ti at 20  $\mu$ s: pressure horizontal histograms at  $y=2.45$  cm and  $y=2.65$  cm just below and above the tile back.

**INTENTIONALLY LEFT BLANK.**

## 8. REFERENCES

Anderson, C. E., Jr., P. E. O'Donoghue, J. Lankford, and J. D. Walker. "Numerical Simulations of SHPB Experiments for the Dynamic Compressive Strength and Failure of Ceramics." International Journal of Fracture, vol. 55, no. 193, 1992.

Backman, M. E., R. G. S. Sewell, J. C. Schulz, O. E. R. Heimdal, and S. A. Finnegan. "Stagnation Cap Formation on Blunt Projectiles Penetrating Metallic or Brittle Targets." Paper no. 45, pp. 821–833, Metallurgical Applications of Shock-Wave and High-Strain-Rate Phenomena. Edited by L. E. Murr, K. P. Staudhammer, and M. A. Meyers. New York: Marcel Dekker, Inc., 1992.

Bless, S. J., Z. Rosenberg, and B. Yoon. "Hypervelocity Penetration of Ceramics." International Journal of Impact Engineering, vol. 5, pp. 165–171, 1987.

Donachic, M. J., Jr. (editor). Titanium. A Technical Guide. ASM International, Metals Park, OH, p. 34, 1988.

ASM International. Engineered Materials Handbook, Vol. 4: Ceramics and Glasses. Metals Park, OH, p. 752, 1991.

Gust, W. H., A. C. Holt, and E. B. Royce. "Dynamic Yield, Compressional and Elastic Parameters for Several Lightweight Intermetallic Compounds." Journal of Applied Physics, vol. 44, no. 2, p. 550, 1973.

Gust, W. H., and E. B. Royce. "Dynamic Yield Strengths of B C, BeO and Al O Ceramics." Journal of Applied Physics, vol. 42, no. 276, 1971.

Hauver, G. E., P. H. Netherwood, R. F. Benck, W. A. Gooch, W. J. Perciballi, and M. S. Burkins. "Variation of Target Resistance During Long-Rod Penetration into Ceramics." 13th International Symposium on Ballistics, 1992.

Matuska, D. A. HULL, Public Domain Version 122. Orlando Technology Inc. (OTI). Orlando, FL.

McColm, I. J. Ceramic Hardness. New York: Plenum Press, 1990.

Morris, B. L., and C. E. Anderson, Jr. "The Ballistic Performance of Confined Ceramic Tiles." TACOM Combat Vehicle Survivability Symposium, 1991.

Rosenberg Z., and J. Tsaliah. "Applying Tate's Model for the Interaction of Long Rod Projectiles with Ceramic Targets." International Journal of Impact Engineering, vol. 9, no. 2, pp. 247–251, 1990.

Rosenberg, Z., and Y. Yeshurun. "The Relation between Ballistic Efficiency and Compressive Strength of Ceramic Tiles." International Journal of Impact Engineering, vol. 7, no. 3, pp. 357–362, 1988.

Wilkins, M. L. "Mechanics of Penetration and Perforation." International Journal of Engineering Science, vol. 16, pp. 793–808, 1978.

Wilkins, M. L., C. F. Kline, and C. A. Honodel. UCRL 71817, Lawrence Livermore Laboratory.

Wilkins, M. L., C. F. Kline, and C. A. Honodel. UCRL 50694, Lawrence Livermore Laboratory.

Woolsey, P. "Ceramic Materials Screening by Residual Penetration Ballistic Testing." TB-14/1, Thirteenth International Symposium on Ballistics, 1992.

Woolsey, P., D. Kokidko, and S. Mariano. "Progress Report on Ballistic Test Methodology for Armor Ceramics." TACOM Combat Vehicle Survivability Symposium, 1990.

Woolsey, P., S. Mariano, and D. Kokidko. "Alternative Test Methodology for the Ballistic Performance Ranking of Armor Ceramics." Proceedings of the 5th TACOM Armor Conference, 1989.

Zukas, J. A., T. Nicholas, H. F. Swift, L. B. Greszczuk, and D. R. Curran. Impact Dynamics, New York: John Wiley and Sons, Inc., pp. 377-8 and 422, 1982.

<u>No. of Copies</u>	<u>Organization</u>	<u>No. of Copies</u>	<u>Organization</u>
2	Administrator Defense Technical Info Center ATTN: DTIC-DDA Cameron Station Alexandria, VA 22304-6145	1	Commander U.S. Army Missile Command ATTN: AMSMI-RD-CS-R (DOC) Redstone Arsenal, AL 35898-5010
1	Commander U.S. Army Materiel Command ATTN: AMCAM 5001 Eisenhower Ave. Alexandria, VA 22333-0001	1	Commander U.S. Army Tank-Automotive Command ATTN: AMSTA-JSK (Armor Eng. Br.) Warren, MI 48397-5000
1	Director U.S. Army Research Laboratory ATTN: AMSRL-OP-CI-AD, Tech Publishing 2800 Powder Mill Rd. Adelphi, MD 20783-1145	1	Director U.S. Army TRADOC Analysis Command ATTN: ATRC-WSR White Sands Missile Range, NM 88002-5502
1	Director U.S. Army Research Laboratory ATTN: AMSRL-OP-CI-AD, Records Management 2800 Powder Mill Rd. Adelphi, MD 20783-1145	(Class. only) 1	Commandant U.S. Army Infantry School ATTN: ATSH-CD (Security Mgr.) Fort Benning, GA 31905-5660
2	Commander U.S. Army Armament Research, Development, and Engineering Center ATTN: SMCAR-TDC Picatinny Arsenal, NJ 07806-5000	(Unclass. only) 1	Commandant U.S. Army Infantry School ATTN: ATSH-WCB-O Fort Benning, GA 31905-5000
1	Director Benet Weapons Laboratory U.S. Army Armament Research, Development, and Engineering Center ATTN: SMCAR-CCB-TL Watervliet, NY 12189-4050	2	<u>Aberdeen Proving Ground</u> Dir, USAMSAA ATTN: AMXSY-D AMXSY-MP, H. Cohen
1	Director U.S. Army Advanced Systems Research and Analysis Office (ATCOM) ATTN: AMSAT-R-NR, M/S 219-1 Ames Research Center Moffett Field, CA 94035-1000	1	Cdr, USATECOM ATTN: AMSTE-TC
		1	Dir, USAERDEC ATTN: SCBRD-RT
		1	Cdr, USACBDCOM ATTN: AMSCB-CII
		1	Dir, USARL ATTN: AMSRL-SL-I
		5	Dir, USARL ATTN: AMSRL-OP-AP-L

No. of Copies	<u>Organization</u>	No. of Copies	<u>Organization</u>
2	Director Lawrence Livermore National Laboratory ATTN: Dr. Carl Cline Dr. D. J. Steinberg P.O. Box 808 Livermore, CA 94550	27	<u>Aberdeen Proving Ground</u> Dir, USARL ATTN: AMSRL-WT-TA, R. Benck W. Bruchey M. Burkins R. Carroll J. Dehn M. Duffy G. Filbey W. Gillich W. Gooch D. Hackbarth E. Horwath G. Hauver T. Havel Y. Huang H. Meyer P. Netherwood E. Rapacki W. Rowe M. Zoltoski AMSRL-WT-TB, R. Frey AMSRL-WT-TC, W. de Rosset K. Kimsey D. Scheffler AMSRL-WT-TD, D. Dietrich K. Frank G. Randers-Pehrson S. Segletes
4	Director Los Alamos National Laboratory ATTN: Dr. E. Cort Dr. D. Mandell Dr. W. Birchler Dr. J. Dienes Los Alamos, NM 87545		
5	Director Sandia National Laboratories ATTN: Dr. M. Kipp Dr. D. Grady Dr. E. Hertel Dr. P. Yarrington Dr. S. Silling Albuquerque, NM 87185		
1	Institute for Advanced Technology ATTN: Dr. S. Bless 4030-2 W. Braker Lane Austin, TX 78759-5329		
1	Southwest Research Institute ATTN: Dr. C. E. Anderson, Jr. 6220 Culebra Rd, Drawer 28510 San Antonio, TX 78228-0510		